Using Mechanical Oscillators for Transduction and Memory of Quantum States

by

Sarah A. McGee

B.S.E., University of Michigan, 1998

M.S., University of Colorado, 2000

A thesis submitted to the

Faculty of the Graduate School of the

University of Colorado in partial fulfillment

of the requirements for the degree of

Doctor of Philosophy

Department of Physics

2012

This thesis entitled:
Using Mechanical Oscillators for Transduction and Memory of Quantum States
written by Sarah A. McGee
has been approved for the Department of Physics

Murray Holland

Cindy Regal

Date

The final copy of this thesis has been examined by the signatories, and we find that both the content and the form meet acceptable presentation standards of scholarly work in the above mentioned discipline.

McGee, Sarah A. (Ph.D., Physics)

Using Mechanical Oscillators for Transduction and Memory of Quantum States

Thesis directed by Prof. Murray Holland

We study an optomechanical system in which a microwave field and an optical field are coupled to the same mechanical oscillator. We explore the feasibility of using these mechanical oscillators to store quantum mechanical states and to transduce states between optical and microwave electromagnetic oscillators with special consideration given to the effect of mechanical decoherence. Besides being of fundamental interest, this coherent quantum state transfer could also have important practical implications in the field of quantum information science because it allows one to utilize the advantages while overcoming the intrinsic limitations of both platforms. We discuss several state transfer protocols and study their transfer fidelity using a full quantum mechanical model and implementing quantum state diffusion in order to describe the dissipative effects. We find that a state transfer fidelity of 95% can be achieved for parameters realizable with current experimental technology.

Dedication

To the glory of God.

Acknowledgements

I would like to thank many people for helping me along the way to achieving this goal. My family has always been there for me and encouraged me at every stage. From our discussions about quantum physics and God in high school to getting a Ph.D., my family has always helped me. I am forever grateful for their support and prayers.

I also could not have gotten this far without the support and many discussions I have had with my teachers along the way. I would like to thank my high school physics teacher, Philip Dale, who would always discuss many things that were not covered in class with me. My experience at the University of Michigan was also invaluable to me. I am grateful to Dante Amidei and Keith Riles for their help in understanding the fundamentals of quantum physics.

Here at the University of Colorado, I have also had many who were willing to stop what they were doing to help me answer a question or give me advice. I thank Dominic Meiser and Jinx Cooper for helping me understand quantum optics better. I would also like to acknowledge the help of my fellow grad students along the way. I am also grateful for the close collaboration with the experimental groups led by Cindy Regal and Konrad Lehnert. Tauno Palomaki and Jennifer Harlow have both been very helpful in their discussions on the experimental side of the electro-opto-mechanical system. I am also very thankful to have Murray Holland as my advisor. Our discussions have been invaluable. His guidance and direction in my research has helped me immensely.

Most of all, I am incredibly thankful to my Lord and Savior, Jesus Christ. He has been my constant help and inspiration. He has given me the gifts and the understanding to do research and He has helped me to develop those gifts.

Contents

Chapter

Figures

Figure

Chapter 1

Introduction

Recent experiments have demonstrated the ability to control mesoscopic mechanical resonators near the quantum limit [38, 9, 42, 25]. This achievement provides new opportunities for fundamental physics [20] and a new technology for engineering quantum systems [34, 17]. The mechanical resonators are formally equivalent to electromagnetic resonators, which form the foundation of quantum optics, but offer many unique opportunities. For example, mechanical resonators are massive objects that can be coaxed into interacting strongly with many different systems. For instance, in experiments to date, mesoscopic mechanical objects have been coupled to both electrical and optical photons in cavities. It may be possible to sandwich a mesoscopic mechanical resonator between two optical or electrical cavities. Also, as proposed in Ref. [31], it may even be possible to couple a mechanical resonator simultaneously to both electrical and optical cavities, despite the several orders of magnitude difference in the resonance frequencies of each cavity. Such an interface may provide a way to connect quantum resources that are more suited for creating quantum states (electrical circuits) [14] to resources that are more suited for manipulating and storing quantum states (optical platforms).

There are many different systems which could potentially implement a microwave to optical conversion scheme. For example, experiments using dipolar molecules [30, 3] have been proposed for quantum memory and for mapping microwave frequency qubits to the optical regime. One limitation of the dipolar molecular interface is that the microwave frequencies are limited to the allowed transitions in the molecule. With a mesoscopic mechanical resonator, there is a much

broader range of allowed frequencies.

In this new field, an important question is how to harness mechanical resonators within electromagnetic cavities to transduce and store quantum states. By transduction, we mean the transfer of energy between distinct degrees of freedom; in this case, between electromagnetic oscillators whose frequencies are separated by many orders of magnitude. The ability to strongly couple single photons in optomechanical systems would open up a large variety of quantum protocols [29]. However, in order to achieve sufficient coupling, experiments mainly operate the electromagnetic-mechanical interface in an analogous way to three-wave mixing in nonlinear optics [49, 1]. A strong pump tone red-detuned from the cavity is introduced to bridge most of the energy gap between the electromagnetic and mechanical oscillators producing an effective beam-splitter interaction, which can conveniently be turned on and off by varying the pump tone intensity. Single-photon states detuned from the pump can then be transduced between mechanical and any number of electromagnetic wavelengths, depending on the frequency of the pump and cavity spectrum.

The quantum optomechanics experiments envisioned are thus rooted in the well developed toolbox associated with two-mode quantum optics. However, when we introduce low-frequency mechanical resonators, the presence of a thermal bath damping and exciting the phonon resonances must be taken into account in the theoretical analysis. To create a versatile interface between microwave and optical photons, we envision using a low frequency MHz membrane microresonator [38]. Despite recent progress toward bringing such mechanical systems to the quantum regime, mechanical decoherence proportional to the mechanical resonator line strength and thermal bath phonons remains a significant decay pathway.

We first look at the system from the perspective of storage and retrieval of an electromagnetic quantum state in a mechanical resonator. Second, we look at the system from the perspective of transduction of a quantum state from a microwave to optical resonator, or vice versa. We investigate the effect of different protocols on the population of the mechanical state and, hence, the susceptibility to mechanical decoherence. We also explore other applications of the system, such as a Heisenberg interferometer.

A possible experimental implementation of this idea is illustrated in Figure 1.1. The field in an optical cavity is coupled to a thin dielectric drum at the cavity waist. The field acts on the drum by means of the radiation pressure force and the drum acts back on the field through dispersive shifts of the cavity resonance frequency [5]. A segment of the drum is coated with metal and forms one of the plates of a capacitor. The capacitor is part of an LC circuit that acts as a microwave cavity. As the plate of the capacitor moves closer or farther away from the stationary plate, the resonance frequency of the LC circuit changes. Likewise, the LC circuit exerts a force on the movable plate. A similar system has recently been discussed in detail by Taylor et.al. [37].

A theoretical analysis of using this system for transduction was recently done by Wang and Clerk [45]. They studied similar protocols to the ones that we will explore in this thesis for the case of quantum transduction. In that paper, they focus on intra-cavity transduction of Gaussian states (*i.e.*, a pure state whose Wigner function is Gaussian) and then extend the analysis to itinerant photons incident on the one cavity and coming out of the other cavity. In this thesis, we will not only look at the intra-cavity transduction of classical Gaussian states, but also of any quantum state. However, reference [45] is a good resource for someone wanting to explore these concepts further from a different perspective.

The basic system we consider, as we will show, corresponds precisely, in a given parameter regime, to the set of adjustable beam-splitters and cavities illustrated in Figure 1.2. The optomechanical and electromechanical coupling strength can be adjusted to change the effective beam splitters from 0 to 100% reflection and transmission. In the first part of this thesis, we explore the feasibility of using mechanical resonators to store quantum mechanical states and to transduce states between electromagnetic resonators with special consideration given to the effect of mechanical decoherence. In the last part of this thesis, we consider using these effective adjustable beam splitters to form an interferometer.

This is an open quantum system where each of the cavities is coupled to its respective reservoir (not shown in the diagram). The state in each cavity can decay into its reservoir or be thermally excited by the reservoir. We trace out the reservoir variables from the total system-reservoir density

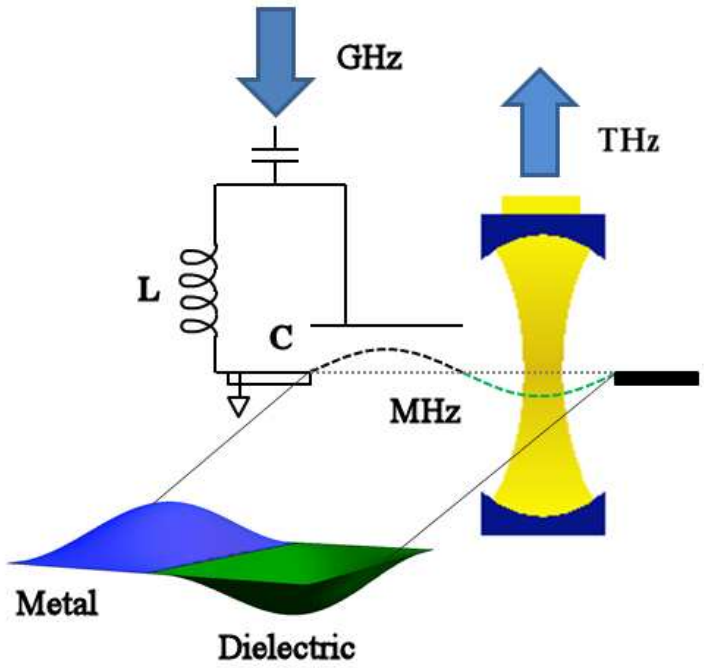

Figure 1.1: The circuit diagram for an optical cavity coupled to a membrane mechanical resonator that in turn is coupled to an electrical LC circuit. The system can be driven or read out by microwave or optical drives.

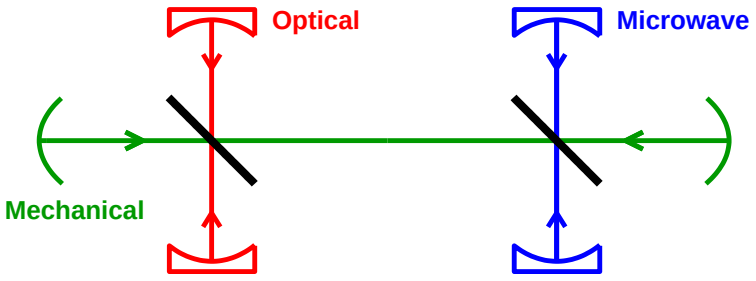

Figure 1.2: The linearized system of two coupled effective adjustable beam splitters. This should be considered to be an open quantum system with all the oscillators coupled to their respective reservoirs (not shown).

matrix and the equations of motion so that only the statistical properties of the reservoir remain. After tracing out the reservoir variables, we arrive at a master equation for the system and the reduced system density matrix. The master equation describes the evolution of the mixed states of our system of three coupled resonators subject to decay into the reservoirs and thermal excitations from the reservoirs.

There are many methods to unravel the mixed states into a set of pure states that can be evolved according to the Schrödinger equation. One of the most well known methods is the Quantum Jump Monte Carlo method. In that method, each pure state is evolved for short time steps with a certain probability of making a jump between states in that time step. Then, all the pure states trajectories are averaged in an ensemble sense to predict the expectation values of experimental measurements.

Another method is the quantum state diffusion method (QSD) that our analysis is based on. This algorithm provides an exact unraveling of the quantum master equation describing this open quantum system into parallel pure state quantum trajectories. These trajectories evolve stochastically rather than using the jumps of the Quantum Jump Monte Carlo method. Using the quantum state diffusion approach, we are able to precisely calculate the fidelity of quantum state memory and quantum state transduction. High fidelity is necessary to store, transfer, and retrieve desired quantum states without adverse modification.

Numerical methods are not limited to Gaussian states. They allow for any quantum input state to be tested. In this thesis, we compare the memory and transduction fidelity for coherent states, squeezed states, cat-states, and nonclassical superpositions of Fock states. Numerical methods also allow for many types of coupling schemes. The simplest scheme is the coherent swapping of the quantum state of two oscillators at a transfer rate determined by the strength of the coupling. This is analogous to Rabi flopping between the internal states of a two-level atom. In addition to this scheme [40], we explore several more diverse swapping schemes and find them to be more robust against the inevitable mechanical decoherence. [46].

In this thesis, we set the decay of the optical and microwave cavities equal to zero and consider

the state preparation of the optical and microwave modes as an initial condition. This simplifies the analysis and allows us to focus on the role of the mechanical decoherence. Nonetheless, the internal and external Q of the optical and microwave cavities is also an important topic, and has recently been treated in both the context of swapping [40] and itinerant photon schemes [46, 32].

In the last part of this thesis, we discuss a protocol to use the system as a Heisenberg interferometer. We make use of a blue detuned pump field to produce correlated pairs of photons and phonons as inputs to the interferometer. This is a truly quantum interferometer which can potentially operate at the Heisenberg limit of phase resolution. The effective beam splitter interaction in the Hamiltonian entangles the two input Fock states, which makes a highly nonclassical phase state. The phase state has large number fluctuations, but small phase difference fluctuations inside the arms of the interferometer where the phase is accumulating. Thus, it improves the phase difference measurement efficiency. This application could enable one to measure any stresses or other factors that modify the mechanical resonance frequency possibly in real time.

This thesis is structured as follows. In Chapter 2, we develop the theoretical model of the system and derive the equations of motion for the system. We develop a model for both red and blue detuned pumps. We then define what "high fidelity" means in this context. We also explore the analogy between our system of three coupled harmonic resonators with a three level atom.

In Chapter 3, we explore the possibilities of quantum memory and transduction in a coherent state basis, which can be solved analytically. We look at many aspects of the system and lay the foundations for much of the numerical analysis that follows.

In Chapter 4, we discuss the quantum state diffusion method and the code we used to numerically simulate the system of three coupled harmonic resonators. We also simulate and analyze key test cases used to verify that the numerical approach is correctly implemented.

In Chapter 5, we consider the possibility of using a reduced system of two coupled harmonic resonators for quantum memory. We look at how the fidelity behaves for several different quantum input states. We also explore how long the quantum state can remain in the system before decaying appreciably.

In Chapter 6, we explore the possibility of quantum transduction in three coupled harmonic resonators. With three resonators, there is more flexibility in the protocols for coupling the resonators together. This allows for a variety of transduction protocols. We analyze several of these transduction protocols and compare and contrast how the fidelity behaves for each of them.

In Chapter 7, we discuss the how the system can also be used as an interferometer. The interference fringes will disappear when each pump is detuned from its respective cavity resonance by exactly the mechanical resonator frequency. Thus, the interferometer protocol can be used to calibrate the detuning of the pumps.

Finally, in Chapter 8, we draw conclusions and relate our theoretical results to the potential for actual experiments.

Chapter 2

Theory and Model

In this chapter, we develop the basic framework for the Hamiltonian describing the system of three coupled harmonic oscillators. We look at the Hamiltonian for both red and blue detuned pumps and how each affects the system differently. Then, we define the fidelity for reading the quantum state out of the system. Finally, we explore the similarities between this system and that of a three-level atom. This chapter is devoted to developing a toolbox for us to use through out the thesis.

2.1 Cooling and Heating

First, we look at the energy levels for the system to get an idea of how the system should behave. For simplicity of illustration, we look at the energy levels for two coupled harmonic oscillators, the optical and mechanical, in Figure 2.1. The optical resonance frequencies, represented by the large vertical steps, are much larger than the mechanical resonance frequency, represented by the small horizontal steps. The initial state is $|n, m\rangle$. The pump field is detuned from the cavity resonance by the mechanical resonator frequency, ω_m.

For a red detuned pump, $\omega_{(o,\mu)} = \omega_{(o,\mu),c} - \omega_m$. So the pump is on resonance with the state $|n+1, m-1\rangle$ and thus will drive the population between those two states. The $|n+1, m-1\rangle$ state can spontaneously decay to the $|n, m-1\rangle$ state. In this way, the population of the resonators will ratchet down to the ground state. Consequently, a red detuned pump leads to cooling in the mechanical resonator. This can be interpreted in terms of simple energetics. In order to excite one

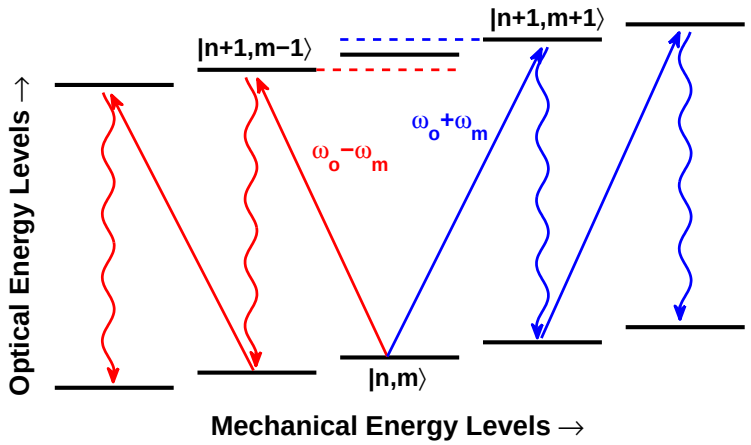

Figure 2.1: The energy levels for a set of two coupled harmonic oscillators. A red detuned pump field will drive the state to lower energy levels while swapping quanta between the two resonators. A blue detuned pump will drive the system to higher energy levels.

photon in the optical cavity, it takes a pump photon from the red detuned drive and the absorption of a phonon from the mechanical resonator. When the mechanical resonator is cooled to the ground state, the process is prohibited. All this requires the resolved sideband limit, *i.e.* that the couplings are weak compared to the relevant detunings as otherwise the power broadening of the transition will invalidate the simple energetic argument.

On the other hand, for a blue detuned pump, $\omega_{(o,\mu)} = \omega_{(o,\mu),c} + \omega_m$, the pump is on resonance with the state $|n+1, m+1\rangle$. Again the state can spontaneously decay to the $|n, m+1\rangle$ state, which will then be driven by the pump to the next higher state. In this way, the population will ratchet up to higher and higher states. Consequently, a blue detuned pump leads to amplification. In this case, the pump photon excites one photon in the optical cavity and one phonon in the mechanical resonator.

2.2 Derivation of the System Hamiltonian

We start by examining the Hamiltonian for the coupled electro-opto-mechanical system (Figure 1.1). Then, the Hamiltonian, in the Schrödinger picture is

$$\hat{H}_{\text{self}} = \hbar\omega_{o,c}\,\hat{a}^\dagger\hat{a} + \hbar\omega_{\mu,c}\,\hat{b}^\dagger\hat{b} + \hbar\omega_m\hat{d}^\dagger\hat{d}\,, \tag{2.1}$$

$$\hat{H}_{\text{coupling}} = -\hbar\frac{g_o}{2}X_{\text{ZP}}\left(\hat{d}e^{i\omega_m t} + \hat{d}^\dagger e^{-i\omega_m t}\right)\hat{a}^\dagger\hat{a} - \hbar\frac{g_\mu}{2}X_{\text{ZP}}\left(\hat{d}e^{i\omega_m t} + \hat{d}^\dagger e^{-i\omega_m t}\right)\hat{b}^\dagger\hat{b}\,, \tag{2.2}$$

$$\hat{H}_{\text{pump}} = \hbar A_o\left(\hat{a}e^{i\omega_{o,c}t} + \hat{a}^\dagger e^{-i\omega_{o,c}t}\right) + \hbar A_\mu\left(\hat{b}e^{i\omega_{\mu,c}t} + \hat{b}^\dagger e^{-i\omega_{\mu,c}t}\right)\,, \tag{2.3}$$

$$\hat{H} = \hat{H}_{\text{self}} + \hat{H}_{\text{coupling}} + \hat{H}_{\text{pump}}\,. \tag{2.4}$$

The operators $\hat{a}$, $\hat{b}$, and $\hat{d}$ are the annihilation operators for a photon inside the optical cavity, for a photon inside the microwave cavity, and for a phonon inside the mechanical resonator, respectively. The pump frequencies are $\omega_{(o,\mu)}$ and the cavity resonance frequencies are $\omega_{(o,\mu),c}$, where o stands for optical and μ stands for microwave. The mechanical resonator resonance frequency is ω_m. X_{ZP} is the mechanical harmonic oscillator length. Both optical and microwave cavities are pumped by strong coherent fields with amplitudes A_o and A_μ, respectively, which lead to a buildup of large steady state amplitudes in those cavities. The purpose of the strong pump fields is to increase the

optomechanical coupling.

The strong coherent pump fields A_o and A_μ lead to a buildup of large steady state amplitudes in the optical and microwave resonators. The steady state intracavity field amplitudes, in turn, shift the equilibrium position of the mechanical resonator. The bare coupling constants g_o and g_μ are given by $g_{(o,\mu)} = \partial\Delta_{o,\mu}/\partial q$ where q is the position of the mechanical resonator and Δ_o and Δ_μ are the resonance frequencies of the optical and microwave resonators in the frame rotating with their respective pump frequencies.

First, we go into the interaction picture to explicitly show the dependence on the detuning $\Delta_{(o,\mu)} = \omega_{(o,\mu),c} - \omega_{(o,\mu)}$. We Define

$$\hat{H}_o \equiv \hbar\omega_o\ \hat{a}^\dagger\hat{a} + \hbar\omega_\mu\ \hat{b}^\dagger\hat{b} \tag{2.5}$$

$$\begin{aligned}\hat{V}_{\text{self}} =& \hat{H}_{\text{self}} - \hat{H}_o \\ =& \hbar\Delta_o\hat{a}^\dagger\hat{a} + \hbar\Delta_\mu\hat{b}^\dagger\hat{b} + \hbar\omega_m\hat{d}^\dagger\hat{d}\ .\end{aligned} \tag{2.6}$$

The other parts of the Hamiltonian remain unchanged so that the total interaction part of the Hamiltonian is

$$\hat{V} = \hat{V}_{\text{self}} + \hat{H}_{\text{coupling}} + \hat{H}_{\text{pump}}\ . \tag{2.7}$$

The interaction Hamiltonian is then,

$$\hat{H}_I = e^{-i\hat{H}_o t}\hat{V}e^{i\hat{H}_o t}\ . \tag{2.8}$$

We use the Baker-Hausdorff theorem to simplify the exponentials,

$$e^{\alpha\hat{X}}\hat{Y}e^{-\alpha\hat{X}} = \hat{Y} + \alpha\left[\hat{X},\hat{Y}\right] + \frac{\alpha^2}{2!}\left[\hat{X},\left[\hat{X},\hat{Y}\right]\right] + \frac{\alpha^3}{3!}\left[\hat{X},\left[\hat{X},\left[\hat{X},\hat{Y}\right]\right]\right] + \dots\ . \tag{2.9}$$

Thus, each operator is transformed in the following way,

$$
\begin{aligned}
e^{-i\hat{H}_o t/\hbar}\ \hat{a}\ e^{i\hat{H}_o t/\hbar} &= \hat{a}e^{-i\omega_o t} && (2.10)\\
e^{-i\hat{H}_o t/\hbar}\ \hat{a}^\dagger\ e^{i\hat{H}_o t/\hbar} &= \hat{a}^\dagger e^{i\omega_o t} && (2.11)\\
e^{-i\hat{H}_o t/\hbar}\ \hat{b}\ e^{i\hat{H}_o t/\hbar} &= \hat{b}e^{-i\omega_\mu t} && (2.12)\\
e^{-i\hat{H}_o t/\hbar}\ \hat{b}^\dagger\ e^{i\hat{H}_o t/\hbar} &= \hat{b}^\dagger e^{i\omega_\mu t} && (2.13)\\
e^{-i\hat{H}_o t/\hbar}\ \hat{d}\ e^{i\hat{H}_o t/\hbar} &= \hat{d} && (2.14)\\
e^{-i\hat{H}_o t/\hbar}\ \hat{d}^\dagger\ e^{i\hat{H}_o t/\hbar} &= \hat{d}^\dagger\ . && (2.15)
\end{aligned}
$$

Thus, for example, the optical pump term becomes,

$$
\begin{aligned}
\hbar A_o e^{-i\hat{H}_o t}\left(\hat{a}e^{i\omega_{o,c}t}+\hat{a}^\dagger e^{-i\omega_{o,c}t}\right)e^{i\hat{H}_o t} =& \hbar A_o\left(\hat{a}e^{i(\omega_{o,c}-\omega_o)t}+\hat{a}^\dagger e^{-i(\omega_{o,c}-\omega_o)t}\right)\\
=& \hbar A_o\left(\hat{a}e^{i\Delta_o t}+\hat{a}^\dagger e^{-i\Delta_o t}\right) \qquad (2.16)
\end{aligned}
$$

Applying the Baker-Hausdorff theorem to all the terms gives the full interaction Hamiltonian,

$$
\begin{aligned}
\hat{H}_I =& \hbar\Delta_o\hat{a}^\dagger\hat{a}+\hbar\Delta_\mu\hat{b}^\dagger\hat{b}+\hbar\omega_m\hat{d}^\dagger\hat{d}\\
&-\hbar\frac{g_o}{2}X_{\mathrm{ZP}}\left(\hat{d}e^{i\omega_m t}+\hat{d}^\dagger e^{-i\omega_m t}\right)\hat{a}^\dagger\hat{a}-\hbar\frac{g_\mu}{2}X_{\mathrm{ZP}}\left(\hat{d}e^{i\omega_m t}+\hat{d}^\dagger e^{-i\omega_m t}\right)\hat{b}^\dagger\hat{b}\\
&+\hbar A_o\left(\hat{a}e^{i\Delta_o t}+\hat{a}^\dagger e^{-i\Delta_o t}\right)+\hbar A_\mu\left(\hat{b}e^{i\Delta_\mu t}+\hat{b}^\dagger e^{-i\Delta_\mu t}\right)\ . \qquad (2.17)
\end{aligned}
$$

The description of the system is greatly simplified by splitting off the steady state expectation values of the various operators in the Hamiltonian Eq. (2.4) and by introducing fluctuations around these means,

$$
\begin{aligned}
\hat{a} \rightarrow& \langle\hat{a}\rangle_{\mathrm{SS}}e^{i\Delta_o t}+\hat{a}\ ,\\
\hat{b} \rightarrow& \langle\hat{b}\rangle_{\mathrm{SS}}e^{i\Delta_\mu t}+\hat{b}\ . \qquad (2.18)
\end{aligned}
$$

After removing the constant offset, the Hamiltonian to second order is,

$$\begin{aligned}\hat{H}_{\text{eff}} =&\hbar\left[\Delta_o\langle\hat{a}\rangle_{\text{SS}} + A_o\right]\left(\hat{a}e^{i\Delta_o t} + \hat{a}^\dagger e^{-i\Delta_o t}\right) + \hbar\left[\Delta_\mu\langle\hat{b}\rangle_{\text{SS}} + A_\mu\right]\left(\hat{b}e^{i\Delta_\mu t} + \hat{b}^\dagger e^{-i\Delta_\mu t}\right)\\ &- \hbar\frac{g_o}{2}X_{\text{ZP}}\langle\hat{a}\rangle_{\text{SS}}^2\left(\hat{d}e^{-i\omega_m t} + \hat{d}^\dagger e^{i\omega_m t}\right) - \hbar\frac{g_\mu}{2}X_{\text{ZP}}\langle\hat{b}\rangle_{\text{SS}}^2\left(\hat{d}e^{-i\omega_m t} + \hat{d}^\dagger e^{i\omega_m t}\right)\\ &+ \hbar\Delta_o\hat{a}^\dagger\hat{a} + \hbar\Delta_\mu\hat{b}^\dagger\hat{b} + \hbar\omega_m\hat{d}^\dagger\hat{d}\\ &- \hbar\frac{g_o}{2}X_{\text{ZP}}\langle\hat{a}\rangle_{\text{SS}}\Big(\hat{a}^\dagger\hat{d}^\dagger e^{-i(\Delta_o+\omega_m)t} + \hat{a}\hat{d}e^{i(\Delta_o+\omega_m)t}\\ &\qquad + \hat{a}\hat{d}^\dagger e^{-i(\Delta_o-\omega_m)t} + \hat{a}^\dagger\hat{d}e^{i(\Delta_o-\omega_m)t}\Big)\\ &- \hbar\frac{g_\mu}{2}X_{\text{ZP}}\langle\hat{b}\rangle_{\text{SS}}\Big(\hat{b}^\dagger\hat{d}^\dagger e^{-i(\Delta_\mu+\omega_m)t} + \hat{b}\hat{d}e^{i(\Delta_\mu+\omega_m)t}\\ &\qquad + \hat{b}\hat{d}^\dagger e^{-i(\Delta_\mu-\omega_m)t} + \hat{b}^\dagger\hat{d}e^{i(\Delta_\mu-\omega_m)t}\Big)\,. \end{aligned} \tag{2.19}$$

By setting the linear terms equal to zero, we find that the steady state expectation values are related to the pump amplitude and detuning,

$$\langle\hat{a}\rangle_{\text{SS}} = -\frac{A_o}{\Delta_o}\,, \tag{2.20}$$

$$\langle\hat{b}\rangle_{\text{SS}} = -\frac{A_\mu}{\Delta_\mu}\,. \tag{2.21}$$

With that, the Hamiltonian becomes,

$$\begin{aligned}\hat{H}_{\text{eff}} =&\hbar\Delta_o\hat{a}^\dagger\hat{a} + \hbar\Delta_\mu\hat{b}^\dagger\hat{b} + \hbar\omega_m\hat{d}^\dagger\hat{d}\\ &- \hbar\frac{\Omega_o}{2}\langle\hat{a}\rangle_{\text{SS}}\left(\hat{d}e^{-i\omega_m t} + \hat{d}^\dagger e^{i\omega_m t}\right) - \hbar\frac{\Omega_\mu}{2}\langle\hat{b}\rangle_{\text{SS}}\left(\hat{d}e^{-i\omega_m t} + \hat{d}^\dagger e^{i\omega_m t}\right)\\ &- \hbar\frac{\Omega_o}{2}\left(\hat{a}^\dagger\hat{d}^\dagger e^{-i(\Delta_o+\omega_m)t} + \hat{a}\hat{d}e^{i(\Delta_o+\omega_m)t} + \hat{a}\hat{d}^\dagger e^{-i(\Delta_o-\omega_m)t} + \hat{a}^\dagger\hat{d}e^{i(\Delta_o-\omega_m)t}\right)\\ &- \hbar\frac{\Omega_\mu}{2}\left(\hat{b}^\dagger\hat{d}^\dagger e^{-i(\Delta_\mu+\omega_m)t} + \hat{b}\hat{d}e^{i(\Delta_\mu+\omega_m)t} + \hat{b}\hat{d}^\dagger e^{-i(\Delta_\mu-\omega_m)t} + \hat{b}^\dagger\hat{d}e^{i(\Delta_\mu-\omega_m)t}\right)\,, \end{aligned} \tag{2.22}$$

where the bare coupling constants have been modified to become

$$\Omega_o = -\,g_o X_{\text{ZP}}\frac{A_o}{\Delta_o}\,, \tag{2.23}$$

$$\Omega_\mu = -\,g_\mu X_{\text{ZP}}\frac{A_\mu}{\Delta_\mu}\,. \tag{2.24}$$

The highest experimental values have achieved about $\Omega_o \sim 0.1\omega_m$ and $\Omega_\mu \sim 0.1\omega_m$ [39, 42] for $\Delta_{(o,\mu)} = \omega_m$. It is important to note that the pump amplitude, $A_{(o,\mu)}$ is a complex number

containing the relative phase of the pump field. Thus, the relative phase can be modified to change the sign of the modified coupling constants. The magnitude of the coupling can be modified by changing the bare coupling strength, the pump amplitude or the detuning.

2.3 Red Detuned System Hamiltonian

For the case where both the optical and microwave resonators are subject to a pump field that is red detuned from their respective cavity resonance frequencies such that

$$\begin{aligned}\Delta_o \equiv& \omega_{o,c} - \omega_o = \omega_m \\ \Delta_\mu \equiv& \omega_{\mu,c} - \omega_\mu = \omega_m \ ,\end{aligned} \tag{2.25}$$

then, the Hamiltonian in Eq. 2.22 becomes,

$$\begin{aligned}\hat{H}_{\text{eff}} =& \hbar\omega_m \left(\hat{a}^\dagger\hat{a} + \hat{b}^\dagger\hat{b} + \hat{d}^\dagger\hat{d}\right) \\ &- \hbar\frac{\Omega_o}{2}\langle\hat{a}\rangle_{\text{SS}}\left(\hat{d}e^{-i\omega_m t} + \hat{d}^\dagger e^{i\omega_m t}\right) - \hbar\frac{\Omega_\mu}{2}\langle\hat{b}\rangle_{\text{SS}}\left(\hat{d}e^{-i\omega_m t} + \hat{d}^\dagger e^{i\omega_m t}\right) \\ &- \hbar\frac{\Omega_o}{2}\left(\hat{a}^\dagger\hat{d}^\dagger e^{-2i\omega_m t} + \hat{a}\hat{d}e^{2i\omega_m t} + \hat{a}\hat{d}^\dagger + \hat{a}^\dagger\hat{d}\right) \\ &- \hbar\frac{\Omega_\mu}{2}\left(\hat{b}^\dagger\hat{d}^\dagger e^{-2i\omega_m t} + \hat{b}\hat{d}e^{2i\omega_m t} + \hat{b}\hat{d}^\dagger + \hat{b}^\dagger\hat{d}\right) \ .\end{aligned} \tag{2.26}$$

In the resolved sideband limit where the frequency, ω_m, of the mechanical resonator is much larger than the mechanical decay rate (as well as the effective coupling constants), we can employ the rotating wave approximation where all the rapidly oscillating time dependent terms average to zero, which leads to

$$\hat{H}_{\text{eff}} = \hbar\omega_m\left(\hat{a}^\dagger\hat{a} + \hat{b}^\dagger\hat{b} + \hat{d}^\dagger\hat{d}\right) - \hbar\frac{\Omega_o}{2}\left(\hat{a}^\dagger\hat{d} + \hat{a}\ \hat{d}^\dagger\right) - \hbar\frac{\Omega_\mu}{2}\left(\hat{b}^\dagger\hat{d} + \hat{b}\ \hat{d}^\dagger\right) \ . \tag{2.27}$$

This bilinear Hamiltonian is analogous to three quantized single mode fields coupled to each other by beam splitters as illustrated in Figure 1.2. The beam splitters are adjustable. A coupling of $\pi/2$ will be like a 50/50 beam splitter. A coupling of π will be like a mirror, swapping the states perfectly. If we turn the coupling off, the oscillators will propagate freely as if there is no beam

splitter. Thus, by varying the coupling constants, we can change from 0 to 100% reflection and transmission.

It is important to note that the quantum mechanical systems described by the field operators $\hat{a}$, $\hat{b}$, and $\hat{d}$ are in fact fluctuations of the bare fields around their stationary values at each of their respective resonator frequencies.

2.4 Blue Detuned System Hamiltonian

For the case where both the optical and microwave resonators are subject to a blue detuned pump field such that,

$$\begin{aligned}\Delta_o \equiv& \omega_{o,c} - \omega_o = -\omega_m \\ \Delta_\mu \equiv& \omega_{\mu,c} - \omega_\mu = -\omega_m \ ,\end{aligned} \tag{2.28}$$

then the effective system Hamiltonian from Eq. 2.22 becomes,

$$\begin{aligned}\hat{H}_{\text{eff}} =& \hbar\omega_m \left(-\hat{a}^\dagger\hat{a} - \hat{b}^\dagger\hat{b} + \hat{d}^\dagger\hat{d}\right) \\ &- \hbar\frac{\Omega_o}{2}\langle\hat{a}\rangle_{\text{SS}} \left(\hat{d}e^{-i\omega_m t} + \hat{d}^\dagger e^{i\omega_m t}\right) - \hbar\frac{\Omega_\mu}{2}\langle\hat{b}\rangle_{\text{SS}} \left(\hat{d}e^{-i\omega_m t} + \hat{d}^\dagger e^{i\omega_m t}\right) \\ &+ \hbar\frac{\Omega_o}{2}\left(\hat{a}^\dagger\hat{d}e^{2i\omega_m t} + \hat{a}\hat{d}^\dagger e^{-2i\omega_m t} + \hat{a}\hat{d} + \hat{a}^\dagger\hat{d}^\dagger\right) \\ &+ \hbar\frac{\Omega_\mu}{2}\left(\hat{b}^\dagger\hat{d}e^{-2i\omega_m t} + \hat{b}\hat{d}^\dagger e^{2i\omega_m t} + \hat{b}\hat{d} + \hat{b}^\dagger\hat{d}^\dagger\right) \ .\end{aligned} \tag{2.29}$$

Applying the rotating wave approximation leads to the simple blue detuned effective Hamiltonian:

$$\hat{H}_{\text{eff}} = \hbar\omega_m \left(-\hat{a}^\dagger\hat{a} - \hat{b}^\dagger\hat{b} + \hat{d}^\dagger\hat{d}\right) + \hbar\frac{\Omega_o}{2}\left(\hat{a}^\dagger\hat{d}^\dagger + \hat{a}\hat{d}\right) + \hbar\frac{\Omega_\mu}{2}\left(\hat{b}^\dagger\hat{d}^\dagger + \hat{b}\hat{d}\right) \ . \tag{2.30}$$

Notice that unlike the red detuned case in which beam-splitter like coupling emerged, here the Hamiltonian corresponds to creation or destruction of pairs of photons and phonons. This leads to exponential growth or decay of the populations in each coupled system, and is reminiscent of parametric amplification in nonlinear optical devices. Figure 2.2 shows the schematic diagram of one such parametric amplifier.

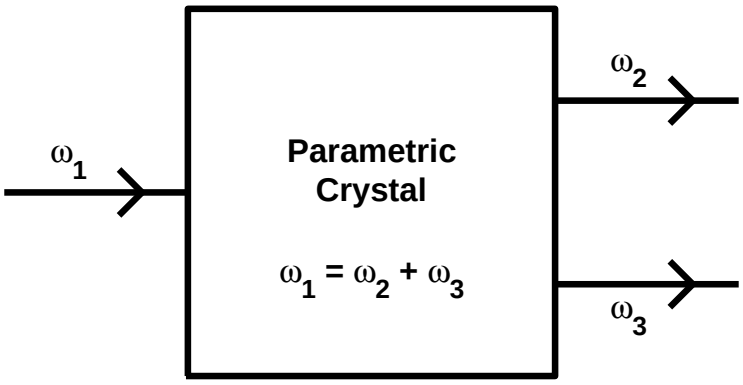

Figure 2.2: A schematic diagram of a parametric amplifier.

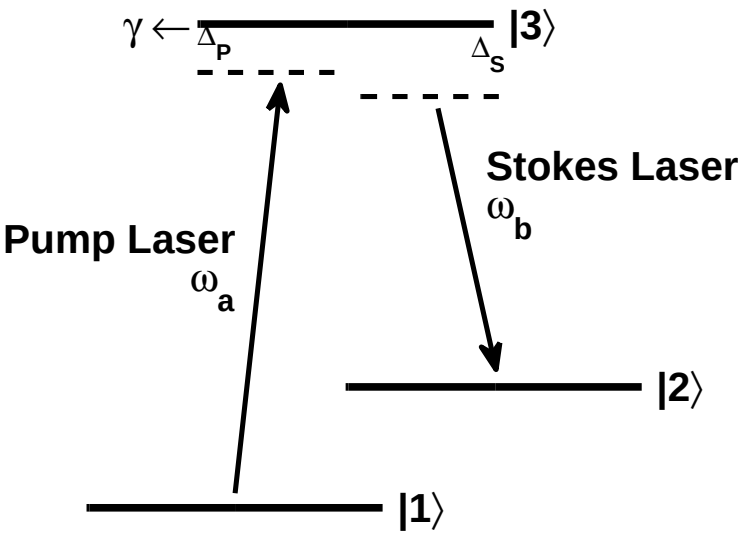

Figure 2.3: Schematic of a three level atom showing the coupling needed for the STIRAP process. The Stokes coupling is turned on first. Then the pump coupling is turned on, resulting in state transfer from state $|1\rangle$ to state $|2\rangle$ without leaving any population in state $|3\rangle$.

2.5 Analogy to Three Level Atom

Putting the Hamiltonian in Eq. 2.27 in matrix form reveals a remarkable similarity to the Hamiltonian for a three level atom (Figure 2.3). Thus, the two systems may have similar behavior in certain parameter regimes. This allows us to take insight from the quantum dynamics of few level atomic systems and immediately understand certain aspects of the coupled microresonator system.

We make an analogy between the states of a three level atom and the $n = 1$ states of each resonator. We equate the atomic state $|1\rangle$ with having one photon in the microwave resonator, state $|2\rangle$ with having one photon in the optical resonator, and state $|3\rangle$ with having one phonon in the mechanical resonator. The self energy terms of the Hamiltonian in Eq. 2.27 are

$$\hat{H}_{\text{self}} = \hbar \begin{pmatrix} \Delta_\mu & 0 & 0 \\ 0 & \Delta_o & 0 \\ 0 & 0 & \omega_m \end{pmatrix} . \tag{2.31}$$

The interaction part of the Hamiltonian is

$$\hat{V} = -\frac{1}{2}\hbar \begin{pmatrix} 0 & 0 & \Omega_\mu \\ 0 & 0 & \Omega_o \\ \Omega_\mu & \Omega_o & 0 \end{pmatrix} . \tag{2.32}$$

We can diagonalize the matrix and find the Eigenstates and Eigenvalues [46].

$$\hat{H} = \hbar\omega_+ \hat{c}_+^\dagger \hat{c}_+ + \hbar\omega_- \hat{c}_-^\dagger \hat{c}_- + \hbar\omega_o \hat{c}_o^\dagger \hat{c}_o \tag{2.33}$$

where

$$\hat{c}_+ = -\frac{1}{\sqrt{2}}\hat{d} - \frac{\Omega_o \hat{a} + \Omega_\mu \hat{b}}{\sqrt{2\left(\Omega_o^2 + \Omega_\mu^2\right)}} \tag{2.34}$$

$$\hat{c}_- = \frac{1}{\sqrt{2}}\hat{d} - \frac{\Omega_o \hat{a} + \Omega_\mu \hat{b}}{\sqrt{2\left(\Omega_o^2 + \Omega_\mu^2\right)}} \tag{2.35}$$

$$\hat{c}_o = \frac{\Omega_\mu \hat{a} - \Omega_o \hat{b}}{\sqrt{\Omega_o^2 + \Omega_\mu^2}} \tag{2.36}$$

and

$$\omega_+ = \omega_m - \sqrt{\Omega_o^2 + \Omega_\mu^2} \tag{2.37}$$

$$\omega_- = \omega_m + \sqrt{\Omega_o^2 + \Omega_\mu^2} \tag{2.38}$$

$$\omega_o = \omega_m \, . \tag{2.39}$$

There is a dark state associated with $\hat{c_o}$ that does not affect the state of the mechanical resonator. We can adiabatically move a state in the microwave resonator to the optical resonator by slowly varying the couplings without putting any population in the mechanical state. At the beginning of the process, the optomechanical coupling is slowly turned on while the electromechanical coupling is off so that the dark state is $\hat{c_o} = \hat{b}$. At the end of the process, the electromechanical coupling is on, while the optomechanical coupling is off leaving the dark state in $\hat{c_o} = -\hat{a}$. This effectively transduces the quantum state from the microwave cavity to the optical cavity.

This is similar to the Stimulated Raman Adiabatic Passage (STIRAP) process in a three level atom. In the STIRAP process, the Stokes coupling (the coherent coupling between states $|2\rangle$ and $|3\rangle$) is turned on first which splits the energy levels for state $|3\rangle$. Then, the pump coupling (the coherent coupling between states $|1\rangle$ and $|3\rangle$) is turned on and the population in state $|1\rangle$ is seen to be transferred to state $|2\rangle$ without ever having any significant population in state $|3\rangle$ because of the interference between the pathways corresponding to transversing each of the two split energy levels. We will consider this adiabatic transduction process further in Ch. 6.

2.6 Fidelity

These Hamiltonians do not take into account the mechanical decoherence and thermal noise that we would like to focus on throughout this thesis. In order to account for the thermal and decay effects we use the Lagrangian in addition to the Hamiltonian.

$$L[\hat{\rho}] = \frac{\gamma_m \bar{n}}{2}\left(\hat{d}^\dagger \hat{d}\hat{\rho} + \hat{\rho}\hat{d}^\dagger \hat{d} - 2\hat{d}\hat{\rho}\hat{d}^\dagger\right) + \frac{\gamma_m\left(\bar{n}+1\right)}{2}\left(\hat{d}\hat{d}^\dagger\hat{\rho} + \hat{\rho}\hat{d}\hat{d}^\dagger - 2\hat{d}^\dagger\hat{\rho}\hat{d}\right) \, , \tag{2.40}$$

where γ_m is the decay rate of the mechanical resonator and $\bar{n}$ is the average occupation number of the thermal bath. The Lagrangian makes an analytical solution impossible so, we need to numerically

simulate the evolution of the system under the influence of mechanical decay and thermal noise. We will look more at the numerical methods we employ in Ch. 4. But here, we look at the fidelity measure [40] that we will use to quantitatively measure the success of the schemes we explore in this thesis. We look at the fidelity [40] for retrieving the input state after storage or transfer as a function of the mechanical quality factor, $Q_m = \omega_m/\gamma_m$. The fidelity [41] we employ is defined as

$$F(\rho_i, \rho_f) \equiv \left[\mathrm{Tr}\left(\sqrt{\sqrt{\rho_i}\rho_f\sqrt{\rho_i}}\right)\right]^2 \tag{2.41}$$

where ρ_i and ρ_f are the reduced density matrices for the input and output states respectively.

To calculate this more easily in our numerical simulations, we convert this equation to an eigenvalue equation. We set $M = \sqrt{\rho_i}\rho_f\sqrt{\rho_i}$ and the fidelity becomes $F = [\mathrm{Tr}\sqrt{M}]^2$. We find the eigenvalues λ_i of M by a unitary transformation U such that $UMU^{-1} = M'$ and

$$M' = \begin{pmatrix} \lambda_1 & 0 & \dots \\ 0 & \lambda_2 & \dots \\ \vdots & \vdots & \ddots \end{pmatrix} . \tag{2.42}$$

The fidelity formula is now

$$\begin{aligned} F &= \left[\mathrm{Tr}\, U\sqrt{M}U^{-1}\right]^2 \\ &= \left[\mathrm{Tr}\sqrt{UMU^{-1}}\right]^2 \\ &= \left[\mathrm{Tr}\sqrt{M'}\right]^2 \\ &= \left[\sum_i \sqrt{\lambda_i}\right]^2 . \end{aligned} \tag{2.43}$$

We next show that the fidelity function has the anticipated properties [18]. Since ρ is positive definite, we can easily see that the fidelity is also positive definite. Also, ρ has strictly positive eigenvalues that are less than 1, and so $0 \leq F \leq 1$. The upper limit 1 corresponds to perfect replication of the quantum state, while small values of F indicate significant degradation. For

$\rho_i = \rho_f$, we want the fidelity to equal 1, which is true since

$$\begin{aligned} F &= \left[\mathrm{Tr}\left(\sqrt{\sqrt{\rho_i}\rho_i\sqrt{\rho_i}}\right)\right]^2 \\ &= \left[\mathrm{Tr}\left(\sqrt{\rho_i^2}\right)\right]^2 \\ &= \left[\mathrm{Tr}\,\rho_i\right]^2 \\ &= 1\ . \end{aligned} \tag{2.44}$$

A special simplification occurs for pure states where the fidelity reduces to an overlap functional:

$$\begin{aligned} F &= \left[\mathrm{Tr}\left(\sqrt{\sqrt{\rho_i}\rho_f\sqrt{\rho_i}}\right)\right]^2 \\ &= \left[\mathrm{Tr}\left(\sqrt{\rho_i\rho_f\rho_i}\right)\right]^2 \\ &= \left[\mathrm{Tr}\left(\sqrt{|\psi_i\rangle\langle\psi_i|\psi_f\rangle\langle\psi_f|\psi_i\rangle\langle\psi_i|}\right)\right]^2 \\ &= \left[\mathrm{Tr}\left(|\langle\psi_i|\psi_f\rangle|\rho_i\right)\right]^2 \\ &= |\langle\psi_i|\psi_f\rangle|^2\ . \end{aligned} \tag{2.45}$$

2.7 Summary

In this chapter, we have developed a toolbox that we will use throughout this thesis. We have derived the red and blue detuned linearized Hamiltonians for the system of three coupled harmonic resonators. The energetic properties of the Hamiltonians shows the cooling and heating effects in the system. The Eigenstates and Eigenvalues of the red detuned Hamiltonian are very similar to those of a three level atom. Also, we defined the fidelity function that we will use to quantitatively measure the success of the schemes presented in future chapters.

Chapter 3

Transduction and Quantum Memory in a Coherent State Basis

3.1 Transduction

To illustrate many of the concepts we will explore in this thesis, we will first look at the solution in the classical regime by working exclusively with coherent states. In this case, the three coupled harmonic resonator system may be solved analytically. This provides a reference for the full quantum solutions that we consider later in the thesis.

We will assume that the initial state in the microwave resonator is $|\beta(t=0)\rangle$ with the other resonators starting in the vacuum $|0\rangle$ state. We also assume that the transduction occurs from the microwave resonator to the optical resonator. The output state is then $|\alpha(t_f)\rangle$.

If all the oscillators, mechanical, microwave, and optical are in coherent states, the eigenstates for each resonator subsystem are given by

$$\hat{a}|\alpha\rangle = \alpha|\alpha\rangle \tag{3.1}$$

$$\hat{b}|\beta\rangle = \beta|\beta\rangle \tag{3.2}$$

$$\hat{d}|\delta\rangle = \delta|\delta\rangle \ . \tag{3.3}$$

In addition, the initial quantum state of the full system is the tensor product of the individual resonator states, *i.e.*,

$$|\Psi\rangle = |\alpha\rangle \otimes |\beta\rangle \otimes |\delta\rangle \ . \tag{3.4}$$

3.1.1 Equations of Motion

To derive the equations of motion for the system, we start with the linearized Hamiltonian given in Eq. 2.27.

$$\hat{H} = \hbar\omega_m \left(\hat{a}^\dagger\hat{a} + \hat{b}^\dagger\hat{b} + \hat{d}^\dagger\hat{d}\right) - \frac{\hbar\Omega_o}{2}\left(\hat{a}^\dagger\hat{d} + \hat{d}^\dagger\hat{a}\right) - \frac{\hbar\Omega_\mu}{2}\left(\hat{b}^\dagger\hat{d} + \hat{d}^\dagger\hat{b}\right) \tag{3.5}$$

The time derivative of each operator is given by the Heisenberg equation.

$$\frac{d\hat{a}(t)}{dt} = \frac{1}{i\hbar}\left[\hat{a}, \hat{H}\right] \tag{3.6}$$

$$\frac{d\langle\Psi(t)|\hat{a}|\Psi(t)\rangle}{dt} = \frac{1}{i\hbar}\langle\Psi(t)|\left[\hat{a}, \hat{H}\right]|\Psi(t)\rangle \tag{3.7}$$

$$\frac{d\alpha(t)}{dt} = \langle\Psi(t)|\left(-i\omega_m\hat{a} + i\frac{\Omega_o}{2}\hat{d}\right)|\Psi(t)\rangle \tag{3.8}$$

$$\dot{\alpha}(t) = -i\omega_m\alpha(t) + i\frac{\Omega_o}{2}\delta(t)\ . \tag{3.9}$$

The other subsystem equations are performed in the same manner,

$$\dot{\beta}(t) = -i\omega_m\beta(t) + i\frac{\Omega_\mu}{2}\delta(t) \tag{3.10}$$

$$\dot{\delta}(t) = -i\omega_m\delta(t) + i\frac{\Omega_o}{2}\alpha(t) + i\frac{\Omega_\mu}{2}\beta(t)\ . \tag{3.11}$$

3.1.2 Constant Coupling

In the case where the couplings are constant, the equations of motion 3.9- 3.11 can be solved analytically. The solution is

$$\alpha(t) = \frac{e^{-i\omega_m t}}{\tilde{\Omega}^2}\left(\Omega_\mu\left(\Omega_\mu\alpha(0) - \Omega_o\beta(0)\right) + \Omega_o\left(\Omega_o\alpha(0) + \Omega_\mu\beta(0)\right)\cos\left(\frac{\tilde{\Omega}t}{2}\right) + i\Omega_o\tilde{\Omega}\delta(0)\sin\left(\frac{\tilde{\Omega}t}{2}\right)\right) \tag{3.12}$$

$$\beta(t) = \frac{e^{-i\omega_m t}}{\tilde{\Omega}^2}\left(\Omega_o\left(\Omega_o\beta(0) - \Omega_\mu\alpha(0)\right) + \Omega_\mu\left(\Omega_o\alpha(0) + \Omega_\mu\beta(0)\right)\cos\left(\frac{\tilde{\Omega}t}{2}\right) + i\Omega_\mu\tilde{\Omega}\delta(0)\sin\left(\frac{\tilde{\Omega}t}{2}\right)\right) \tag{3.13}$$

$$\delta(t) = \frac{e^{-i\omega_m t}}{\tilde{\Omega}^2}\left(\tilde{\Omega}\delta(0)\cos\left(\frac{\tilde{\Omega}t}{2}\right) + i\left(\Omega_o\alpha(0) + \Omega_\mu\beta(0)\right)\sin\left(\frac{\tilde{\Omega}t}{2}\right)\right) \tag{3.14}$$

where $\tilde{\Omega} = \sqrt{\Omega_o^2 + \Omega_\mu^2}$ is the Rabi frequency. For our set of initial conditions, $\alpha(0) = 0$ and $\delta(0) = 0$, the equations reduce to

$$\alpha(t) = \frac{e^{-i\omega_m t}}{\tilde{\Omega}^2}\left(-\Omega_o\Omega_\mu\beta(0) + \Omega_o\Omega_\mu\beta(0)\cos\left(\frac{\tilde{\Omega}t}{2}\right)\right) \tag{3.15}$$

$$\beta(t) = \frac{e^{-i\omega_m t}}{\tilde{\Omega}^2}\left(\Omega_o^2\beta(0) + \Omega_\mu^2\beta(0)\cos\left(\frac{\tilde{\Omega}t}{2}\right)\right) \tag{3.16}$$

$$\delta(t) = i\frac{e^{-i\omega_m t}}{\tilde{\Omega}^2}\Omega_\mu\beta(0)\sin\left(\frac{\tilde{\Omega}t}{2}\right) \ . \tag{3.17}$$

Figure 3.1 illustrates the normal Rabi flopping that occurs when the resonators are coupled with a constant coupling. For the electromechanical system shown in Figure 3.1(A), the Rabi frequency reduces to $\tilde{\Omega} = \Omega_\mu$. For the electro-optomechanical system shown in Figure 3.1(B), the Rabi frequency reduces to $\tilde{\Omega} = \sqrt{2}\Omega_\mu$, where we have set $\Omega_o = \Omega_\mu$.

In order to get transduction in this system, we need to have two pulses. The first π pulse, which we take to have a square profile, will swap the state from the microwave resonator into the mechanical resonator. Then the second π pulse, also taken to be square, will swap the state into the optical resonator. This is shown in Figure 3.2. The time needed for this transfer is thus $2\pi/\Omega_\mu$.

However, if both couplings are on at the same time, as we saw in Figure 3.1(B), the Rabi frequency is increased to $\sqrt{2}\Omega_\mu$. Thus the pulse area needed for the swapping pulses increases to $\sqrt{2}\pi$. The total transfer time is now $\sqrt{2}\pi/\Omega_\mu$ as shown in Figure 3.3. Also note that here the state is transferred directly from the microwave resonator to the optical resonator without fully populating the mechanical resonator.

3.1.3 Analytic Fidelity Formula

In general, the fidelity in the coherent state basis, is just the overlap between the two Gaussian states [40],

$$F = |\langle\alpha(t_f)|\beta(0)\rangle|^2 \ , \tag{3.18}$$

since the oscillator states remain pure rather than mixed by assumption. For the coherent case, the initial state is $|\beta(0)\rangle$ representing the state in the microwave resonator. The final state will be

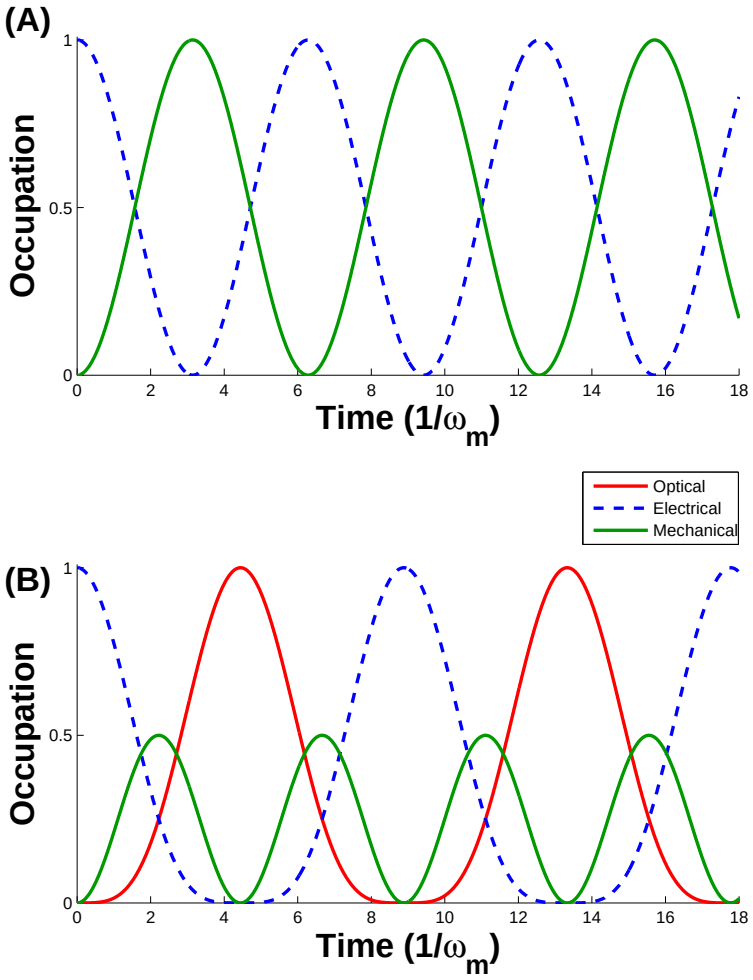

Figure 3.1: The occupation numbers of each resonator swap back and forth at the Rabi frequency when the coupling between the resonators is kept constant. The initial state in the microwave resonator is $\beta(0) = 1$. (A) The case for two coupled resonators such as in the electromechanical system. (B) The case for three coupled resonators such as the electro-optomechanical system. Here we have set $\Omega_o = \Omega_\mu = 1$.

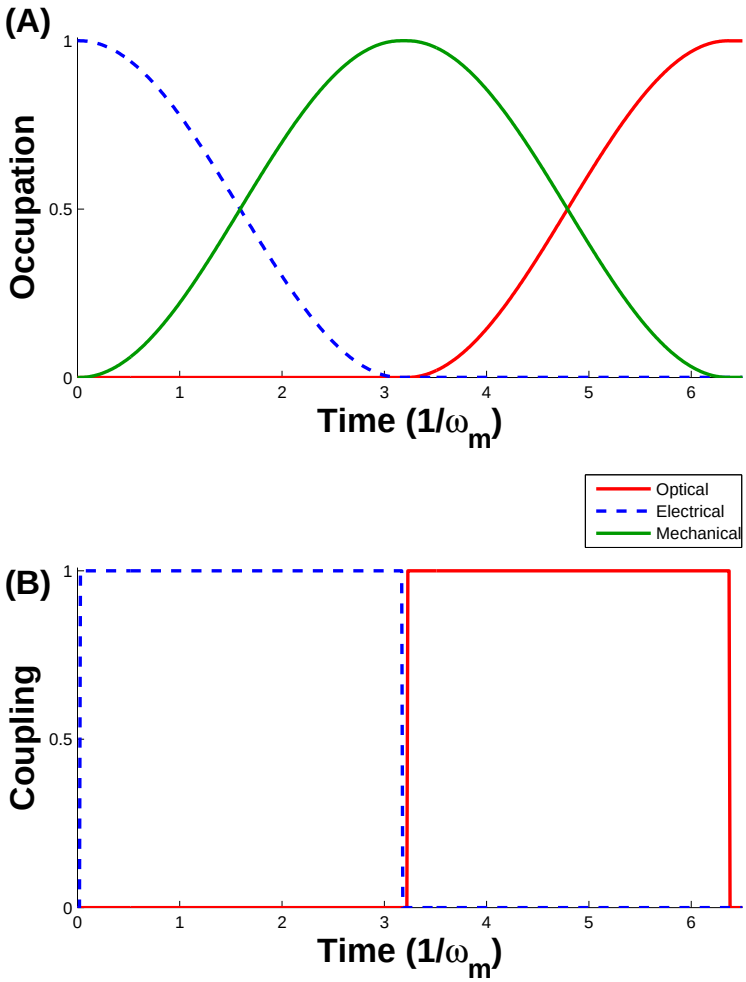

Figure 3.2: (A) The occupation number for the optical, microwave, and mechanical resonators throughout the transduction cycle with each coupling turned on in sequence. (B) The coupling pulses needed to accomplish the transduction. First the electromechanical coupling, with a pulse area of π, is turned on to swap the state from the microwave resonator into the mechanical resonator. Then the optomechanical coupling, also with a pulse area of π, is turned on to swap the state into the optical resonator. Here we have set $\Omega_o = \Omega_\mu = 1$ for illustration purposes.

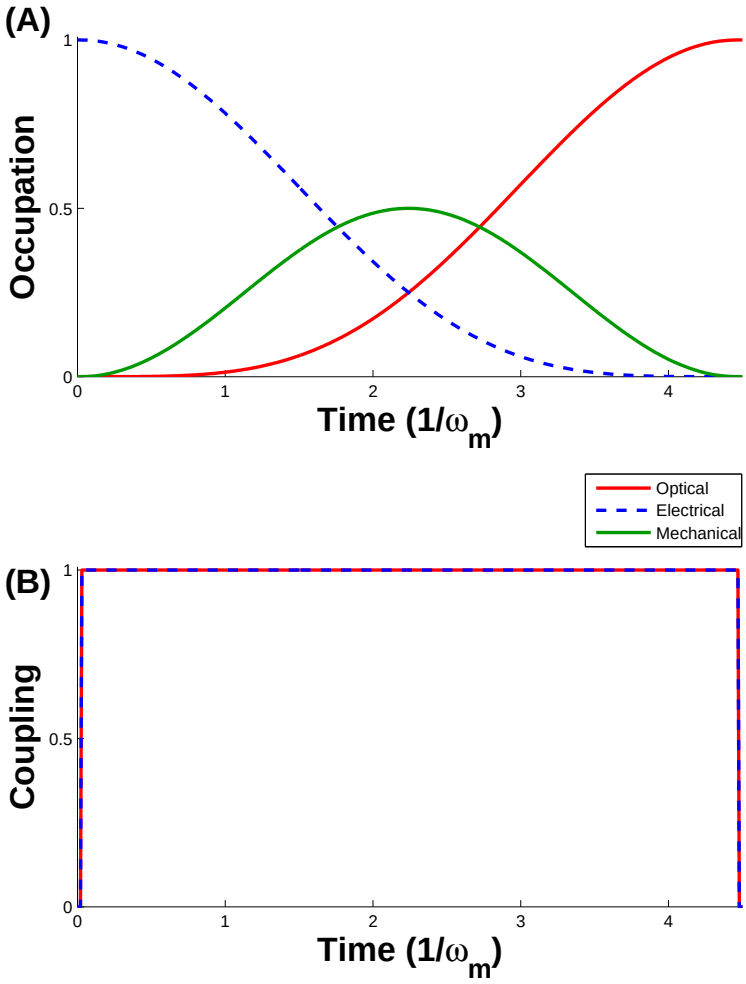

Figure 3.3: (A) The occupation number for the optical, microwave, and mechanical resonators throughout the transduction cycle with both couplings on. (B) The coupling pulses needed to accomplish the transduction. The electromechanical and the optomechanical couplings, both with a pulse area of $\sqrt{2}\pi$, are turned on to swap the state directly from the microwave resonator into the optical resonator. Here we have set $\Omega_o = \Omega_\mu = 1$ for illustration purposes.

$|\alpha(t_f)\rangle$ representing the final state in the optical resonator for quantum transduction and the final state in the microwave resonator for quantum memory.

At zero temperature, in the case where the pulse duration is short compared to the decay time of the mechanical resonator, we can neglect the decay during the swapping pulses and assume that the swaps happened perfectly. In that case, the final state will only have decayed exponentially, at the mechanical decay rate γ_m, during the time, ΔT, between the two π pulses to become $|\psi_f\rangle = |e^{-\gamma_m \Delta T/2}\beta(0)\rangle$. Thus we can analytically find the fidelity for a pure final state to be

$$F = |\langle e^{-\frac{\omega_m \Delta T}{2Q_m}}\beta(0)|\beta(0)\rangle|^2 = e^{-|\beta(0)|^2(1-e^{-\omega_m \Delta T/(2Q_m)})^2} \ . \tag{3.19}$$

However, for non-zero temperatures or large decay rates the final state will thermalize quickly and this formula will no longer be valid. The state does not decay to the vacuum as Eq. (3.19) suggests. Rather it decays to a thermalized value. Thus, the final fidelity for pure states will saturate at low-Q to the overlap between a thermalized state and the initial state. Thus, the coherent state fidelity (Figure 3.4) takes on the form,

$$F(Q) = F(0) + (1 - F(0))\, e^{-|\beta(0)|^2(1-e^{-\omega_m \Delta T/(2Q_m)})^2} \ . \tag{3.20}$$

where $F(0)$ is the thermal saturation overlap value.

Further complicating matters, the full density matrix, which is pure, must be reduced to the resonator subsystem that is being read out before taking the fidelity overlap with the reduced input density matrix. This makes the reduced density matrices impure. Consequently, we need to employ the more general formula to find the fidelity that is valid for states that are not pure.

3.1.4 Pulsed Coupling

Square pulses have a sinc squared frequency composition, and thus a significant contribution from high frequency components. Now we use Gaussian pulses for the coupling parameters so we can look at more sophisticated pulse sequences that have a smoother and localized frequency

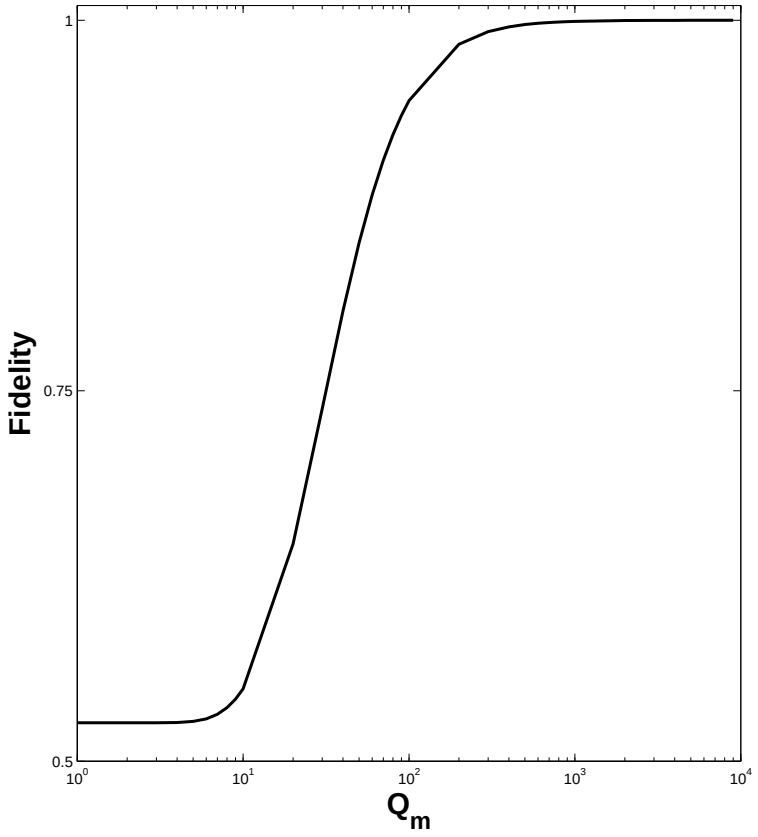

Figure 3.4: The fidelity from Eq. 3.20 as a function of mechanical resonator quality, Q_m. Here $\Delta T = 64(1/\omega_m)$ and $F(0) = 0.25$.

decomposition;

$$\Omega_o(t) = \Omega_o(t_o) e^{-\frac{(t-t_o)^2}{w_o^2 \pi}} \tag{3.21}$$

$$\Omega_\mu(t) = \Omega_\mu(t_\mu) e^{-\frac{(t-t_\mu)^2}{w_\mu^2 \pi}} \tag{3.22}$$

where $\Omega_o(t_o)$ and $\Omega_\mu(t_\mu)$ are the pulse amplitudes and w_o and w_μ are the pulse widths. For simplicity, we set the amplitudes and widths equal ($\Omega_o(t_o) = \Omega_\mu(t_\mu) = \Omega$ and $w_o = w_\mu = w$) so both coupling pulses have the same shape. The only difference will be the location of the center of the Gaussian pulses. The pulse area of either coupling pulse is then given by $w\Omega\pi$.

The equations of motion 3.9-3.11 cannot be solved analytically in any simple way. We numerically solve the equations for a variety of relative pulse centers and widths. We sweep the pulse centers from the point where the two coupling pulses are completely separated with the microwave pulse occurring first to the point where they are occurring simultaneously. This allows us to compare with the results of section 3.1.2. Then, we continue the sweep with the optical pulse occurring first until the pulses are completely separated again. We do this for a variety of pulse areas, while keeping Ω constant.

Figure 3.5 shows the fidelity across the sweeps when the reservoir to which the mechanical resonator is coupled to is at zero temperature. This allows us to neglect decay and thermal noise processes in our analysis. The zero on the x axis is the point where the two coupling pulses are occurring simultaneously. The positive x values indicate the separation between the peaks of the two coupling pulses that are intuitive, *i.e.*, the electromechanical coupling pulse occurs before the optomechanical coupling pulse. The negative x values indicate the separation between the peaks of the two coupling pulses that are counter-intuitive, *i.e.*, the optomechanical coupling pulse occurs before the electromechanical coupling pulse.

As the pulses move farther apart, they eventually become effectively separated and the distance between them no longer matters (since there is no decay here). This is the area on the lower right-hand side of the plot where the fidelity peaks level off at multiples of π. Pulses that are π pulses or an odd integer multiple of a π pulse will swap the state completely from the microwave

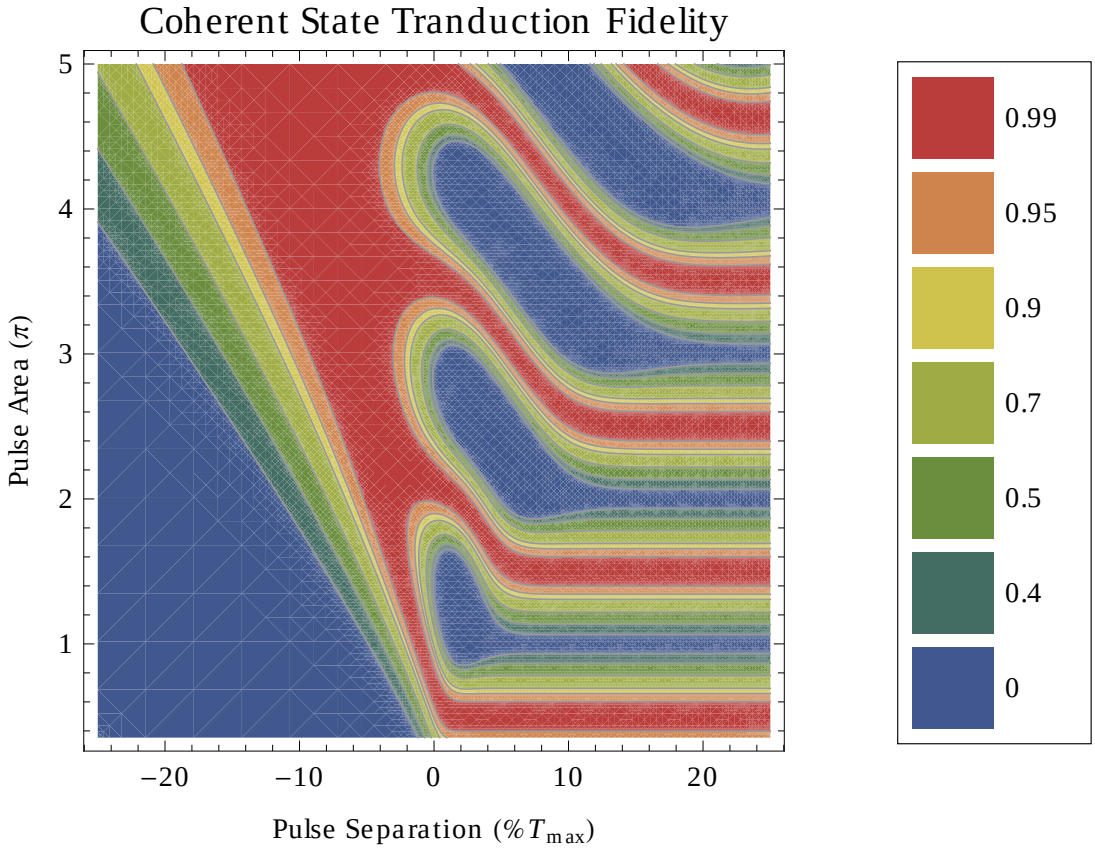

Figure 3.5: The fidelity vs. pulse width and pulse separation for $Q_m = 10000$ and $\bar{n} = 0$.

resonator to the optical resonator. Any other pulse area will not perfectly swap the states. Thus, we see the periodic behavior we expect in that part of the plot in analogy with Rabi oscillations.

At zero pulse separation, the pulses are identical and the Rabi swapping pulse area is $\sqrt{2}\pi$. Thus, the peak fidelity periods are at odd integer multiples of $\sqrt{2}\pi$. For partially overlapping intuitive pulses, the peak fidelity periods smoothly drop from the simultaneous values to the separated values.

The lower left-hand side of the plot is where the counter-intuitive pulses have gotten far enough apart to be effectively separated and thus no transduction is occurring. However, when the counter-intuitive pulses are partially overlapping, we see a large area of high fidelity with no oscillatory behavior. This corresponds to the optomechanical implementation of the STIRAP process more usually seen in a three-level atom system as we discussed in section 2.5. Each state in the Fermionic three level atom is analogous to a ladder of Boson states in each harmonic resonator. Instead of having a population of 0 or 1 in each of the three states, there can be any population in each state. The fact that the STIRAP process is evident in a Bosonic system consisting of coupled resonators with a Hilbert space dimension much larger than three, rather than in a Fermionic system of only three levels is significant. As the pulse area increases, the pulses become more and more adiabatic and the separation and pulse area of the pulses becomes more and more irrelevant.

3.2 Memory: Quantum Information Storage and Retrieval

Now we reduce the system to two coupled harmonic resonators to study the quantum memory case. This is equivalent to setting $\Omega_o = 0$ so that we are only looking at the electromechanical subsystem. The initial state is still $|\beta(0)\rangle$ in the microwave resonator and $|0\rangle$ in the mechanical resonator. However the coupling pulses will now swap the state into the mechanical resonator and then back to the microwave resonator. We want to explore how long the state can be stored in the mechanical resonator before significant degradation occurs.

3.2.1 Equations of Motion

The reduced equations of motion for the coherent amplitudes are

$$\dot{\beta}(t) = -i\omega_m\beta(t) + i\frac{\Omega_\mu}{2}\delta(t) \tag{3.23}$$

$$\dot{\delta}(t) = -i\omega_m\delta(t) + i\frac{\Omega_\mu}{2}\beta(t) - \frac{\gamma_m}{2}\delta(t)\ . \tag{3.24}$$

The solutions for the constant coupling are now,

$$\beta(t) = e^{-(i\omega_m+\gamma_m/4)t}\left(\beta(0)\cos\left(\frac{\tilde{\Omega}}{2}t\right) + \frac{\beta(0)\gamma_m + 2i\delta(0)\Omega_\mu}{2\tilde{\Omega}}\sin\left(\frac{\tilde{\Omega}}{2}t\right)\right) \tag{3.25}$$

$$\delta(t) = e^{-(i\omega_m+\gamma_m/4)t}\left(\delta(0)\cos\left(\frac{\tilde{\Omega}}{2}t\right) + \frac{-\delta(0)\gamma_m + 2i\beta(0)\Omega_\mu}{2\tilde{\Omega}}\sin\left(\frac{\tilde{\Omega}}{2}t\right)\right) \tag{3.26}$$

where $\tilde{\Omega} = \sqrt{\Omega_\mu^2 - \gamma_m^2/4}$.

3.2.2 Storage Time

For the case of strong short $\pi/2$ pulses, the decay can be neglected during the pulses, so that the final state only depends on the length of time between the storage and retrieval pulses, ΔT and the decay rate,

$$\beta(\Delta T) = \beta(0)e^{-i\omega_m\Delta T}e^{-\gamma_m\Delta T/2}\ . \tag{3.27}$$

This gives us the same fidelity that we found in Eq. 3.19.

In Figure 3.6 we plot the fidelity for three different $Q_m = \omega_m/\gamma_m$ values vs. the storage time ΔT. In subplot (A), we see that the fidelity decays exponentially with the storage time at a rate determined by Q_m as expected. In subplot (B), we show the same fidelity versus the storage time scaled by the mechanical resonator quality. When the axes are scaled like this, all the curves collapse onto a universal curve:

$$F = e^{-|\beta(0)|^2(1-e^{-\zeta_o/2})^2} \tag{3.28}$$

where $\zeta_o = \omega_m\Delta T/Q_m$.

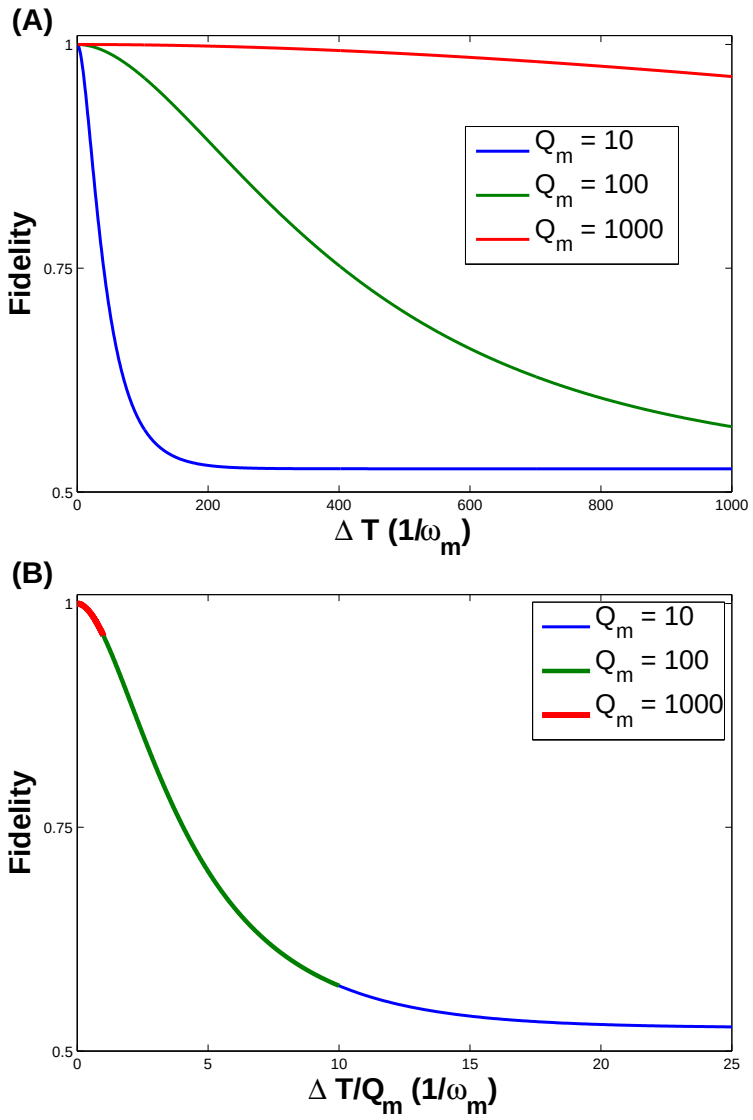

Figure 3.6: (A) The fidelity decays for longer storage times and lower mechanical quality. (B) The same fidelity scaled by the mechanical quality so that all curves collapse onto one universal curve $F = e^{-|\beta(0)|^2(1-e^{-\zeta_o/2})^2}$ where $\zeta_o = \omega_m \Delta T/Q_m$. Here $\beta(0) = 1$.

3.3 Summary

We illustrated many of the concepts we will use throughout this thesis by working exclusively with coherent states for a zero temperature bath. We looked at the fidelity for transduction with separated, simultaneous, and adiabatic transfer schemes. We will explore these protocols further with other quantum states in Ch. 6. We also looked at the fidelity for quantum memory versus storage time and found a universal curve for how the fidelity decays. We will further explore quantum memory with other quantum states in Ch. 5.

Chapter 4

Quantum State Diffusion

4.1 QSD Algorithm

We use the quantum state diffusion (QSD) method to simulate the fully quantum evolution of this open system [12, 28, 4, 48]. The QSD method is well suited for this problem because it yields the conditional evolution of an open quantum system subject to homodyne measurements of the output fields. In this way, we may obtain amplitude and phase information about the decay channel. In the QSD approach, we stochastically evolve each resonator subsystem as if we were performing a continuous fictitious homodyne measurement of the photons or phonons coming out of each resonator. Even though an actual experiment can not measure the phonons in the mechanical resonator, the numerical simulation gives us access to this information in the spirit of a 'Gedanken' measurement. For the scenarios we explore, the decay rates of the optical and microwave resonators are set to zero, so that only the mechanical resonator is coupled to the environment. Thus, in those cases, the stochastic evolution only applies to the mechanical resonator subsystem, while the optical and microwave resonators evolve according to the Schrödinger equation. In actual experiments, the optical and microwave resonators are also coupled to the environment and actual homodyne measurements can be performed on those output fields. The QSD method works for the fully open system as well. But in this thesis, we are reducing the fully open system to focus only on the mechanical decoherence.

The total state of the system is the tensor product of the states of each resonator subsystem

$$|\Psi(t)\rangle = |\psi_a(t)\rangle \otimes |\psi_b(t)\rangle \otimes |\psi_d(t)\rangle \tag{4.1}$$

if the subsystems are not entangled with each other. We construct the initial total state of the system in this way. Then, we evolve the total state according to the QSD algorithm, which has the effect of entangling the subsystem states.

In the QSD method, the evolution of the total density matrix of the system is unraveled into an ensemble of stochastic parallel pure state trajectories. Each trajectory is evolved according to a stochastic differential equation. The trajectories are then averaged in the ensemble sense to recreate the total density matrix. In the limit of a large number of trajectories, the ensemble average of the stochastic trajectories goes to a state diffusion evolution. Each trajectory evolves according to the stochastic differential equation [48]

$$\begin{aligned}|\tilde{\Psi}(t+dt)\rangle =& \Big\{1 - \big[\frac{\gamma_m(2\bar{n}+1)}{2}\hat{d}^\dagger\hat{d} + 2\gamma_m(2\bar{n}+1)\langle\hat{d}^\dagger + \hat{d}\rangle\hat{d} + \frac{i}{\hbar}\hat{H}_{\text{eff}}\big]dt \\ &+ \hat{d}\sqrt{\gamma_m\bar{n}}\; dW_d(t) + \hat{d}^\dagger\sqrt{\gamma_m(\bar{n}+1)}\; dW_{d^\dagger}(t)\Big\}|\Psi(t)\rangle\end{aligned} \tag{4.2}$$

where, $dW(t)$ is the continuum limit of a Wiener increment, ΔW, which satisfies the ensemble average $\langle(\Delta W)^2\rangle = \Delta t$ of a Gaussian random distribution with a width Δt. There are two Wiener increments, one for each noise process in the mechanical oscillator where there are two types of decay channels, one for phonons entering the system and one for phonons leaving the system. The stochastic evolution is not Hermitian and thus does not preserve the norm of the state. So, the new total state must also be normalized at each time step in the numerical integration.

The SDE can be rewritten in the form,

$$|\tilde{\Psi}(t+dt)\rangle = \left[1 - \hat{A}\; dt + \sum_i \hat{B}_i dW_i(t)\right]|\Psi(t)\rangle \tag{4.3}$$

which is the starting point for the multidimensional second order weak scheme given in reference [21] on page 486 that we use to implement the QSD method in the C++ programming language.

4.2 Test Cases

We used several test cases to validate our approach and computational implementation. We looked at the two level atom case, the case of one thermal harmonic oscillator, the case of cooling the mechanical oscillator with a red detuned pump, and the case of heating with a blue detuned pump.

4.2.1 Two Level Atom

First, we compared the numerical results with the known solution for a two level atom where the effective Hamiltonian is

$$\hat{H}_{\text{eff}} = \Delta\hat{\sigma}_z + \Omega\left(\hat{\sigma}_+ + \hat{\sigma}_-\right) - i\frac{\gamma}{2}\hat{\sigma}_+\hat{\sigma}_- \ , \tag{4.4}$$

where Δ is the detuning, Ω is the Rabi frequency, γ is the spontaneous decay rate from the excited state to the ground state, and $\hat{\sigma}_+$, $\hat{\sigma}_-$, and $\hat{\sigma}_z$ are the Pauli spin matrices. The solution to the optical Bloch equations that results from this Hamiltonian for the excited state probability of a two-level atom is [15]

$$\rho_{ee} = \frac{2\Omega^2}{\gamma^2/2 + 4\Omega^2}\left(1 - \left(\cos(\lambda t) + \frac{3\gamma}{4\lambda}\sin(\lambda t)\right)e^{-3\gamma t/4}\right) \tag{4.5}$$

where $\lambda = \sqrt{4\Omega^2 - \gamma^2/16}$.

Figure 4.1(A) shows the first 10 individual trajectories for the excited state probability from the QSD simulation. The average of the first 10 trajectories is shown by the thick black line. All 4000 trajectories in the simulation average to the final excited state probability shown in Figure 4.1(B). Figure 4.1(B) shows numerical results for the probability of being in the excited state compared with the analytic solution of the optical Bloch equations when the atom is initially in the ground state. We ran 4000 trajectories and set $\Omega = 3\gamma$.

As we increase the number of trajectories, we would expect the noise for a second order weak scheme to decrease like $1/\sqrt{n}$ where n is the number of trajectories, which is what we see in Figure 4.2.

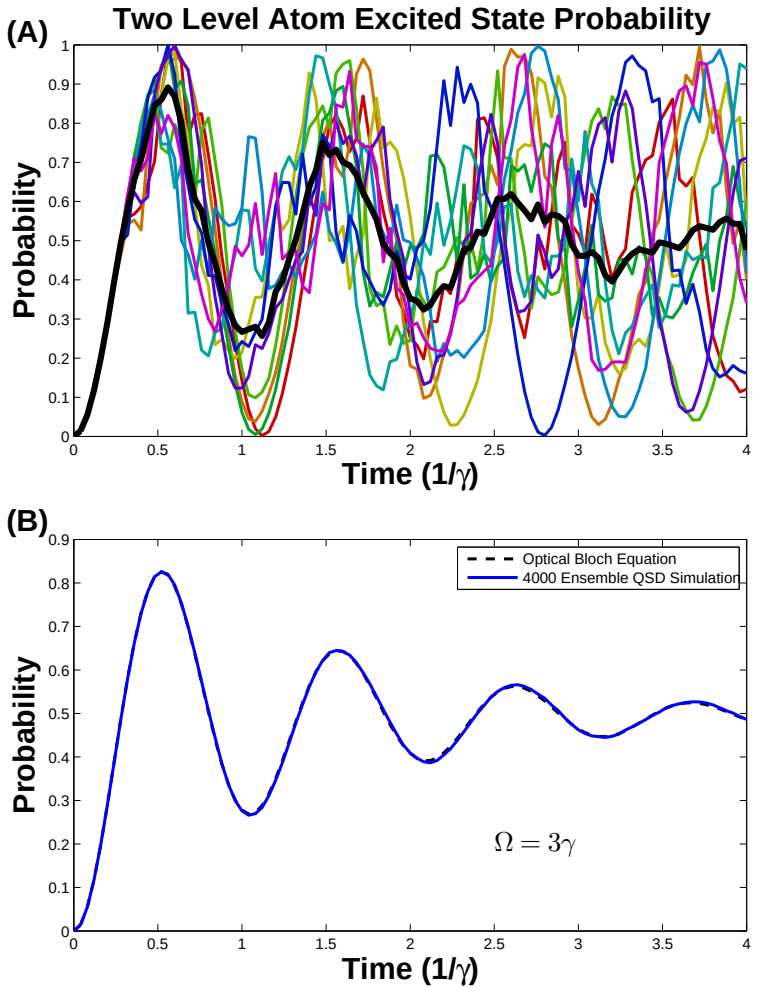

Figure 4.1: Two Level Atom Excited State Population. (A) The first 10 individual trajectories from the QSD simulation. The average of the first 10 trajectories is shown by the thick black line. (B) The excited state population of a two level atom from the numerical simulation (solid blue line) compared with the analytic solution from the optical Bloch equations (dashed black line) for the case of $\Omega = 3\gamma$ for 4000 trajectories.

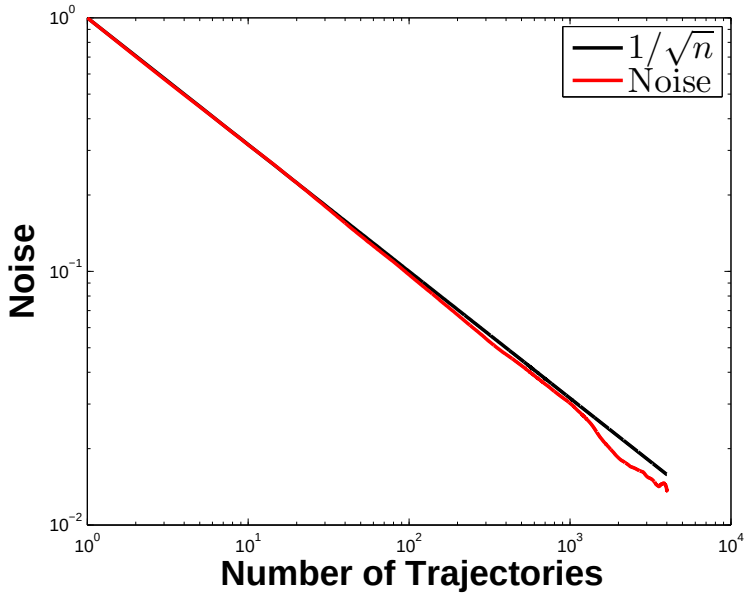

Figure 4.2: The noise decreases with the number of trajectories like $1/\sqrt{n}$ where n is the number of trajectories.

4.2.2 One Harmonic Oscillator

Next, we looked at the expected behavior for one thermal harmonic resonator. We ran three cases with 400 trajectories each to test the different aspects of the numerical implementation.

The first case is a harmonic resonator that was already thermalized to the temperature of the thermal bath. The initial state used here is a Fock state, $|n = 3\rangle$. In this case, we expect the occupation number of the resonator to remain constant at the thermal bath temperature, which corresponds to an $\bar{n} = 3$ thermal state here. This is exactly what we see in Figure 4.3(A).

The second case is a harmonic resonator that is initially occupied at $n = 3$, but is connected to a zero temperature bath. In this case, we expect to see the occupation number decay exponentially to the bath temperature, as illustrated by our results in Figure 4.3(B).

The third case is a harmonic resonator that is initially empty ($n = 0$) and is connected to a bath with temperature corresponding to a thermal occupancy of $\bar{n} = 2$. In this case, we expect the occupation number to exponentially increase at a rate determined by $\gamma_m \bar{n}$ until the resonator thermalizes with the bath. This is what we observed, as shown in Figure 4.3(C).

4.2.3 Sideband Cooling

Next, we looked at two and three coupled harmonic resonators with a red detuned pump field, where only the mechanical resonator is coupled to a thermal bath. In this case, we get cooling of the mechanical resonator as we saw in Section 2.1 The mechanical resonator is losing phonons to decay and to the other resonators, but it is also gaining phonons from the thermal bath. So the final equilibrium temperature will be non-zero.

Figure 4.4(A) shows the cooling for the electromechanical system for 500 trajectories in the case where $\gamma_m = \gamma_\mu$. As the two resonators come into equilibrium with each other they arrive at equal steady-state occupation numbers which is approximately half of the thermal bath temperature $\bar{n} = 3$. This is because the state spends approximately half of the time in the mechanical resonator where it can be affected by the thermal bath. Also, the rate of phonons being absorbed from the

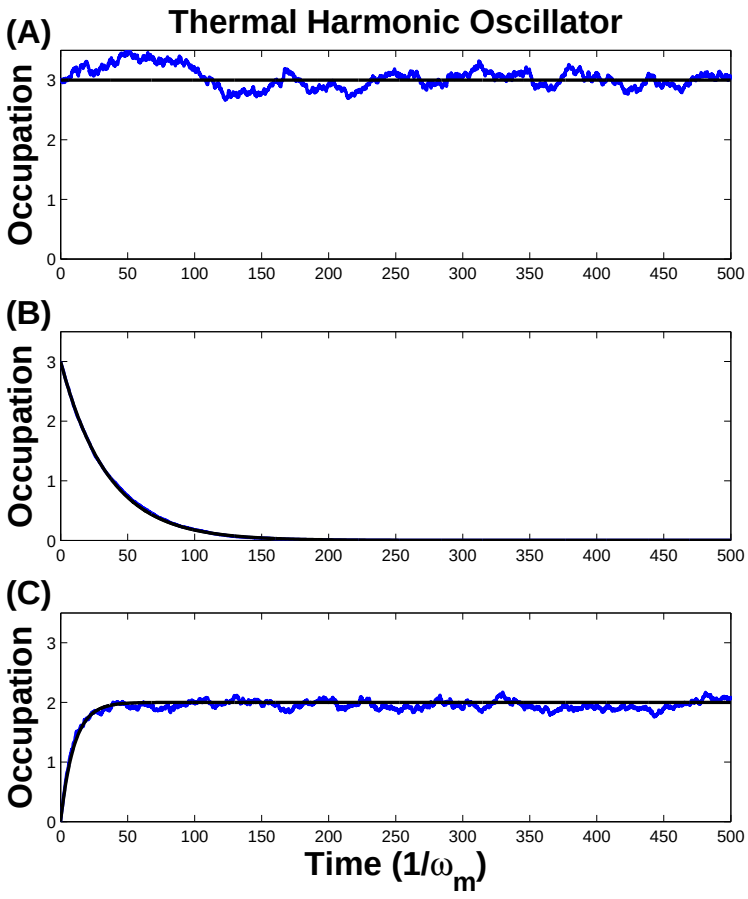

Figure 4.3: The occupation number of one thermal harmonic resonator (blue line) vs. the theoretical prediction (black line). (A) The case where the resonator starts out thermalized to the bath temperature corresponding to $n = \bar{n} = 3$ and thus remains at that temperature. (B) The case where the resonator is initially occupied at $n = 3$ but is connected to a zero temperature bath and thus decays to zero temperature. (C) The case where the resonator is initially empty ($n = 0$) and is connected to a hotter bath with temperature corresponding to $\bar{n} = 2$ and thus exponentially increases until it thermalizes with the bath. The number of trajectories used in all these cases was 400.

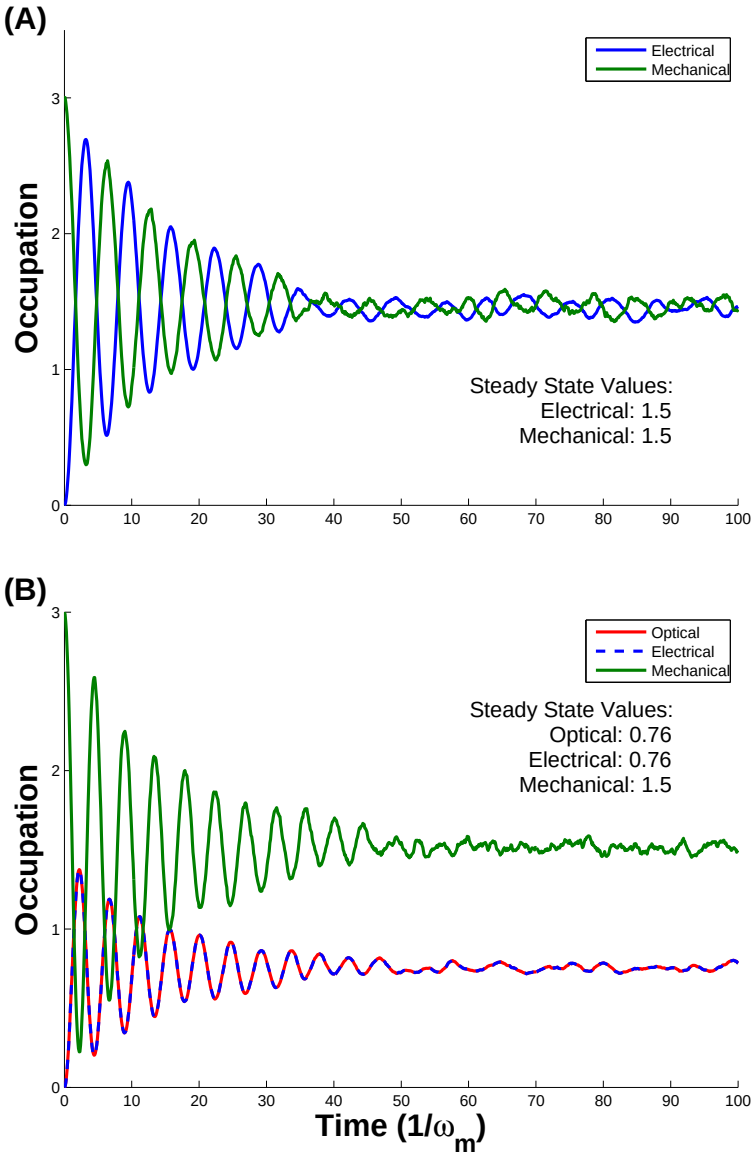

Figure 4.4: Cooling coupled harmonic resonators for 500 trajectories. (A) The case for an electromechanical system where $\gamma_m = \gamma_\mu$. (B) The case for an electro-opto-mechanical system where $\gamma_m = \gamma_\mu = \gamma_o$. In both cases, the thermal bath temperature corresponds to $\bar{n} = 3$.

thermal bath is equal to the rate of phonons being transduced to photons in the microwave cavity where they are lost to the zero temperature bath.

Figure 4.4(B) shows the cooling for the electro-opto-mechanical system for 500 trajectories where $\gamma_{(o,\mu)} = \gamma_m$. We have set the electromechanical coupling to be equal to the optomechanical coupling. Thus, the steady state occupation of the microwave and optical resonators is half of the occupation of the mechanical resonator because the phonons are transferred at equal rates into each of the other two resonators.

In contrast, Figure 4.5 shows the cases for two (subplot (A)) and three (subplot (B)) coupled resonators where $\gamma_{(o,\mu)} \gg \gamma_m$. In these cases, the state will decay out of the microwave and optical cavities much faster than the mechanical resonator is absorbing phonons from its thermal bath. So the mechanical resonator will cool to its ground state.

4.2.4 Blue Detuned Pump

Next, we look at the case of a blue detuned pump field with two coupled resonators. In this case, we expect exponential heating in both resonators. From the Hamiltonian, Eq. 2.30, we expect correlated pairs of photons and phonons to be generated. Figure 4.6(A) shows the occupation numbers for both resonators growing exponentially with a zero number difference for positive values of the coupling strength and decaying exponentially for negative values of the coupling strength. Subplot (B) shows the coupling strength. Setting the coupling to be negative is equivalent to time reversal, so the observation of decay can be anticipated. Subplot (C) shows that the variance of the number difference is zero for all times, indicating that photons/phonons are produced in correlated pairs at all times.

4.3 Summary

The Quantum State Diffusion method is a versatile way to unravel the density matrix master equation into pure state trajectories that can be evolved independently. The total state is found by the ensemble average of these individual trajectories. We found that the QSD approach was

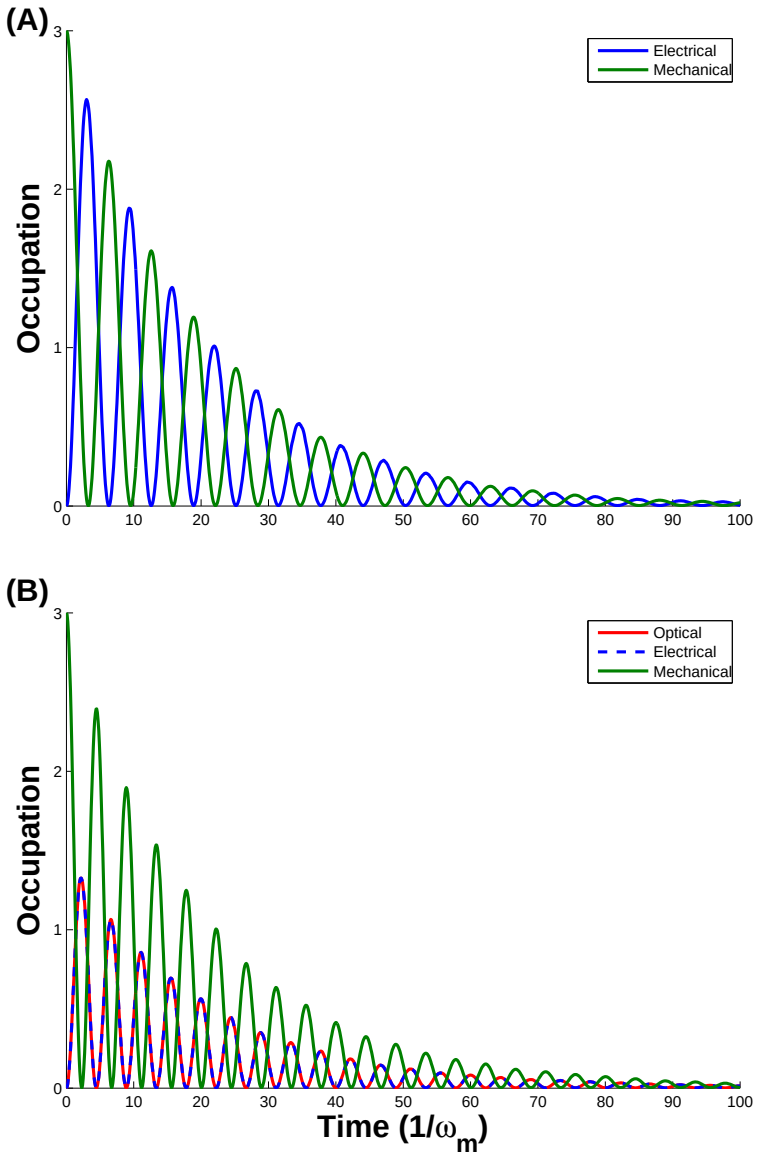

Figure 4.5: Cooling coupled harmonic resonators to the ground state. (A) The case for an electromechanical system where $\gamma_\mu \gg \gamma_m$. (B) The case for an electro-opto-mechanical system where $\gamma_{(o,\mu)} \gg \gamma_m$. In both cases, the thermal bath temperature corresponds to $\bar{n} = 3$.

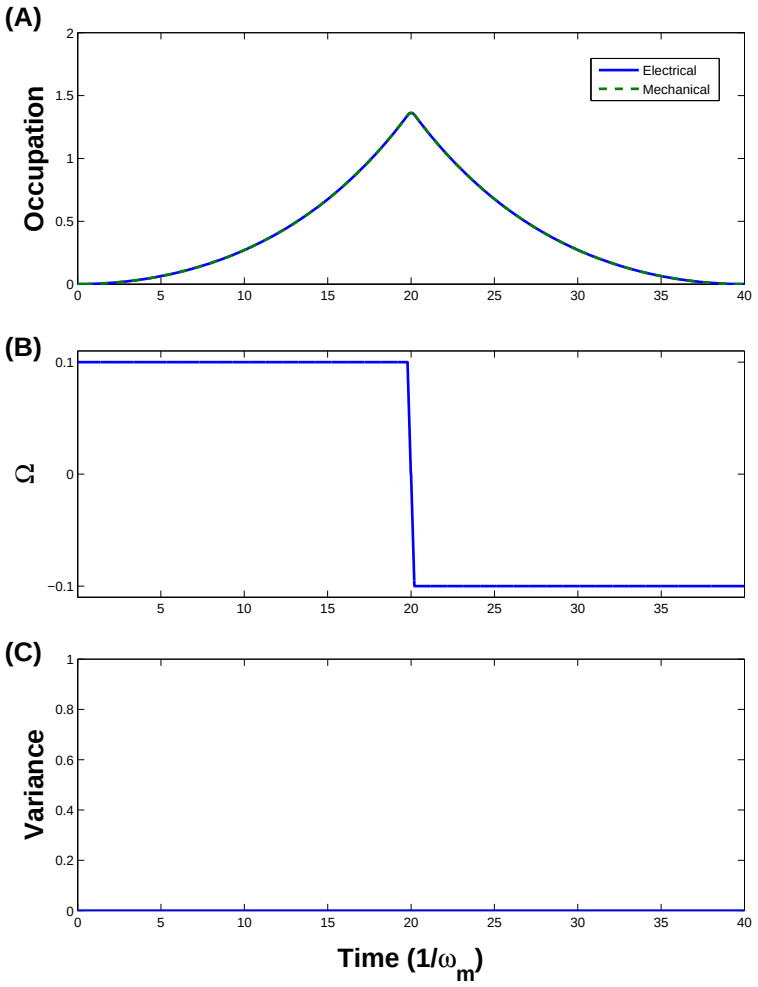

Figure 4.6: Blue Detuned Occupation and Variance. (A) The number of photons/phonons in each resonator. (B) The coupling strength. When the coupling is positive, the number grows exponentially. When it is negative, it decays exponentially, until it hits zero, then grows exponentially again. (C) The variance in the number difference, $\Delta w = \langle \left(\hat{b}^\dagger \hat{b} - \hat{d}^\dagger \hat{d} \right)^2 \rangle - \left(\langle \hat{b}^\dagger \hat{b} \rangle - \langle \hat{d}^\dagger \hat{d} \rangle \right)^2$, remains zero indicating that photons/phonons are produced in correlated pairs at all times.

particularly suited to our system of three coupled harmonic resonators. We used several test cases to verify that our computational implementation of the QSD method was done correctly.

Chapter 5

Quantum Memory: Storage and Retrieval

One of the possible applications of this system is to store a quantum state in the mechanical resonator. One could prepare the microwave resonator in any of a variety of quantum states. This can be done with superconducting quantum circuits or other experimental setups such as those described in [22, 19, 43, 14]. Then, the states of the microwave and mechanical resonators could be swapped using a "π-pulse", effectively storing the quantum state in the mechanical resonator. At some later time, another swap could be done to put the state back into the microwave resonator where it can be retrieved [49, 40]. The objective would be to maintain high fidelity of the quantum state involved. These swaps are achieved by varying the coupling constant, $\Omega_{(o,\mu)}$ which behaves like a Rabi frequency in the beam splitter Hamiltonian, Eq. 2.27. As we saw in Eqs. 2.23 and 2.24, the coupling constants can be changed by modulating the bare coupling constants $g_{(o,\mu)}$ or the pump amplitude $A_{(o,\mu)}$, or the detuning $\Delta_{(o,\mu)}$. For this problem, it is sufficient to consider just a pair of resonators. We reduce the system to one electromagnetic resonator and one mechanical resonator by setting one of the coupling constants to zero.

A "π-pulse" in this context is a pulse where the time integral over the coupling constant in frequency units is π. For the Gaussian coupling pulses, $\Omega(t) = \Omega e^{-(t-t_c)^2/(w^2\pi)}$, that we employ, the pulse area is $w\pi\Omega$ where $w\pi$ is the width of the Gaussian and the peak amplitude is Ω. The pulse sequence is schematically shown in Figure 5.1(A). The first π pulse is the storage pulse. The second π pulse is the retrieval pulse. The sign of the coupling constant for retrieval must be the opposite of the sign for storage in order to cancel the phase accumulation during the pulses. Also, the width

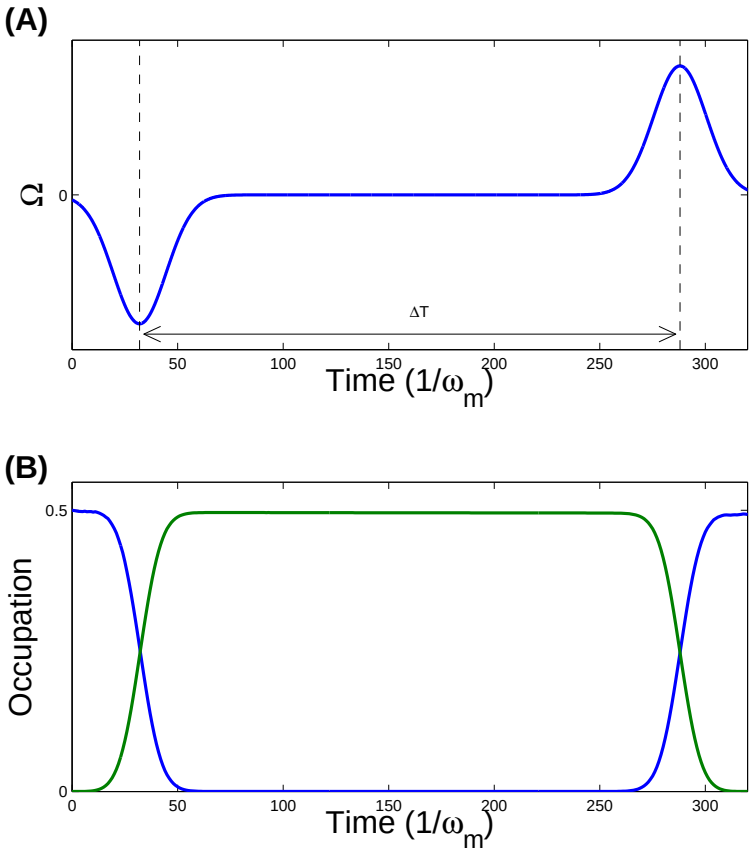

Figure 5.1: Quantum memory pulse sequence and occupation for the case of $\Delta T = 160(1/\omega_m)$. (A) A schematic diagram of the coupling π pulse sequence for Quantum State Memory tests. The sign of the coupling constant for retrieval must be the opposite of the sign for storage in order to cancel the phase accumulation during the pulses. (B) The occupation numbers for the microwave and mechanical resonators throughout the memory pulse sequence. The actual storage time is reduced by the width of the Gaussian pulses.

of the π pulse must be short compared to the mechanical decay rate γ_m otherwise, the state may decay before it can be swapped to the other resonator. Subplot (B) shows the occupation numbers of both resonators throughout the sequence. The first pulse swaps the state from the microwave resonator to the mechanical resonator. The second pulse swaps the state back into the microwave resonator. It takes approximately the width of the π pulse before the state is fully in the mechanical resonator. Thus, the actual storage time of the state in the mechanical resonator is approximately the separation time between the peaks of the pulses (ΔT) reduced by the width of the pulses.

If we move the pulses as close together as possible (shown in Figure 5.2 for $\Delta T = 64(1/\omega_m)$), then the peak separation ΔT will be approximately twice the width of the Gaussian π pulses. Even though there is no time between the end of the storage pulse and the beginning of the retrieval pulse, the state is still in the mechanical resonator for approximately the width of the π pulse, which for all the quantum memory cases is $w\pi = \pi/\Omega_\mu = \pi/(0.1\omega_m)$.

To see how well the system is able to store classical and quantum states, we study a variety of initial states with the same pulse sequence for storage and retrieval. Recall that these states in fact represent the phonon or photon fluctuations around the stationary value of each resonator, as we have previously described in the derivation of the linearized effective Hamiltonian, Eq. 2.27.

We use coherent states $|\alpha\rangle|n\rangle_m$, squeezed coherent states $|\alpha,\xi\rangle|n\rangle_m$, cat states $|\psi_{cat}\rangle$, and a superposition of Fock states $|\psi_{SF}\rangle$ as inputs to the microwave resonator. The squeezed coherent state [44] is a displaced squeezed vacuum state, $|\alpha,\xi\rangle = \hat{D}(\alpha)\hat{S}(\xi)|0\rangle$, where α is the mean value and ξ is the squeezing parameter. The displacement operator is $\hat{D}(\alpha) = e^{\alpha\hat{a}^\dagger - \alpha^*\hat{a}}$ and the squeezing operator is $\hat{S}(\xi) = e^{\frac{1}{2}(\xi^*\hat{a}^2 - \xi(\hat{a}^\dagger)^2)}$.

The cat state is $|\psi_{cat}\rangle = N(|\alpha\rangle + |-\alpha\rangle)|n\rangle_m$ where N is a normalization constant. The input state for the superposition of Fock states that we will study is $|\psi_{SF}\rangle = \frac{1}{\sqrt{2}}(|0\rangle_\mu + |1\rangle_\mu)|n\rangle_m$, where $|i\rangle_\mu$ indicates the photon fluctuations around the stationary value inside the microwave cavity and $|n\rangle_m$ indicates the phonon fluctuations around the stationary value inside the mechanical resonator.

The initial Fock state for the mechanical resonator for all input states, $|n\rangle_m$, is randomly chosen according to the probability distribution for a thermal state, $P_n = \bar{n}^n/(\bar{n}+1)^{n+1}$ in order

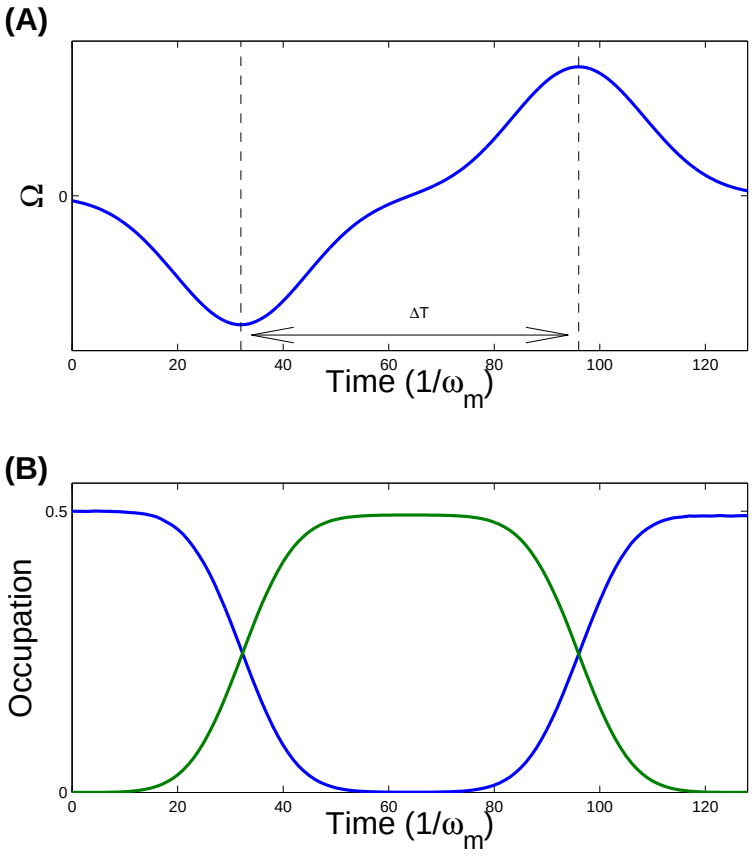

Figure 5.2: Quantum memory pulse sequence and occupation for the case of $\Delta T = 64(1/\omega_m)$. (A) The coupling π pulse sequence. The separation between the pulses here are approximately twice the width of the each pulse ($\Delta T \approx 2w$). Thus, the pulses are as close together as they can be. (B) The occupation numbers for the microwave and mechanical resonators throughout the memory pulse sequence. The actual storage time is reduced by the width of the Gaussian pulses.

to sample the thermal density matrix at a temperature corresponding to $\bar{n}$.

5.1 Increasing Decay Rates

Figure 5.3(A) shows the memory fidelity at zero temperature for the input states $|\alpha\rangle$, $|\psi_{SF}\rangle$, and $|\psi_{cat}\rangle$ for $\Delta T = 64(1/\omega_m)$. The coherent state fidelity agrees well with our analytical result in Eq. (3.20) except at very low Q. At low Q values, the input state thermalizes quickly to a thermal state. For these low Q values, the decay time is larger than the pulse width. Even though there is almost no time between the pulses for these cases, the state still thermalizes during the pulse width. A thermal state has a constant fidelity overlap with the initial state. Thus, the fidelity for low Q mechanical resonators levels off to a constant value. This causes the actual fidelity to deviate from the analytic formula. Across the range of Q_m values considered in Figure 5.3, the non-classical states have lower fidelities than the coherent state.

The fidelities for a finite temperature corresponding to $\bar{n} = 3$ are shown in Figure 5.3(B). As expected, the fidelities are consistently reduced by the thermal noise. At the current experimental values for the mechanical quality [39] (far right hand side of the plots), all the fidelities are above 99% and there is little difference between the various input states.

For the squeezed states $|\alpha, \xi\rangle$, shown in Figure 5.4, we varied the squeezing parameter ξ, keeping α constant at $\alpha = 1$. For $\xi = 0$ the input state is just the coherent state, so the data is similar to the coherent state data. The solid red line is the analytic formula from Eq. 3.20 showing good agreement with the no squeezing, $\xi = 0$, input state. As the squeezing increases, the input state becomes more and more nonclassical. For low-Q cavities, the mechanical resonator quickly decays to a thermal state that is farther and farther away from the initial squeezed state. This causes the fidelity for these highly squeezed states to go to zero.

5.2 Increasing Wait Time

Next, we look at how long the mechanical resonator can store a quantum state before significant degradation occurs. Figure 5.5 shows the memory fidelity of $|\psi_{SF}\rangle$ for increasing wait times as

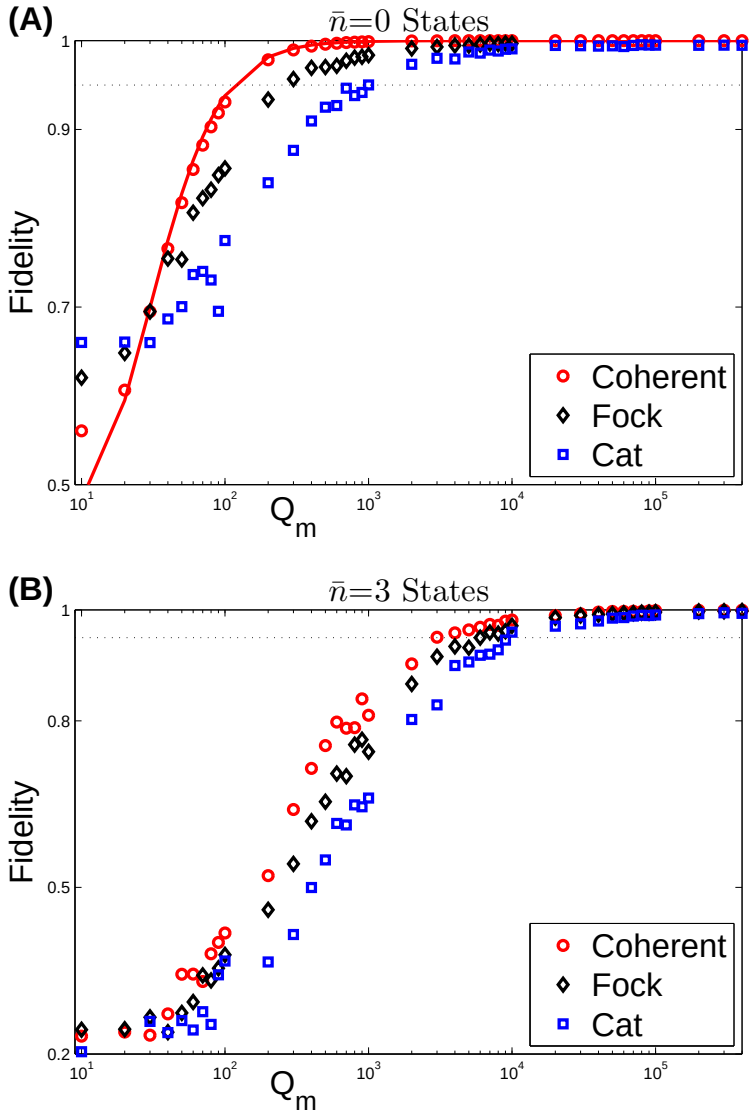

Figure 5.3: (A) Memory fidelity vs. mechanical resonator quality for input states $|\alpha\rangle$ (red circles), $|\psi_{SF}\rangle$ (black diamonds), $|\psi_{cat}\rangle$ (blue squares) for $\bar{n} = 0$. The solid red line is the analytic formula from Eq. 3.20. (B) The same as A except for $\bar{n} = 3$. In all cases, $\Delta T = 64(1/\omega_m)$. The horizontal dotted black line indicates 95% fidelity.

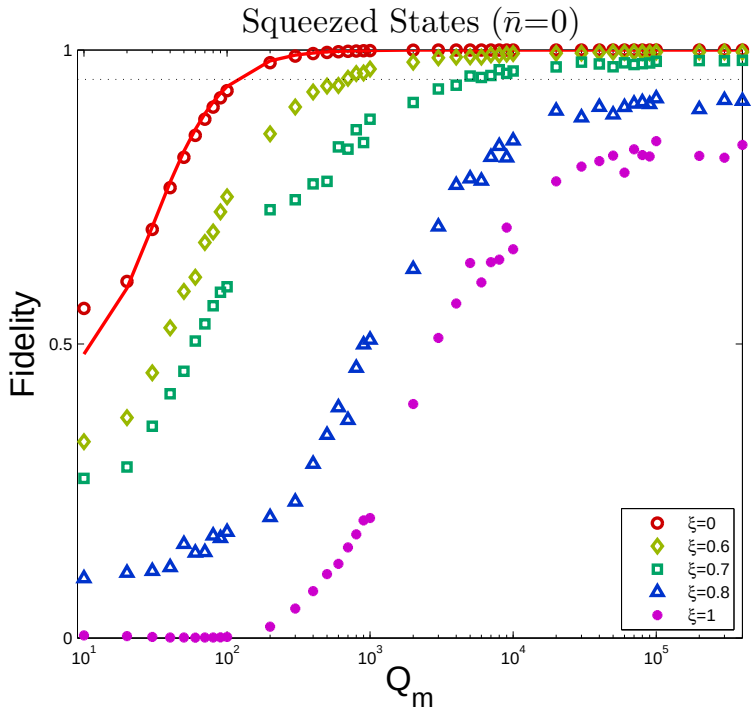

Figure 5.4: The memory fidelity vs. quality for squeezed states $|\alpha, \xi\rangle$ with $\alpha = 1$ and $\bar{n} = 0$ for various squeezing parameters ξ. In all cases, $\Delta T = 64(1/\omega_m)$. The solid red line is the analytic formula for a coherent state from Eq. 3.20.

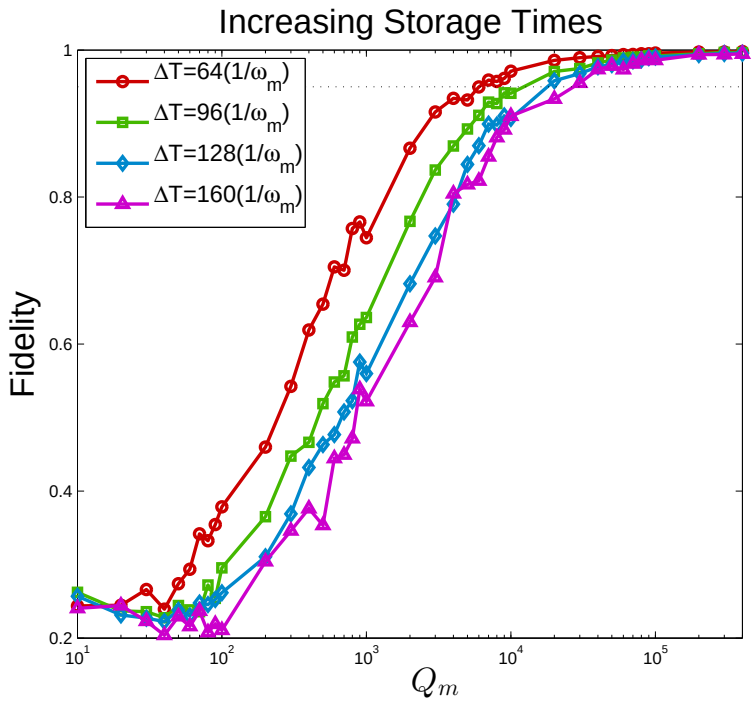

Figure 5.5: Memory fidelity vs. mechanical resonator quality for various wait times with $\bar{n} = 3$ for $|\psi_{SF}\rangle$. The fidelity decreases exponentially with decreasing Q and with increased wait times. At low-Q, the fidelity saturates to that of a thermalized state overlapping with the initial state.

a function of Q_m for $\bar{n} = 0$. As expected, the longer the state is stored in the mechanical resonator, the more the fidelity degrades. However, we can still achieve above a 95% fidelity for the higher Q_m values.

Taking a cue from the coherent case, where we found a universal curve for the zero temperature fidelity (Eq. 3.28), we employ a dimensionless variable scaled by the thermal average occupation number $\bar{n}$,

$$\zeta_o = \omega_m(\Delta T - \frac{\pi}{\Omega_\mu})/Q_m \tag{5.1}$$

$$\zeta = \omega_m(\Delta T - \frac{\pi}{\Omega_\mu})\bar{n}/Q_m \ , \tag{5.2}$$

to rescale the Fock state fidelity data. We subtract the width of the π pulses to more accurately reflect the actual storage time. Figure 5.6(A) shows the same memory fidelity versus ζ_o for $\bar{n} = 0$. Figure 5.6(B) shows the memory fidelity versus ζ for finite $\bar{n}$ in order to remove the dependence on the temperature. As we increase the wait time before the second π pulse, the fidelity decreases exponentially as expected. By removing the dependence on the temperature, the fidelity curves all collapse onto one universal curve. This universal curve for Fock states is similar to the universal curve we found for coherent states in section 3.2.2.

All the input states in Figure 5.3 reach above a 95% fidelity for ζ_o values below about 0.26 for coherent states, 0.11 for Fock states, and 0.04 for Cat states for $\bar{n} = 0$. The fidelity is above 95% for ζ values below 0.03 for coherent states, 0.02 for Fock states, and 0.01 for Cat states for $\bar{n} = 3$ with the peak coupling set to $\Omega_\mu = 0.1\omega_m$.

The distribution of the fidelities over the individual stochastic QSD trajectories is not Gaussian and thus the mean and variance are not representative of the outcome of a single run. In an experiment, many runs must be performed to get good statistics about the memory transfer fidelity. However, as the mean fidelity increases, the distribution becomes more and more narrow and thus more repeatable. Figure 5.7 shows the fidelity distribution for $|\psi_{SF}\rangle$ for $Q_m = 10,000$, $Q_m = 1000$, $Q_m = 500$, where the wait time is $\Delta T = 64\frac{1}{\omega_m}$, $\bar{n} = 3$, and the peak coupling is $\Omega_\mu = 0.1\omega_m$ for 1000 trajectories.

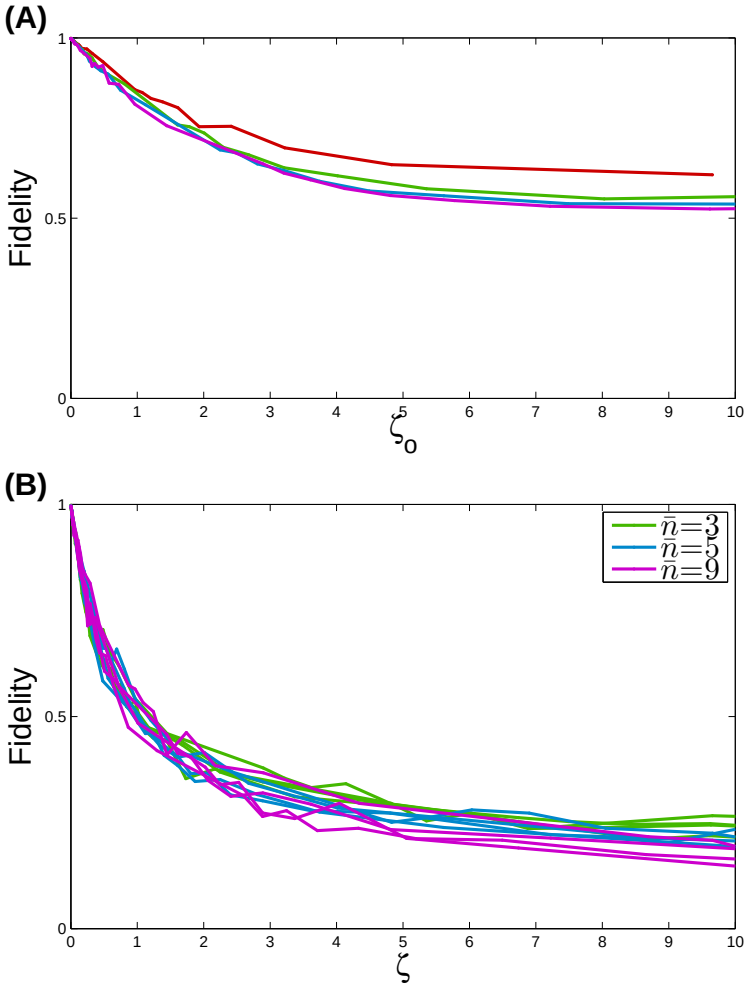

Figure 5.6: (A) The memory fidelity vs. scaled wait time with $\bar{n} = 0$ for $|\psi_{SF}\rangle$. (B) The memory fidelity vs. scaled wait time for different temperatures showing how all the curves collapse onto one universal curve. In all cases, the peak coupling is $\Omega_\mu = 0.1\omega_m$.

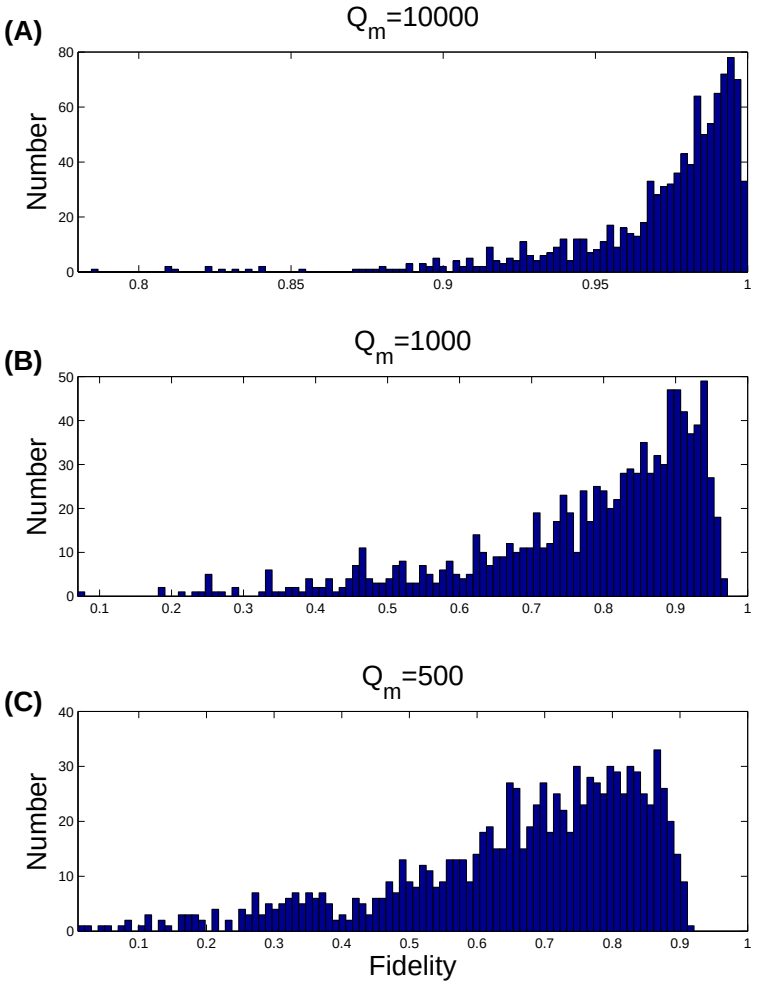

Figure 5.7: Distribution of fidelities for $|\psi_{SF}\rangle$ for $Q_m = 10,000$ (A), $Q_m = 1000$ (B), and $Q_m = 500$ (C) for 1000 independent QSD trajectories. In all cases, $\Delta T = 64\frac{1}{\omega_m}$, $\bar{n} = 3$, and the peak coupling is $\Omega_\mu = 0.1\omega_m$. Note the different horizontal axis in each plot.

5.3 Increasing Coupling Strength

We now examine the effect of increasing the coupling strength, Ω_μ. This will make the Gaussian pulses higher and narrower. Each pulse maintains a pulse area of π as required for the swap to be perfect. We expect the fidelity to improve with increasing coupling strength because there is less decay and thermal noise during the shorter pulses. This is what we see in Figure 5.8 showing the fidelity for increasing coupling strength for $\bar{n} = 0$ and $\bar{n} = 3$ for the representative case of $Q_m = 1,000$ and $\Delta T = 64\frac{1}{\omega_m}$. At the coupling strengths used throughout this thesis, $\Omega_\mu = 0.1\omega_m$ (the highest currently achievable experimental values), there is a significant difference between the fidelities at zero temperature and at higher temperatures. However as the coupling strength increases, the difference becomes less and less significant. This trend is the same for any storage time and mechanical quality.

5.4 Summary

Quantum storage and retrieval is possible for a variety of input states, both classical and quantum. At the current experimental Q values of about $Q_m = 360,000$ [39] the quantum state can be stored in the mechanical resonator for longer than $\Delta T = 160(1/\omega_m)$ at low temperatures. As the experiments improve the coupling strength, the fidelity will increase allowing longer storage times at higher temperatures.

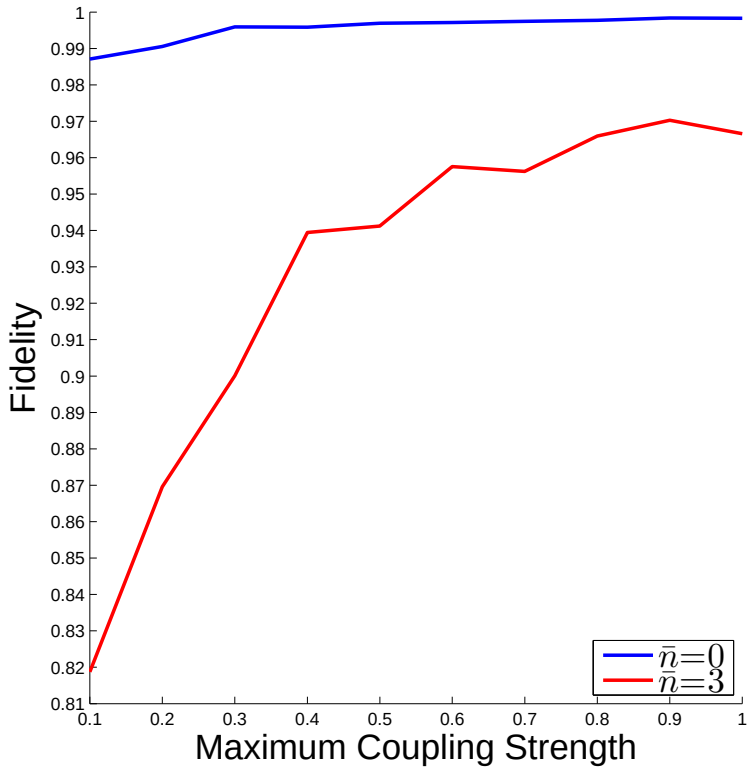

Figure 5.8: The memory fidelity for increasing coupling strength. The π pulses used in the memory scheme for each data point have a maximum amplitude as indicated by the x axis. The width of the pulse decreases in order to keep the pulse area constant. Here $Q_m = 1,000$ and $\Delta T = 64\frac{1}{\omega_m}$.

Chapter 6

Quantum Transduction

We turn now to the problem of transducing the quantum state from the microwave domain to the optical domain via the mechanical resonator, or vice versa. This situation is formally equivalent to the quantum memory case if the electromechanical coupling pulse and the optomechanical coupling pulse do not overlap. This is because transduction can be realized by two sequential steps from one resonator to the mechanical resonator and then to the second resonator, playing the same roles as storage and retrieval in the previously studied case of quantum memory. However, with three resonators, more varied protocols are also possible. Although we specialize our analysis to the case where the initial state is in a superposition of Fock states, which now also contains the optical vacuum state, *i.e.*, $|\psi_t\rangle = \frac{1}{\sqrt{2}}(|0\rangle_\mu + |1\rangle_\mu)|n\rangle_m|0\rangle_o$, these procedures could be similarly applied to consider other quantum states.

The coupling parameters can be of similar orders of magnitude for optical and microwave cavities. So, to simplify the analysis and also for impedance matching, we set the respective optical and microwave coupling parameters equal to each other, $\Omega_o = \Omega_\mu = 0.1\omega_m$. In addition, we set both optical and microwave detunings equal to the mechanical resonator frequency.

6.1 Separated Pulse Scheme

For transduction, we want to minimize the decoherence and thermal effects caused by leaving the quantum state of interest in the mechanical resonator for any appreciable time period. The simplest method to accomplish this is to move the quantum state through the mechanical resonator

as quickly as possible. This method would be good for applications such as quantum information processing where speed is desirable.

Another method is to adiabatically move the state from the microwave to the optical resonator or vice versa without fully populating the mechanical resonator utilizing the concepts from STIRAP in atoms. Naturally, adiabaticity requires longer times and hence could eventually run into limits associated with the microwave and optical cavity decay that we do not include here. But, it is also less susceptible to variations in the pulse profiles. We will discuss this method in more detail in section 6.4.

We begin by considering a similar protocol to the quantum memory scheme. We set the first π pulse to swap the state from the microwave cavity to the mechanical resonator. Then, we set the second π pulse to occur right after the first one to swap the state from the mechanical resonator to the optical cavity. This pulse sequence is shown schematically in Figure 6.1(A).

The resulting fidelity is shown by the red dots in Figure 6.2 as a function of the Q of the mechanical resonator. As this is formally equivalent to the memory scheme, we see similar behavior. The separation between the peaks of the π pulses used here is the same as the wait time we used for the quantum memory scheme. Thus, the numerical data are similar. Just like in the quantum memory case, as the mechanical quality decreases, the thermal noise and decay processes become more significant and the fidelity exponentially decays down to the fully thermalized value.

6.2 Simultaneous Pulse Scheme

A natural extension of this scheme is to move the two π pulses closer together, which could allow for faster transfer. Taking this to its logical extreme, we study a scheme where both coupling pulses occur simultaneously. This allows for the quantum state to move from the microwave to optical cavity, or vice versa, without fully occupying the mechanical resonator, but note, that this in not in the adiabatic regime. The overlap in the coupling modifies the optimal pulse area of both couplings. Both of these pulses must now have a pulse area of $\sqrt{2}\pi$. This is shown schematically in Figure 6.1(B).

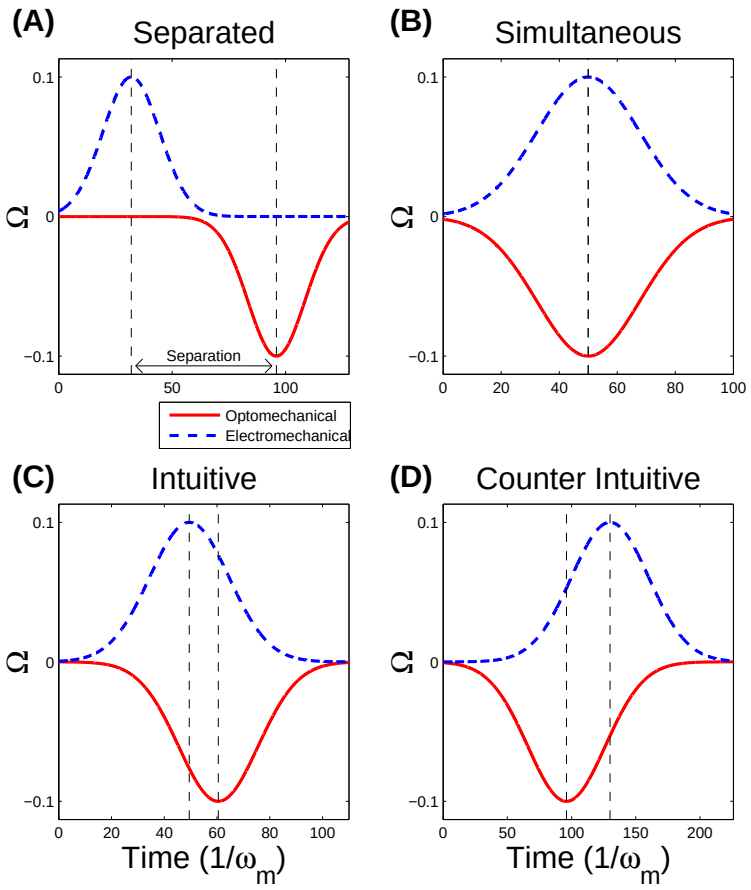

Figure 6.1: Transduction Pulse Sequences. (A) A schematic representation of separated coupling pulses. (B) A schematic representation of simultaneous coupling pulses. (C) A schematic representation of intuitive partially overlapping coupling pulses. (D) A schematic representation of counter-intuitive partially overlapping coupling pulses.

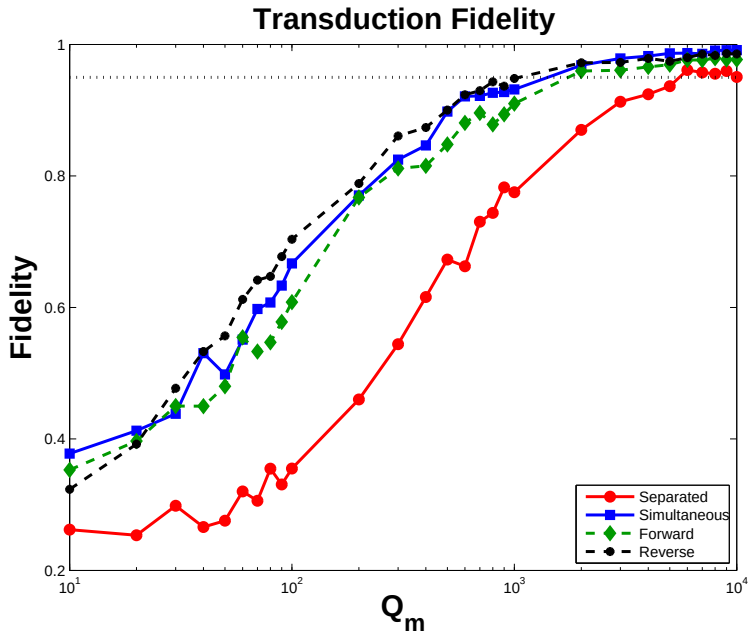

Figure 6.2: Transfer fidelity vs. mechanical oscillator quality for $|\psi_t\rangle$ for the separated pulse scheme with $\Delta T = 64(1/\omega_m)$ (red dots), the simultaneous pulse scheme (blue squares), intuitive pulse scheme (green diamonds), and counter-intuitive pulse scheme (black stars). For this case, $\bar{n} = 3$ and the number of trajectories is 100.

This scheme achieves significantly higher fidelities than the separated pulse scheme for all Q values. The fidelity is shown in Figure 6.2 by the blue squares. In the low-Q regime, the decay and thermal noise processes become increasingly more significant. However, the population going through the mechanical resonator is smaller, so the effect is lessened. Also, there is no waiting time between the pulses for decay and thermal noise processes to occur. The only decay happens during the width of the pulse. Thus, the simultaneous pulse scheme is more robust against these processes.

To illustrate the differences between the separated and simultaneous pulse schemes, we examine the populations in each of the three resonators throughout the swapping process. Figure 6.3(A) shows how the populations change for the separated π pulse scheme. As expected, the state in the electrical resonator moves into the mechanical resonator and then into the optical resonator. In contrast, Figure 6.3(B) shows populations for the simultaneous π pulse scheme. Here, the state transfers from the electrical resonator to the optical resonator without ever fully populating the mechanical resonator.

6.3 Intuitively Ordered Overlapping Pulse Scheme

As the pulses move closer together, the pulse area needed to make the swap smoothly changes from π to $\sqrt{2}\pi$. Also, in real experiments, there may be slight imperfections in the pulse preparation that would result in varying pulse areas and peak separations. We have run our simulations over a range of varying pulse areas and separations to investigate the effect this had on the fidelity.

Figure 6.4 shows the transduction fidelity versus the pulse area and the peak separation between the two coupling pulses for $\bar{n} = 0$ and $Q_m = 100,000$ for the superposition of Fock states, $|\psi_t\rangle$. This plot is very similar to the plot in Figure 3.5 for the transduction fidelity of a coherent state. Just as in that case, the x values represent the separation between the peaks of the two coupling pulses as a percentage of the total transduction sequence time as shown in Figure 6.1. The zero on the x axis is the point where the two coupling pulses occur simultaneously. The positive x values represent peak separations that are "intuitive", *i.e.*, the electromechanical

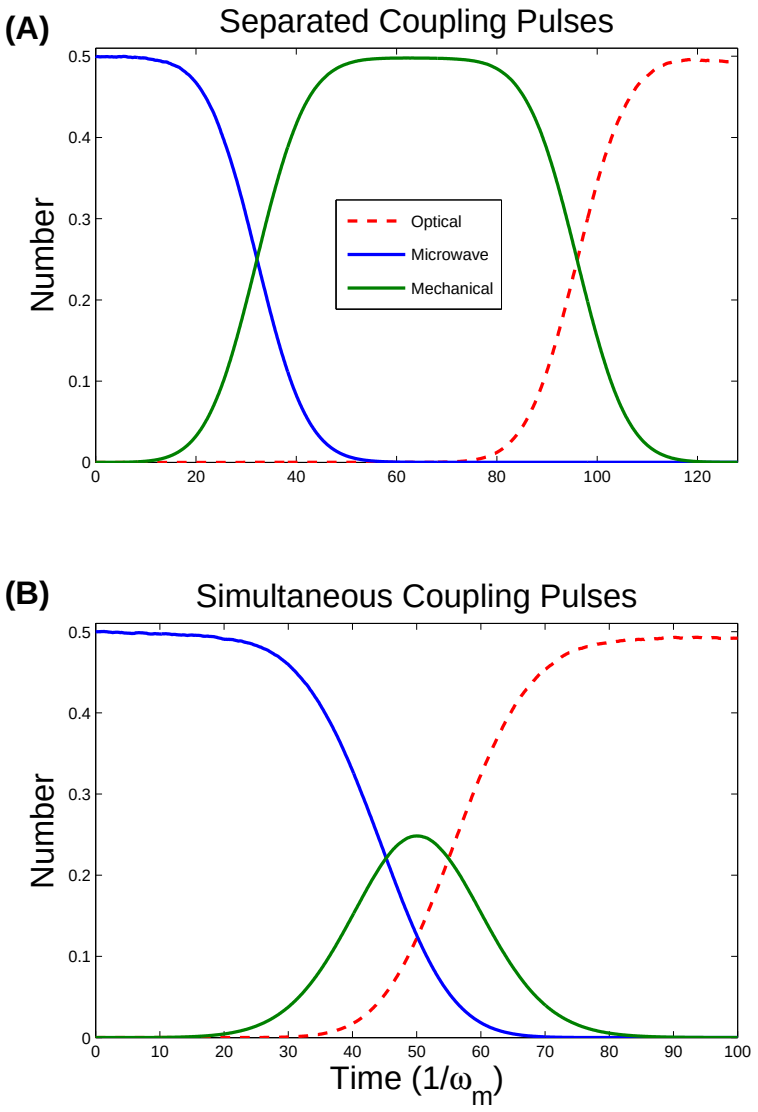

Figure 6.3: Transduction Occupation Numbers. (A) Number of photons or phonons in each oscillator for intuitive, separated coupling pulses with $\Delta T = 64(1/\omega_m)$. (B) Number of photons or phonons in each oscillator for simultaneous coupling pulses.

coupling pulse occurs before the optomechanical coupling pulse. A representative intuitive pulse sequence is shown in Figure 6.1(C). The negative x values represent peak separations that are "counter-intuitive", *i.e.*, the optomechanical coupling pulse occurs before the electromechanical coupling pulse. A representative counter-intuitive pulse sequence is shown in Figure 6.1(D).

As the intuitive Gaussian pulses move farther apart, they eventually become effectively separated and the distance between them no longer matters, since this is at zero temperature with very low decay rates. This is the area on the far right-hand side of Figure 6.4(A) where the regions of high fidelity level off at odd integer multiples of π. Pulses that are π pulses or an odd integer multiple of a π pulse will swap the state completely from the microwave resonator to the optical resonator. Any other pulse area will not perfectly swap the states. Thus, we see the oscillatory behavior we expect in that part of the plot.

At zero pulse separation, the pulses are identical and the Rabi swapping pulse area is $\sqrt{2}\pi$. Thus, the peak fidelity oscillations are at odd integer multiples of $\sqrt{2}\pi$. For partially overlapping intuitive pulses, the peak fidelity oscillations smoothly drop from the simultaneous values to the separated values.

As we increase the temperature of the mechanical resonator, shown in Figure 6.4(B), the fidelity decreases. The periodic lines of high fidelity still exist, but are narrower. The data in the plot is very coarse grained so the lines of high fidelity are showing up as islands in the contour plot.

The fidelity for a representative partially overlapping intuitive coupling pulse configuration is shown in Fig. 6.2 by the green diamonds. For this case, the pulse area is 1.2π, the peak separation is 10%, and $\bar{n} = 3$. In the next section, we will discuss the counter-intuitive half of Figure 6.4.

6.4 Counter-Intuitively Ordered Overlapping Pulse Scheme

The left half of Figure 6.4(A) shows the transduction fidelity for overlapping coupling pulses that are in the counter-intuitive order, which means, that the optomechanical coupling pulse occurs before the electromechanical coupling pulse. As the peak separation increases, at some point, the pulses become effectively separated and the fidelity goes to zero. However, when the coupling

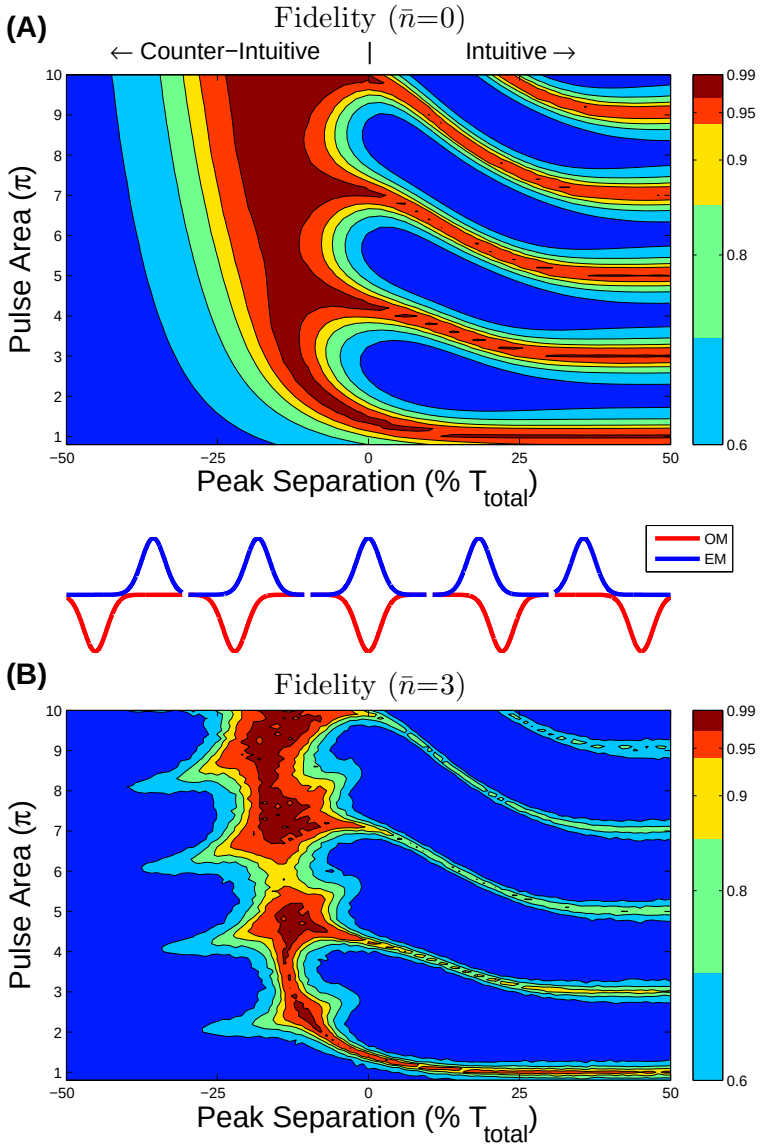

Figure 6.4: The fidelity vs. pulse width and pulse separation for $Q_m = 100000$ with (A) $\bar{n} = 0$ and (B) $\bar{n} = 3$. The negative x values represent the peak separation for counter-intuitively ordered pulses while the positive x values represent the peak separation for intuitively ordered pulses.

pulses are significantly overlapping, there is a large area of high fidelity for any pulse area. As we increase the pulse area, and thus the adiabaticity, the zone of high fidelity transduction increases. This counter-intuitive coupling scheme closely resembles the Stimulated Raman Adiabatic Passage (STIRAP) process in a three level atom that we discussed in section 2.5.

We illustrate, in Figure 6.5, the populations of the three resonators throughout this scheme. Just as we would expect for a STIRAP-like process, the state adiabatically transfers from the microwave to the optical resonator while minimally populating the mechanical resonator. Thus, this scheme is much more robust against decay and thermal noise as well as imperfections in pulse area. However, adiabaticity generally requires longer times. The simultaneous pulse scheme will transduce the state much quicker, but the pulses must be precisely generated. So, there is a trade-off between the transduction time and the strigentness of pulse preparation and also decay during the simultaneous pulse width.

As the temperature increases (Figure 6.4(B)), the region of high fidelity becomes narrower and does not smoothly fall off as it does for zero temperature. We see periodic regions of higher fidelity mirroring the periodic structure on the intuitive half of the graph. To explore why this structure emerges, we examine the populations in the three resonators throughout the process, shown in Figure 6.6. Subplot (A) shows the resonator populations for the zero temperature case. During most of the optomechanical coupling pulse, nothing is changing because there is no population in either the optical or mechanical resonators to swap. Once the electromechanical coupling is turned on, the states begin to swap. The state can only move into the optical resonator as long as both couplings are on. However, the pulse area here is 2π with a peak separation is -24% so the pulse area and overlap is not sufficient to swap the state efficiently. Thus the final fidelity is low.

Subplot (B) shows the resonator populations for a bath temperature corresponding to $\bar{n} = 3$. In this case the mechanical resonator is thermalized to the bath temperature at the beginning of the sequence so there is some population in that resonator to swap with the optical resonator during the optomechanical coupling pulse. Thus, when the electromechanical coupling is turned on and the state in the microwave resonator can move into the optical, there is already some thermal

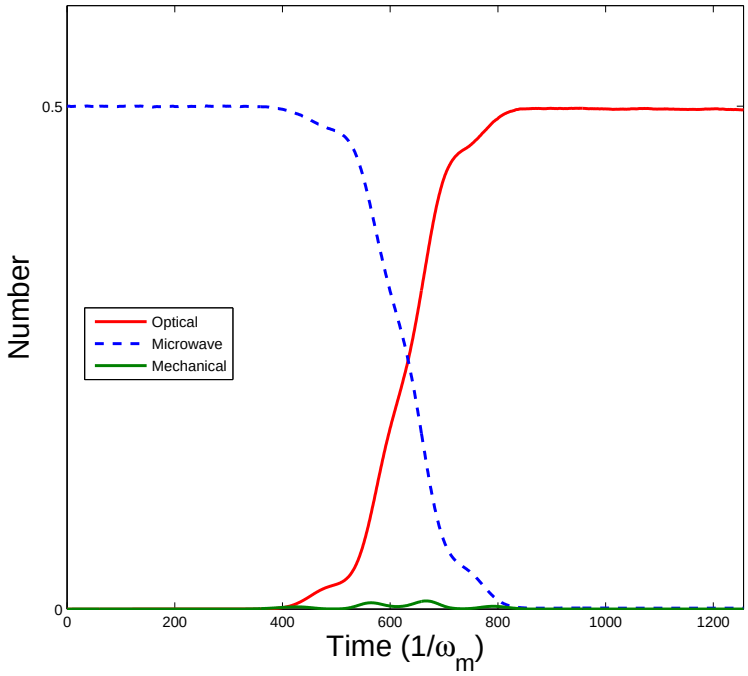

Figure 6.5: The number of photons or phonons in each oscillator for the STIRAP-like coupling pulses for peak separation -14% and pulse area 10π. The population smoothly transfers from the microwave resonator to the optical resonator while minimally populating the mechanical resonator.

decoherence in the optical and mechanical resonators and the starting populations are not zero. This causes the final state to be different from the zero temperature case. Also, if the pulse areas and overlap are such that the optical and mechanical resonator can swap the thermal state perfectly, there will be more thermal state in the optical resonator to add to the microwave initial state that is partially transferred in. Thus, the final fidelity will be higher. This is why we see the periodic behavior on the left hand side of Figure 6.4(B).

A representative counter-intuitive partially overlapping coupling pulse configuration is shown in Figure 6.2 by the black stars. For this case, the pulse area is 2.4π, the peak separation is -15%, and $\bar{n} = 3$.

6.5 Summary

There are many possible protocols to achieve high fidelity quantum state transduction. Intuitively ordered partially overlapping or separated pulses require precise pulse areas to achieve high fidelity. Simultaneous pulses also require precise pulse areas, but achieve high fidelity with short transduction times and are more robust against thermal noise and decay processes than the separated pulse scheme. Adiabatic counter-intuitively ordered pulses have much longer transduction times, but are much more robust against thermal noise and decay processes and the pulse area does not need to be precisely controlled.

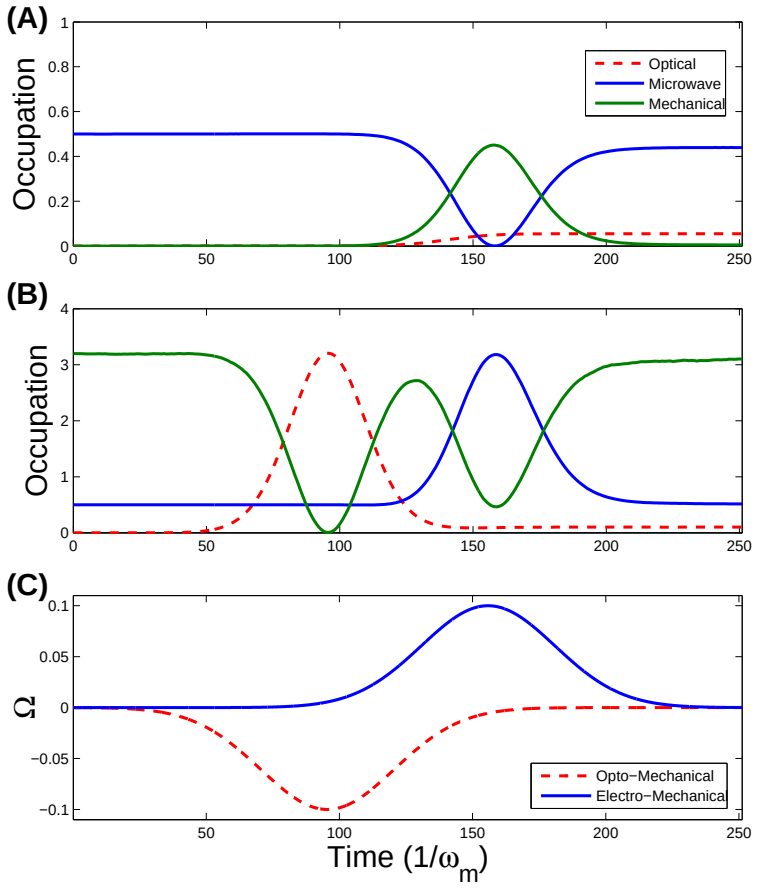

Figure 6.6: The number of photons or phonons in each oscillator for the STIRAP-like coupling pulses for peak separation -24% and pulse area 2π for (A) $\bar{n} = 0$ and (B) $\bar{n} = 3$ illustrating the case of false fidelity readings. (C) The coupling pulse profiles.

Chapter 7

Interferometry

7.1 An Interferometer in Time

The ability to construct analogues of beam splitters and parametric amplifiers allows for the interesting possibility of using the optomechanical system as an interferometer. Figure 7.1 shows a typical Mach-Zehnder type optical interferometer. Such interferometers are setup so that the two input beams mix at a beam splitter (one of which may be in the vacuum state), then propagate independently for some time and then are recombined at a second beam splitter. The two output beams are then detected and the interference fringes recorded. If there is sufficient length difference or induced phase difference in the two free propagation segments, the measured fringes will show this difference. Such interferometers have both classical and quantum limits for the minimum detectable phase shift.

As we described in Chapter 1, the red detuned linearized Hamiltonian in Eq. 2.27,

$$\frac{1}{\hbar}\hat{H}_{\rm eff} = \Delta_o \hat{a}^\dagger \hat{a} + \Delta_\mu \hat{b}^\dagger \hat{b} + \omega_m \hat{d}^\dagger \hat{d} - \frac{\Omega_o}{2}\left(\hat{a}^\dagger \hat{d} + \hat{a}\ \hat{d}^\dagger\right) - \frac{\Omega_\mu}{2}\left(\hat{b}^\dagger \hat{d} + \hat{b}\ \hat{d}^\dagger\right) \tag{7.1}$$

is analogous to a set of cavities coupled by 50/50 beam splitters if the coupling constants are equal to $\pi/2$, as was shown schematically in Figure 1.2. The beam splitter effect in this case is produced by the coupling between the optical and mechanical resonators, $\Omega_o(t)$, or the microwave and mechanical resonators, $\Omega_\mu(t)$. The coupling is given by $\Omega_{o,\mu}(t) = -g_{o,\mu} X_{\rm ZP} A_{o,\mu}/\Delta_{o,\mu}$. Consequently, the coupling strength can be modified by changing the bare coupling strength $g_{o,\mu}$, the pump detuning, or the strength and relative phase of the pumping field.

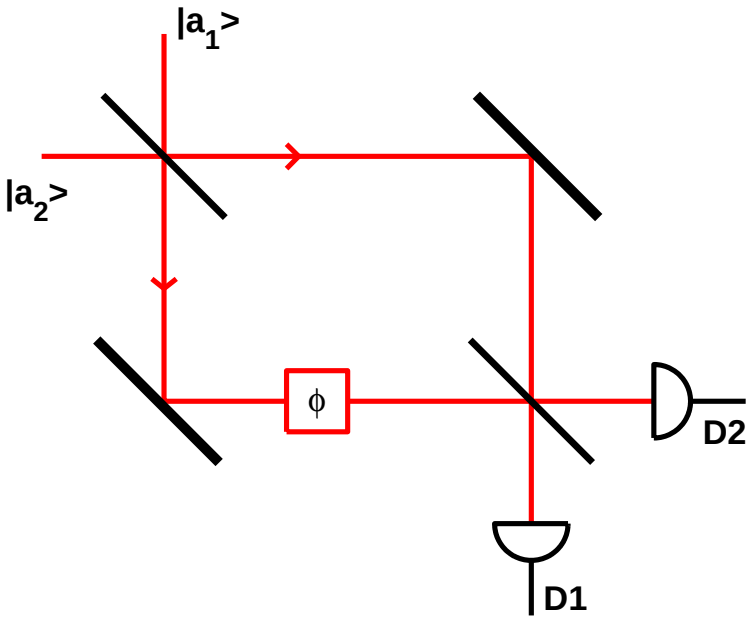

Figure 7.1: A schematic diagram of a Mach-Zehnder Interferometer.

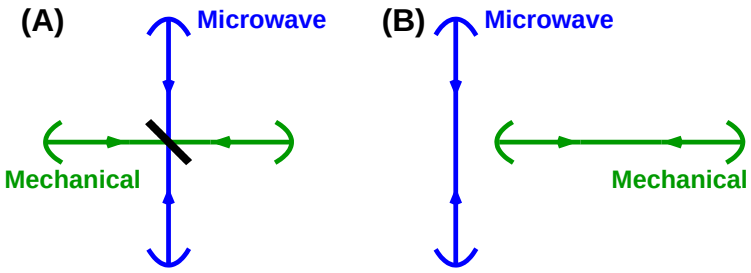

Figure 7.2: (A) Schematic of two resonators coupled with the effective beam splitter interaction of Eq. 2.27. (B) Schematic of the two resonators with the coupling turned off.

If the coupling profile is pulsed with an area of $\pi/2$, the states in the two resonators will mix equally (*i.e.*, a 50/50 beam splitter). Rather than being a physical beam splitter, mixing two quantized fields in space, the pulsed optomechanical system is an effective beam splitter mixing the two quantized fields in time. When the coupling is turned off, the states in the resonators will evolve freely, which is analogous to the free propagation segment of a typical interferometer. In this way, the effective beam splitter interaction can be turned on or off in specified sequences in order to implement the interferometer analogue. The beam splitter segment is shown schematically in Figure 7.2(A). While the free propagation segment is shown schematically in Figure 7.2(B).

In all the previous cases, the detuning of the microwave resonator from its resonance frequency, Δ_μ, is set to exactly equal the mechanical resonator frequency, ω_m, and so $\delta = 0$ in all the previous cases. For interferometry, we allow δ to deviate from 0 so that we can see the interference fringes. Since the interferometer is measuring the difference δ between the detuning and the mechanical resonance frequency, it could be used in any application that requires a precise knowledge of the mechanical resonance frequency. For example, in the actual experiment, interferometry can be used to calibrate the detuning in the microwave or optical resonator so that they are red-detuned by exactly the mechanical resonator frequency. Also, the effects of any factor that varies the mechanical frequency could be monitored, potentially in real time.

7.2 Ramsey Interferometry

We combined these elements to examine a Ramsey interferometry type measurement in the subsystem with only two coupled harmonic resonators. We choose to use the microwave and mechanical resonators here. However, the system is symmetric in the microwave and optical resonators, so using the optomechanical system would give the same results. The system of two coupled harmonic resonators can be mapped directly onto the two level atom Bloch equations in which Ramsey spectroscopy is more typically expressed. We make an analogy between the excited state of the two level atom with the state of the microwave resonator and the ground state of the two level atom with the state of the mechanical resonator. In a two level atom, the decay rate γ would correspond

to the decay out of the excited state. But, in our coupled harmonic oscillator system, we could have decay out of both the microwave and mechanical cavity. Thus, we set $\gamma = \frac{1}{2}(\gamma_m + \gamma_\mu)$ here. The Bloch equations, in the case of no dephasing, are

$$u'(t) = -\gamma u(t) - \delta v(t) \tag{7.2}$$

$$v'(t) = -\gamma v(t) + \delta u(t) - \Omega w(t) \tag{7.3}$$

$$w'(t) = -\gamma w(t) - \frac{1}{2}\gamma + \Omega v(t) \tag{7.4}$$

where, in our electromechanical system, the reduced density matrices are related to the Bloch vector components by

$$\begin{aligned} u(\Delta T) =& \frac{1}{2}\left(\langle \hat{b}^\dagger \hat{d}\rangle + \langle \hat{b}\hat{d}^\dagger\rangle\right) = \frac{1}{2}e^{-\gamma\Delta T}\sin(\delta\Delta T) \\ v(\Delta T) =& \frac{1}{2i}\left(\langle \hat{b}^\dagger \hat{d}\rangle - \langle \hat{b}\hat{d}^\dagger\rangle\right) = \frac{1}{2}\left(e^{-\gamma\Delta T} - 1\right) \\ w(\Delta T) =& \frac{1}{2}\left(\langle \hat{b}^\dagger \hat{b}\rangle - \langle \hat{d}^\dagger \hat{d}\rangle\right) = \frac{1}{2}e^{-\gamma\Delta T}\cos(\delta\Delta T) \end{aligned} \tag{7.5}$$

the decay rate is γ, the coupling constant is Ω, and $\delta = \omega_m - \Delta_\mu$.

The procedure to perform Ramsey interferometry is to start with the mechanical resonator in the ground state and the microwave resonator occupied, and thus the Bloch vector $(u(t), v(t), w(t))$ is pointing to the north pole (*i.e.*, the analogue of the atom in the excited state). The first step is to perform a $\pi/2$ pulse to entangle the state of the microwave resonator and the state of the mechanical resonator which brings the Bloch vector down to the u-v plane. The $\pi/2$ pulse swaps the states halfway so that they become maximally entangled. Then, we wait for some time during which the phase difference between the two states oscillates around the horizontal plane of the Bloch sphere. Spontaneous decay to the thermal bath is also occurring during the wait time, which shortens the length of the Bloch vector. A second $\pi/2$ pulse is performed that would bring the Bloch vector back up to the north pole where it started should the accumulated phase difference be equal to a multiple of 2π. Then, the populations and quadratures are measured. The population difference will show interference between the two states with visibility that depends on how long the Bloch vector was allowed to precess around the equator of the Bloch sphere.

Solving the Bloch equations for short, strong $\pi/2$ pulses after a wait time of ΔT gives the solutions for the final Bloch vector.

$$u(\Delta T) = \frac{1}{2} e^{-\gamma \Delta T} \sin(\delta \Delta T) \tag{7.6}$$

$$v(\Delta T) = \frac{1}{2} \left(e^{-\gamma \Delta T} - 1 \right) \tag{7.7}$$

$$w(\Delta T) = \frac{1}{2} e^{-\gamma \Delta T} \cos(\delta \Delta T) \tag{7.8}$$

Figure 7.3 shows the comparison between the numerical data and the analytic formulas for the populations. We find that the numerics matches nicely with the analytic formula.

7.3 Heisenberg Interferometry

The phase resolution for the Ramsey setup where one port is in the vacuum, the mechanical resonator in our case, is proportional to the standard quantum limit, $1/\sqrt{n}$, where n is the number of quanta in the other port, the microwave resonator in our case. However, if there are exactly equal occupation numbers entering into both ports, then the phase resolution can be decreased in principle to the Heisenberg limit [16], $1/n$, which is the fundamental limit set by quantum mechanics. The Heisenberg interferometer is a true quantum interferometer. The beam splitter entangles the two input Fock states, which makes a highly nonclassical phase state. The phase state has large number fluctuations, but small phase difference fluctuations. Thus, it improves the phase difference measurement efficiency.

In the electromechanical system, the occupation numbers of the mechanical resonator can not be directly controlled. However, if the pump is blue detuned from the mechanical resonance frequency, the pump will generate pairs of correlated photons and phonons in the microwave and mechanical resonators. It stands to reason then, that if we put a blue detuned pump segment before our red detuned Ramsey interferometer sequence, then the inputs at both ports would be correlated with equal number and the phase resolution could potentially be reduced to the Heisenberg Limit.

We transform away the self energy terms from the red and blue detuned effective Hamiltonians in Eqs 2.27 and 2.30, and set the detuning during the red detuned segments to be slightly different

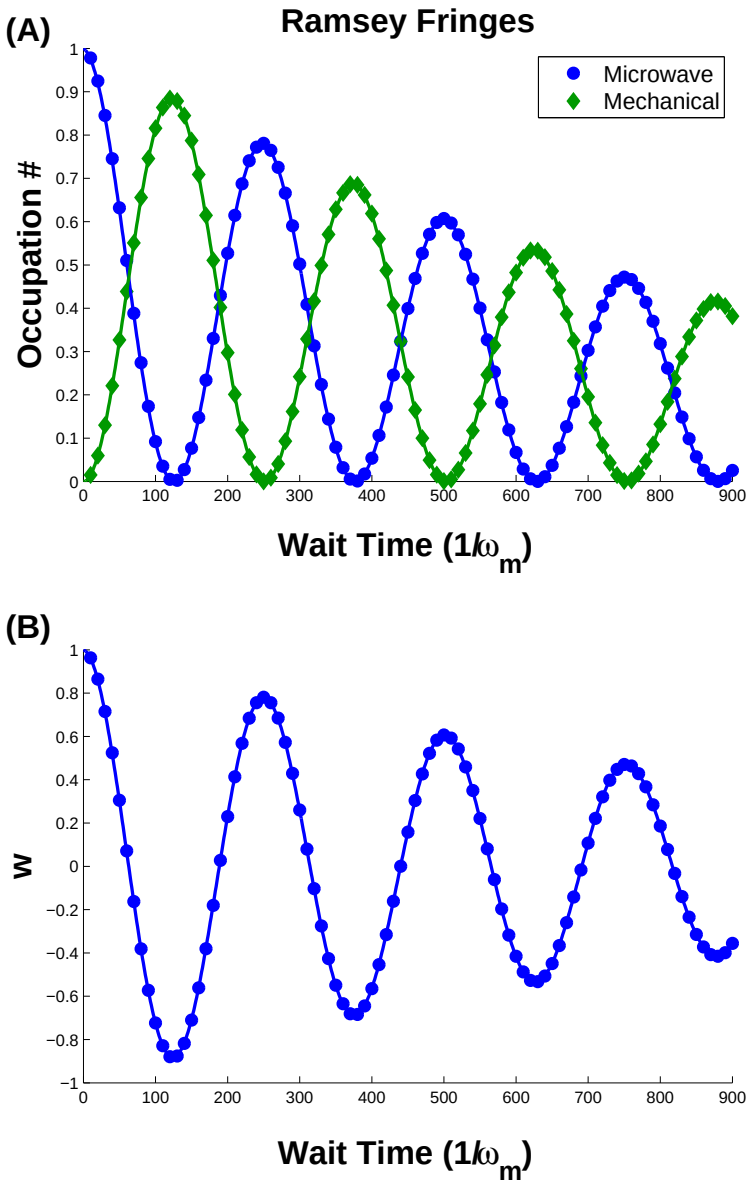

Figure 7.3: Ramsey interference fringes. (A) The populations of the microwave resonator (blue dots) and the mechanical resonator (green diamonds) swap back and forth and decay exponentially with decay rate γ. (B) The population difference analogous to $w(t)$ in the Bloch equations for the two level atom. The numerical results are given by the dots and the expected values from the Bloch equations are given by the solid lines. For these cases, $Q_m = Q_\mu = 1000$ and $\bar{n} = 0$.

from the resonance frequency of the mechanical resonator,

$$\Delta_\mu = \omega_m + \delta \ . \tag{7.9}$$

The $\pi/2$ pulses are short and strong, so that we can neglect the small δ during those segments. The δ difference from the resonance frequency only comes into play during the free propagation segment. Also, since we have restricted our consideration to the electromechanical subsystem, we set $\Omega_o = 0$. Then, the red detuned, blue detuned, and free propagation Hamiltonians respectively are

$$\frac{1}{\hbar}\hat{H_R} = \frac{\Omega_\mu}{2}\left(\hat{b}^\dagger \hat{d} + \hat{b}\hat{d}^\dagger\right) \tag{7.10}$$

$$\frac{1}{\hbar}\hat{H_B} = \frac{\Omega_\mu}{2}\left(\hat{b}^\dagger \hat{d}^\dagger + \hat{b}\hat{d}\right) \tag{7.11}$$

$$\frac{1}{\hbar}\hat{H_F} = \delta \hat{b}^\dagger \hat{b} \ . \tag{7.12}$$

7.3.1 Interferometer Theory

In order to find the occupation number in the output resonator at the end of the sequence, we need to build up the final state of the system. The initial state is the ground state in both microwave and mechanical resonators, $|\psi_0\rangle = |0,0\rangle$. Then, a blue detuned pump is applied for some time, T_B. So, the state that is input into the interferometer is

$$|\psi_1\rangle = e^{i\hat{H_B}T_B/\hbar}|0,0\rangle \ . \tag{7.13}$$

The number of photons and phonons entering the interferometer is

$$N_\mu = \langle 0,0|e^{-i\hat{H_B}T_B/\hbar}\ \hat{b}^\dagger\hat{b}\ e^{i\hat{H_B}T_B/\hbar}|0,0\rangle \tag{7.14}$$

$$N_m = \langle 0,0|e^{-i\hat{H_B}T_B/\hbar}\ \hat{d}^\dagger\hat{d}\ e^{i\hat{H_B}T_B/\hbar}|0,0\rangle \ . \tag{7.15}$$

We use the Baker-Hausdorff theorem to simplify the exponentials just as we did in Ch. 2, so that each operator is transformed in the following way,

$$e^{-i\hat{H}_B T_B/\hbar}\ \hat{b}\ e^{i\hat{H}_B T_B/\hbar} = \hat{b}\cosh\left(\frac{\Omega_\mu T_B}{2}\right) - i\hat{d}^\dagger \sinh\left(\frac{\Omega_\mu T_B}{2}\right) \tag{7.16}$$

$$e^{-i\hat{H}_B T_B/\hbar}\ \hat{b}^\dagger\ e^{i\hat{H}_B T_B/\hbar} = \hat{b}^\dagger\cosh\left(\frac{\Omega_\mu T_B}{2}\right) + i\hat{d} \sinh\left(\frac{\Omega_\mu T_B}{2}\right) \tag{7.17}$$

$$e^{-i\hat{H}_B T_B/\hbar}\ \hat{d}\ e^{i\hat{H}_B T_B/\hbar} = \hat{d}\cosh\left(\frac{\Omega_\mu T_B}{2}\right) - i\hat{b}^\dagger \sinh\left(\frac{\Omega_\mu T_B}{2}\right) \tag{7.18}$$

$$e^{-i\hat{H}_B T_B/\hbar}\ \hat{d}^\dagger\ e^{i\hat{H}_B T_B/\hbar} = \hat{d}^\dagger\cosh\left(\frac{\Omega_\mu T_B}{2}\right) + i\hat{b} \sinh\left(\frac{\Omega_\mu T_B}{2}\right)\ . \tag{7.19}$$

Plugging this expansion back into the number equations, gives,

$$\begin{aligned} N_\mu =& \langle 0,0| \Bigg(\hat{b}^\dagger\hat{b}\cosh^2\left(\frac{\Omega_\mu T_B}{2}\right) + \left(\hat{d}^\dagger\hat{d}+1\right)\sinh^2\left(\frac{\Omega_\mu T_B}{2}\right) \\ &+ i\left(\hat{b}\hat{d} - \hat{b}^\dagger\hat{d}^\dagger\right)\cosh\left(\frac{\Omega_\mu T_B}{2}\right)\sinh\left(\frac{\Omega_\mu T_B}{2}\right)\Bigg)|0,0\rangle \end{aligned} \tag{7.20}$$

$$\begin{aligned} N_m =& \langle 0,0| \Bigg(\hat{d}^\dagger\hat{d}\cosh^2\left(\frac{\Omega_\mu T_B}{2}\right) + \left(\hat{b}^\dagger\hat{b}+1\right)\sinh^2\left(\frac{\Omega_\mu T_B}{2}\right) \\ &+ i\left(\hat{b}\hat{d} - \hat{b}^\dagger\hat{d}^\dagger\right)\cosh\left(\frac{\Omega_\mu T_B}{2}\right)\sinh\left(\frac{\Omega_\mu T_B}{2}\right)\Bigg)|0,0\rangle\ . \end{aligned} \tag{7.21}$$

These equations reduce to

$$N_\mu = \sinh^2\left(\frac{\Omega_\mu T_B}{2}\right) \tag{7.22}$$

$$N_m = \sinh^2\left(\frac{\Omega_\mu T_B}{2}\right)\ . \tag{7.23}$$

The number difference $w(T_B) = \frac{1}{2}\left(N_\mu - N_m\right) = 0$ as predicted for a blue detuned pump. We expand the variance in the number difference,

$$\Delta w(t) = \frac{1}{4}\left[\langle 0,0|\left(\hat{b}^\dagger\hat{b} - \hat{d}^\dagger\hat{d}\right)^2|0,0\rangle - \langle 0,0|\hat{b}^\dagger\hat{b} - \hat{d}^\dagger\hat{d}|0,0\rangle^2\right] \tag{7.24}$$

according the Baker-Hausdorff theorem and get zero variance:

$$\langle 0,0|\hat{b}^\dagger\hat{b} - \hat{d}^\dagger\hat{d}|0,0\rangle = N_\mu - N_m = 0 \tag{7.25}$$

$$\begin{aligned} \langle 0,0|\left(\hat{b}^\dagger\hat{b} - \hat{d}^\dagger\hat{d}\right)^2|0,0\rangle =& \langle 0,0|\left(\left(\hat{b}^\dagger\hat{b} - \hat{d}^\dagger\hat{d}\right)\left(\cosh^2\left(\frac{\Omega_\mu T_B}{2}\right) - \sinh^2\left(\frac{\Omega_\mu T_B}{2}\right)\right)\right)^2|0,0\rangle \\ =& \langle 0,0|\hat{b}^\dagger\hat{b} + \hat{b}^\dagger\hat{b}^\dagger\hat{b}\hat{b} + \hat{d}^\dagger\hat{d} + \hat{d}^\dagger\hat{d}^\dagger\hat{d}\hat{d} - 2\hat{b}^\dagger\hat{b}\hat{d}^\dagger\hat{d}|0,0\rangle = 0\ . \end{aligned} \tag{7.26}$$

We have verified that the photon/phonon pairs entering the interferometer are not only equal in average number but they are also correlated, so that higher moments are also zero.

After the interferometer sequence, with a free propagation time of ΔT, the state of the system will be

$$|\psi_4\rangle = e^{i\frac{\pi}{2\Omega_\mu}\hat{H_R}/\hbar} e^{i\hat{H_F}\Delta T/\hbar} e^{-i\frac{\pi}{2\Omega_\mu}\hat{H_R}/\hbar} e^{i\hat{H_B}T_B/\hbar}|0,0\rangle \ . \tag{7.27}$$

Using the Baker-Hausdorff theorem to simplify the occupation number expectation values, we get

$$N_\mu = N_m = \sinh^2\left(\frac{\Omega_\mu T_B}{2}\right) \ . \tag{7.28}$$

This is equal to the occupation numbers entering into the interferometer because the red detuned Hamiltonian only swaps the states of the two resonators. But, the number difference is zero so the average occupation number remains constant. The variance in the number difference becomes,

$$\Delta w(t_4) = \frac{1}{4}\sinh^2\left(\Omega_\mu T_B\right)\sin^2\left(\delta\Delta T\right) \tag{7.29}$$

The amplitude of the variance oscillations scales like N_μ^2 as we would expect for a Heisenberg interferometer.

The free propagation state of the interferometer sequence doesn't change the average number in each resonator, but it does affect the phase, as we can see from the variance of the population difference. Normal interferometers would use a homodyne or heterodyne measurement to record the interference fringes caused by the phase difference in the two arms. However, in the electromechanical system, only the population in the microwave resonator can be directly measured. Thus, the variance in the w component of the Bloch vector can't be directly measured at the end of the interferometer sequence. This is like having only one detector in the interferometer, but still wanting to measure the interference fringes. For a Ramsey type interferometer, the final occupation number depends on the phase difference, so we could see the fringes with one detector. However, for the correlated equal input states in the Heisenberg interferometer, the occupation number at the end of the interferometer sequence does not depend on the phase difference, so we can't measure the phase difference with just one detector at this point in the sequence. However, there is a way

to get the information out of the interferometer. We can put another blue detuned pump segment at the end of the red detuned interferometer sequence, with the coupling set to be the negative of what it was for the first blue detuned pump segment. This will then pull pairs of photons and phonons out of the system at a rate depending on the relative phase that was built up during the free propagation segment. This will convert the phase difference into the populations of the two resonators where it can be measured.

Adding the final blue detuned pump segment to the sequence gives a final state for the system of

$$|\psi_5\rangle = e^{-i\hat{H}_B T_B/\hbar} e^{i\frac{\pi}{2\Omega_\mu}\hat{H}_R/\hbar} e^{i\hat{H}_F \Delta T/\hbar} e^{-i\frac{\pi}{2\Omega_\mu}\hat{H}_R/\hbar} e^{i\hat{H}_B T_B/\hbar} |0,0\rangle \ . \tag{7.30}$$

Again, using the Baker-Hausdorff theorem, we find the final average occupation numbers to be

$$N_\mu = N_m = \frac{1}{2}\sinh^2(\Omega_\mu T_B)\sin^2(\delta \Delta T) \ . \tag{7.31}$$

This is exactly twice the variance, so we now have a result that we can use to measure the phase difference.

The required experimental pulse sequence is summarized in Figure 7.4. The coupling strength is shown in subplot (A) and the detuning of the pump from the mechanical resonator frequency is shown in subplot (B). The first segment is the pump segment, so the pump is blue detuned with a coupling strength of $\Omega_\mu = 0.1\omega_m$ and a pump time of $T_B = 20(1/\omega_m)$. The second segment is the effective beam splitter, so the pump is red detuned with a strong coupling strength of $\Omega_\mu = -1.0\omega_m$. The strong coupling strength allows the width of the $\pi/2$ pulse to be small enough to neglect δ, the small difference from the resonance frequency of the mechanical resonator. The third segment is the free propagation, so the pump is red detuned with an offset from resonance of $\delta = 0.3\omega_m$ and propagation time $\Delta T = 21(1/\omega_m)$. The forth segment is the second effective beam splitter so the pump is red detuned with a coupling strength that is the negative of the coupling strength used for the first effective beam splitter segment. The negative sign on the coupling strength here allows for the phase accumulated during the two beam splitter segments to cancel each other out so that only the phase accumulated during the free propagation segment factors into the final measurement.

The final segment is another blue detuned pump segment with a coupling strength that is the negative of the first pump segment and the same pump time to transfer the phase difference into the final population so that it can be measured.

7.3.2 Numerical Simulations

We simulated the full interferometer sequence using the QSD approach developed in the earlier part of this thesis. Figure 7.5(A) shows the occupation numbers in each of the two resonators throughout the full interferometer sequence for zero temperature and small decay for $\Delta T = 20(1/\omega_m)$. The occupation number of each resonator is equal to each other as predicted by the above formulas. During the blue detuned pump segment the populations grow exponentially. The red detuned Hamiltonian swaps the states, but the resonators already have equal populations so the populations remain constant during the red detuned segments. The final blue detuned segment transfers the populations out of the resonators according to the accumulated phase difference so that the final number is given by Eq. 7.31. Subplot (B) shows the coupling strength following the same sequence described above. Subplot (C) shows the detuning from the mechanical resonance frequency as described above. Subplot (D) shows the variance in the number difference, $\Delta w(t)$.

The variance remains constant during the blue detuned pump segments and the free evolution segment. During first the effective beam splitter segment, the variance grows to a large value because of the huge number fluctuations of the phase state. Then, during the second effective beam splitter segment, the variance decays to the value given in Eq. 7.29.

Next, we increased the thermal temperature and the decay rates of the mechanical resonator. Figure 7.6 shows the occupation number and variance for the case of $\Delta T = 21(1/\omega_m)$, $\bar{n} = 3$, and $Q_m = 500$. Now, the mechanical resonator is thermalized to the bath temperature at the beginning of the sequence, so the number difference is non-zero. However, correlated photon/phonon pairs are still being created during the blue detuned pump segment. So both populations grow exponentially at the same rate. Since the populations are different, the beam splitter segment will swap states halfway to create a maximally entangled state as we saw for Ramsey interferometry. Then, during

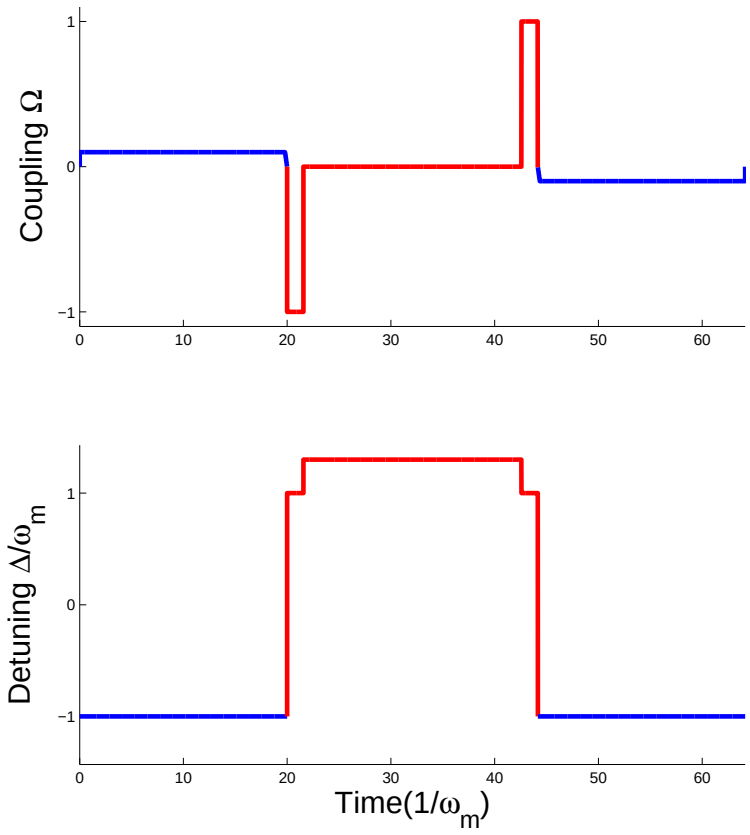

Figure 7.4: Interferometer Pulse Sequences. (A) The coupling strength throughout the interferometer pulse sequence. With blue pumping time $T_B = 20(1/\omega_m)$ and free propagation time, $\Delta T = 21(1/\omega_m)$. (B) The detuning of the microwave pump from the cavity resonance in units of the mechanical resonator frequency ω_m with $\delta = 0.3\omega_m$.

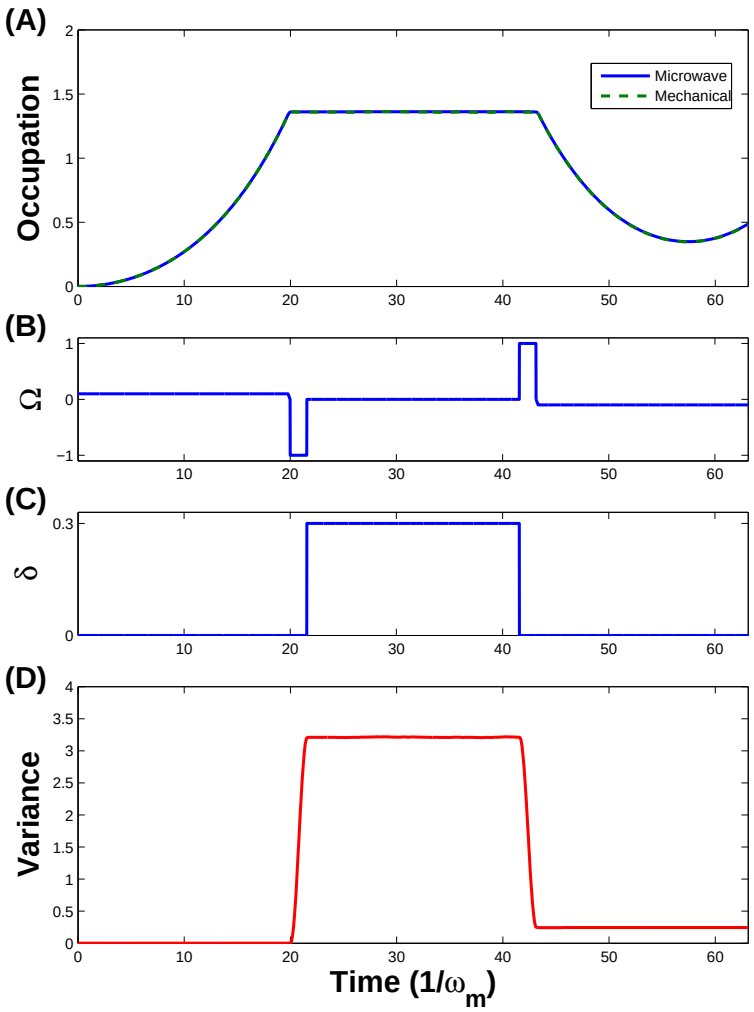

Figure 7.5: [Occupation Number and Variance throughout the Interferometer Sequence. (A) The occupation number of the microwave and mechanical resonators throughout the interferometer sequence for $\Delta T = 20(1/\omega_m)$, $\bar{n} = 0$, and $Q_m = 10000$. (B) The coupling strength throughout the sequence. (C) The detuning from the mechanical resonance frequency throughout the sequence. (D) The variance of the number difference throughout the sequence.

the free propagation segment, the average occupation number decays exponentially. The second beam splitter segment swaps the states back. Then, the final blue detuned pump segment pulls photon/phonon pairs out of the system so that the occupation numbers decay exponentially at the same rate. Subplot (D) shows the variance in the number difference. This is similar to the zero temperature case, except we see significant decay in the variance during the free propagation segment. The system inside the arms of the interferometer is in a phase state with huge number fluctuations, thus it has a large variance. And, the fluctuations decay much more rapidly than the mean.

The microwave occupation numbers from our QSD approach for various temperatures and decays is given in Figure 7.7 by the solid blue line. The mechanical occupation numbers are given by the dashed green line. For reference, twice the variance in the number difference is plotted by the red circles. For the case of zero temperature and no decay (subplot (A)), the numerical data matches with the theoretical value given in Eq. 7.31. For higher temperatures and decay rates, we don't have access to an analytic formula. We simulated the cases of $\bar{n} = 0$ and $Q_m = 500$ (subplot (B)), $\bar{n} = 3$ and $Q_m = 10000$ (subplot (C)), $\bar{n} = 3$ and $Q_m = 500$ (subplot (D)). In all these cases, the period of the oscillations is the same as for the zero temperature case, so we can still see the interference fringes regardless of temperature and decay. However, the amplitude is no longer just a factor of two as in the analytic expression. Also, as we saw above, the number difference between the mechanical and microwave resonators is non-zero for non-zero bath temperatures.

We examine the number and variance of the number difference through out the interferometer sequence for a minimum, half-max, and maximum point of the oscillation for each of the four cases in Figure 7.7. Figure 7.8 shows the four cases for the minimum point at $\Delta T = 21(1/\omega_m)$. Just as before, we see the occupation number exponentially increasing during the first blue detuned pump segment as swapping during the beam splitter segments. We also see that during the free propagation segment, the variance in the number difference decays significantly for higher decay rates and temperatures. During the final blue detuned pump segment, the number exponentially decays to almost zero. For non-zero temperatures and decay rates, the minimum here is not exactly

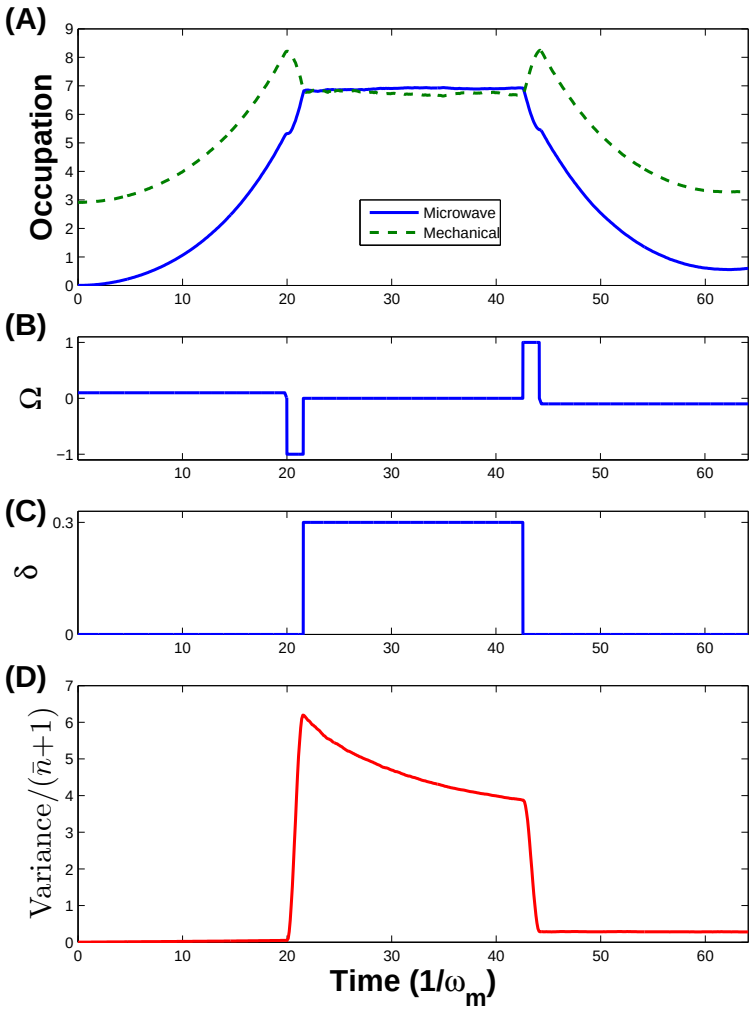

Figure 7.6: Occupation Number and Variance for non-zero Temperature. (A) The occupation number of the microwave and mechanical resonators throughout the interferometer sequence for $\Delta T = 21(1/\omega_m)$, $\bar{n} = 3$, and $Q_m = 500$. (B) The coupling strength throughout the sequence. (C) The detuning from the mechanical resonance frequency throughout the sequence. (D) The variance of the number difference throughout the sequence.

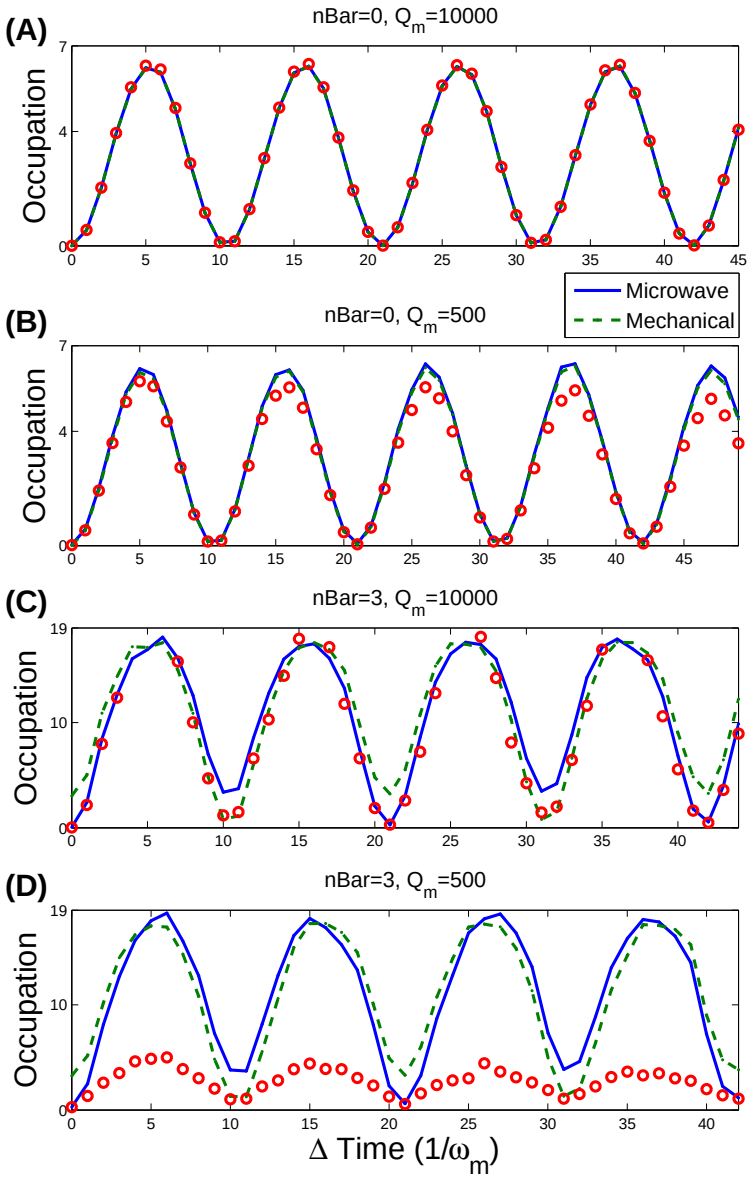

Figure 7.7: The final occupation number vs. δ for (A) $\bar{n} = 0$ and $Q_m = 10000$, (B) $\bar{n} = 0$ and $Q_m = 500$, (C) $\bar{n} = 3$ and $Q_m = 10000$, (D) $\bar{n} = 3$ and $Q_m = 500$. For reference, twice the variance in the number difference is shown by the red circles.

zero. This could be because the minimum is shifted slightly from the ideal value or because the time that is required to pull the photon/phonon pairs out of the system is modified by the temperature and decay.

Next, we look at the number and variance for a point approximately half way between the minimum and the maximum of the occupation number oscillations (Figure 7.9). Here, the final blue detuned pump sequence is decaying to its minimum value and then increasing again. The higher $\bar{n}$ values have exponential decay/growth rates that are lower than for the zero temperature curves. We also see rapid decay in the variance during the final blue detuned segment. The analytical formula for zero temperature and decay predicted that the variance would not change during the blue detuned segments. But, the non-zero decay rates and higher temperature modify this behavior.

Finally, we look at the number and variance for a point at a maximum of the occupation number oscillations (Figure 7.10). Here, during the final blue detuned segment, the number is growing exponentially to the maximum value for the number oscillations. Again, we see that the exponential growth rate is lower for the higher temperature curves than for the zero temperature curves.

7.3.3 Phase Resolution

Next, we want to examine whether the phase resolution for this interferometer sequence is decreased to the Heisenberg limit from the standard quantum limit that we would get with a vacuum in one port. If so, this would represent an ideal interferometer capable of operating at the optimal limit allowed by quantum theory.

We use Bayes theorem to calculate the phase resolution,

$$P(\delta|n)P(n) = P(n|\delta)P(\delta) \ , \tag{7.32}$$

where $P(\delta|n)$ is the probability of measuring δ given a previous measurement of n photons, $P(n|\delta)$ is the probability of measuring n photons given a previous phase difference measurement of δ. $P(n)$ is the probability of measuring n photons and $P(\delta)$ is the probability of measuring a phase

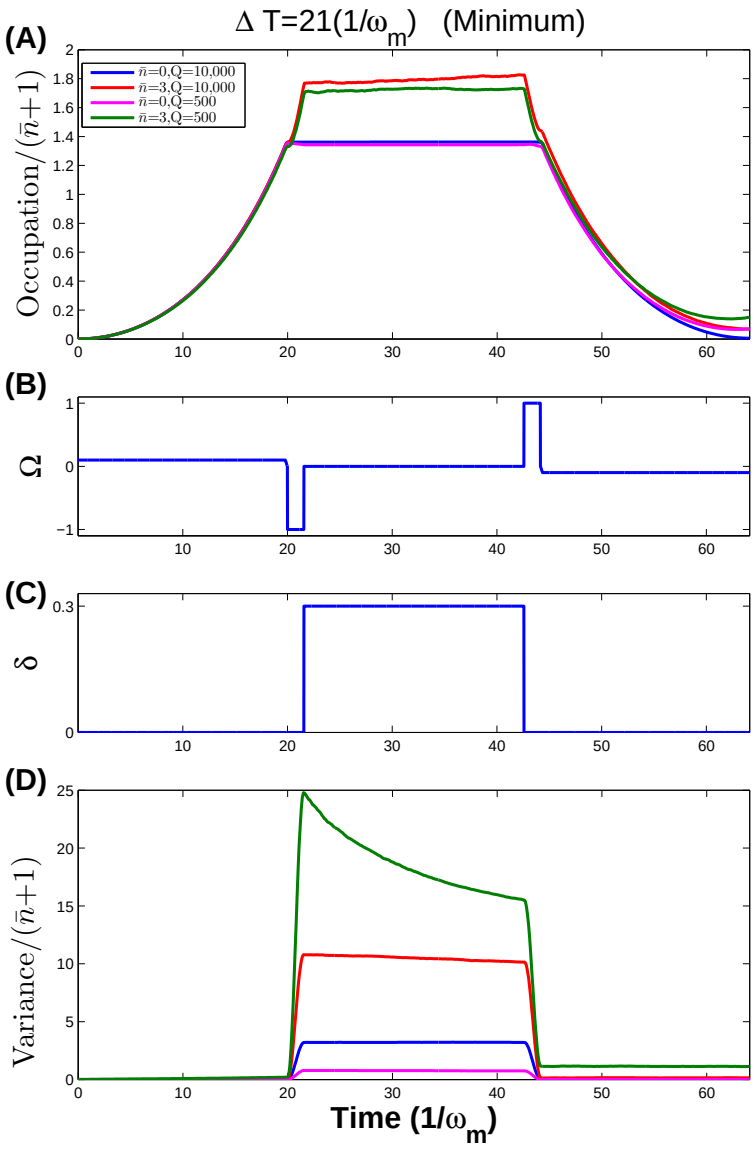

Figure 7.8: The occupation number of the microwave and mechanical resonators throughout the interferometer sequence for (A) $\Delta T = 21(1/\omega_m)$ which is at a minimum of the occupation number oscillations. (B) The coupling strength throughout the sequence. (C) The detuning from the mechanical resonance frequency throughout the sequence. (D) The variance of the number difference throughout the sequence.

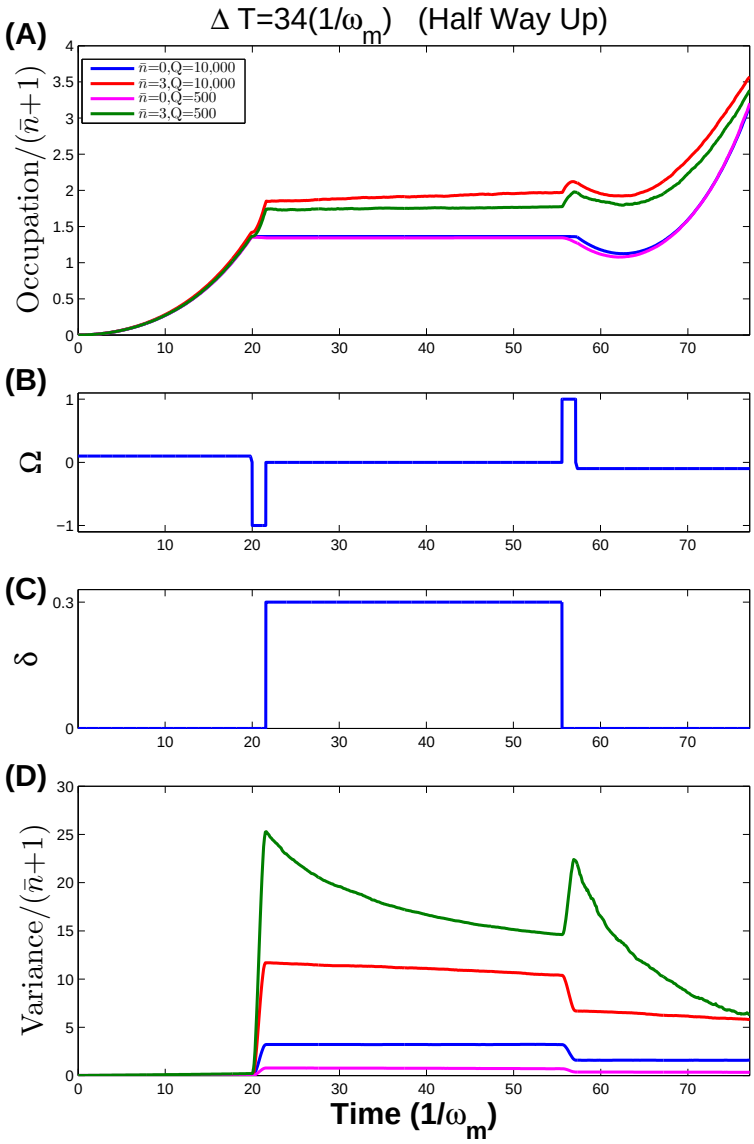

Figure 7.9: The occupation number of the microwave and mechanical resonators throughout the interferometer sequence for (A) $\Delta T = 34(1/\omega_m)$ which is approximately half of the maximum of the occupation number oscillations. (B) The coupling strength throughout the sequence. (C) The detuning from the mechanical resonance frequency throughout the sequence. (D) The variance of the number difference throughout the sequence.

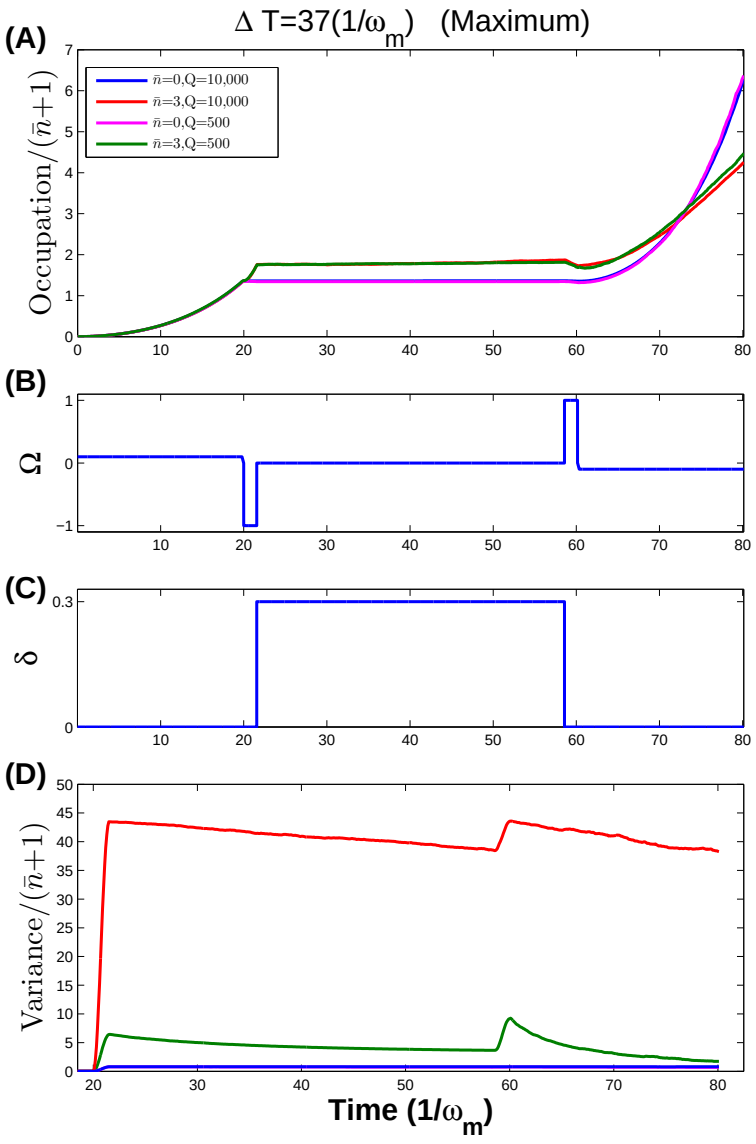

Figure 7.10: The occupation number of the microwave and mechanical resonators throughout the interferometer sequence for (A) $\Delta T = 37(1/\omega_m)$ which is at a maximum of the occupation number oscillations. (B) The coupling strength throughout the sequence. (C) The detuning from the mechanical resonance frequency throughout the sequence. (D) The variance of the number difference throughout the sequence.

difference of δ. Rearranging this equation gives the probability of measuring a certain value for δ,

$$P(\delta|n) = P(n|\delta)P(\delta)\frac{1}{P(n)} \ . \tag{7.33}$$

where $P(\delta)$ is the prior which we take to be constant and $\frac{1}{P(n)}$ is just a normalization constant found from $\int P(\delta|n)d\delta = 1$. After many measurements, we will have an improved probability of measuring a certain value for δ,

$$P(\delta|n_1, n_2, \cdots, n_N) = P(n_N|\delta)\cdots P(n_2|\delta)P(n_1|\delta)N \ . \tag{7.34}$$

The final state of the microwave subsystem with a given δ is

$$|\psi_f(\delta)\rangle = \sum_n C(n,\delta)|n\rangle \ . \tag{7.35}$$

The probabilities that go into Bayes theorem are

$$P(n|\delta) = C^*(n,\delta)C(n,\delta) \ . \tag{7.36}$$

In the QSD simulations, we have the final state of the whole system, so in order to get the probabilities for the microwave subsystem, we take the diagonal values from the reduced density matrix for the microwave subsystem. We run the simulation for a variety of δ values so that we have a table of $P(n_i|\delta_j)$ values. Then, we pick a specific $\delta_j = \delta_a$ to represent the value of the detuning used in the experiment. Lastly, we apply Bayes theorem to find the probability of measuring a detuning near the actual detuning. Figure 7.11 shows this probability for the interferometer sequence we have been discussing. We also compare this probability from the case of a coherent state input into the microwave resonator and keeping the mechanical resonator in the vacuum which should scale according to the standard quantum limit. We find that the correlated photon/phonon pairs created by the blue detuned pump do indeed give a narrower phase resolution for the phase difference δ than the case of a coherent input state in one of the resonators with a vacuum state in the other resonator.

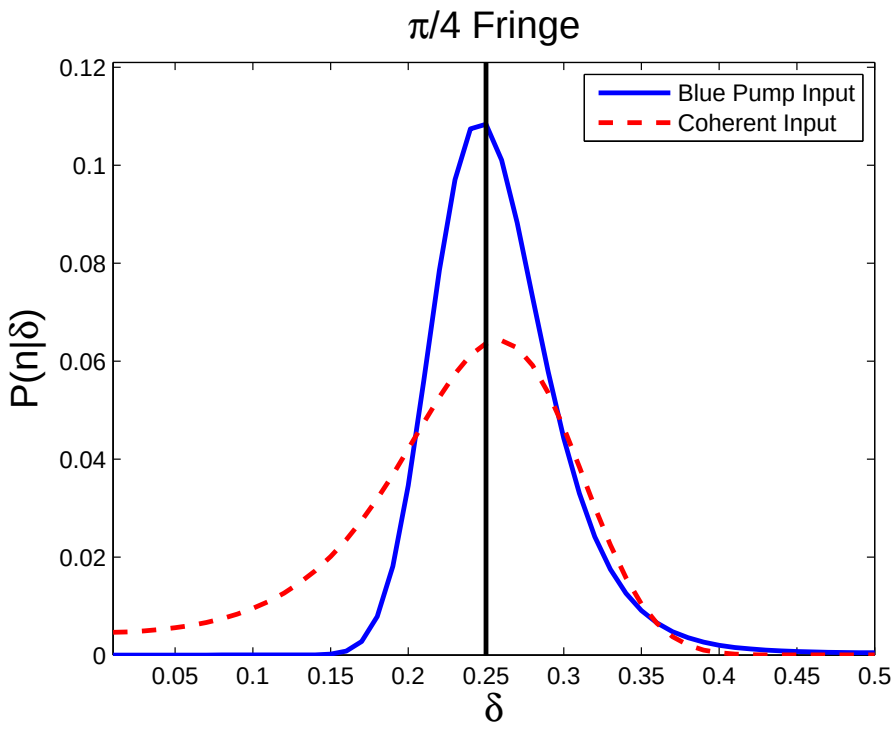

Figure 7.11: The probability of measuring a δ value near the actual δ value. The black vertical line indicates the actual δ value.

7.4 Summary

The system of two coupled harmonic resonators can be used as an interferometer for low temperatures and low decay rates. With a blue detuned pump segment before and after the interferometer sequence, the phase resolution of the interferometer can be improved. In principle, the interferometer should also work with three coupled harmonic resonators where the output from both the optical and microwave resonators could be interfered to produce fringes.

Chapter 8

Conclusion

Quantum state memory and transduction is possible for a broad range of experimentally achievable parameters in driven cavity optomechanics. Many different types of classical and quantum states can be stored in the mechanical resonator and retrieved with a high fidelity in the range of experimentally achievable mechanical quality factors. At the current experimental Q values of about $Q_m = 360,000$ [39] the quantum state can be stored in the mechanical resonator for longer than $\Delta T = 160(1/\omega_m)$ at low temperatures. As experiments cool the mechanical resonators to lower and lower $\bar{n}$ values, the time the state can be stored without significant degradation will increase. Also, as the experiments improve the coupling strength, the fidelity will increase allowing longer storage times at higher temperatures.

We have shown several procedures to accomplish transduction of quantum or classical states. High fidelity transfer is possible for Rabi type pulses of varying widths and separations even for very low Q mechanics. We have shown that over 95% transduction fidelity can be achieved for $Q_m > 4525$ for $\Omega_m = 0.1\omega_m$ and $\bar{n} = 3$ for the simultaneous pulse scheme. This scheme is quicker and more robust against thermal noise and decay than the more common separated pulse scheme. Higher bath temperatures will require a shorter simultaneous pulse with stronger coupling to achieve high fidelities.

Counter-intuitively ordered adiabatic pulses can also be used to transfer the quantum state through a STIRAP like scheme with high fidelity. This scheme is robust against thermal noise and decay and imperfections in pulse area and overlap, but requires longer transduction times. Higher

bath temperatures will also require longer transduction times to maintain the adiabaticity.

We also looked at the effects of blue detuned pump field which is analogous to a parametric amplifier, whereas the red detuned pump field is analogous to a 50/50 beam splitter. In this thesis, we only looked at the symmetric case where both the optical and microwave resonators were driven by red or blue detuned pump fields. Future analysis could explore the antisymmetric case where one of the resonators is subject to a red detuned pump field and the other is subject to a blue detuned pump field.

The reduced system of two coupled harmonic resonators is analogous to Ramsey interferometry. With a blue detuned pump segment before and after the interferometer sequence, a Heisenberg interferometer is realized and the phase resolution of the interferometer can be improved. The second blue detuned pump sequence converts the variance in the number difference (the usual observable in Heisenberg interferometry) into the occupation number of each resonator allowing the interference fringes to be measured. In principle, the interferometer should also work with three coupled harmonic resonators where the output from both the optical and microwave resonators could be interfered to produce fringes.

Bibliography

[1] U. Akram, N. Kiesel, M. Aspelmeyer, and G.J. Milburn. Single-photon opto-mechanics in the strong coupling regime. New J. Phys., 12:083030, 2010.

[2] A. Andre, D. DeMille, J. M. Doyle, M. D. Lukin, S. E. Maxwell, P. Rabl, R. J. Schoelkopf, and P. Zoller. Nature Phys., 2:636, 2006.

[3] A. Andre, D. DeMille, J. M. Doyle, M. D. Lukin, S. E. Maxwell, P. Rabl, R. J. Schoelkopf, and P. Zoller. A coherent all-electrical interface between polar molecules and mesoscopic superconducting resonators. Nat Phys, 2:636, 09 2006.

[4] V. P. Belavkin and P. Staszewski. Phys. Rev. A, 45:1347, 1992.

[5] M. Bhattacharya and P. Meystre. Trapping and cooling a mirror to its qunatum mechnical ground state. Phys. Rev. Lett., 99:073601, 2007.

[6] N. N. Bogolubov, Fam Le Kien, and A. S. Shumovsky. Physics Letters, 107A(4):173, 1985.

[7] H. J. Carmichael. Quantum trajectory theory for cascaded open systems. Phys. Rev. Lett., 70:2273, 1993.

[8] M. A. Castellanos-Beltran, K. D. Irwin, G. C. Hilton, L. R. Vale, and K. W. Lehnert. Amplification and squeezing of quantum noise with a tunable josephson metamaterial. Nature Physics, 4:929, 2008.

[9] Jasper Chan, T. P. Mayer Alegre, Amir H. Safavi-Naeini, Jeff T. Hill, Alex Krause, Simon Groblacher, Markus Aspelmeyer, and Oskar Painter. Laser cooling of a nanomechanical oscillator into its quantum ground state. Nature, 478:89, 2011.

[10] Chunhua Dong, Victor Fiore, Mark C. Kuzyk, Lin Tian, and Hailin Wang. Optical wavelength conversion via optomechanical coupling in a silica resonator. arXiv:1205.2360v1, 2012.

[11] S. Gigan, H. R. Boehm, M. Paternostro, F. Blaser, G. Langer, J. B. Hertzberg, K. Schwab, D. Baeuerle, M. Aspelmeyer, and A. Zeilinger. Self-cooling of a micro-mirror by radiation pressure. Nature, 444:67, 2006.

[12] N. Gisin and I. Percival. Phys. Lett. A, 167:315, 1992.

[13] Jeff T. Hill, Amir H. Safavi-Naeini, Jasper Chan, and Oskar Painter. Coherent optical wavelength conversion via cavity-optomechanics. arXiv:1206.0704v1, 2012.

[14] Max Hofheinz, H. Wang, M. Ansmann, Radoslaw C. Bialczak, Erik Lucero, M. Neeley, A. D. OConnell, D. Sank, J. Wenner, John M. Martinis, and A. N. Cleland. Synthesizing arbitrary quantum states in a superconducting resonator. Nature, 459:546, 2009.

[15] M. J. Holland. A Measurement Approach to the Quantum Dynamics of Open Systems. PhD thesis, University of Oxford, England, 1994.

[16] M. J. Holland and K. Burnett. Intererometric detection of optical phase shifts at the heisenberg limit. Phys. Rev. Lett., 71(9):1355–1358, 1993.

[17] Sungkun Hong, Michael S. Grinolds, Patrick Maletinsky, Ronald L. Walsworth, Mikhail D. Lukin, and Amir Yacoby. Coherent, mechanical control of a single electronic spin. arXiv:1202.1823v1, 2012.

[18] Richard Jozsa. Fidelity for mixed quantum states. Journal of Modern Optics, 41(12):2315–2323, 1994.

[19] K. Kakuyanagi, S. Kagei, S. Saito, H. Nakano, and K. Semba. Applied Physics Express, 3:103101, 2010.

[20] Dustin Kleckner, Igor Pikovski, Evan Jeffrey, Luuk Amentand Eric Eliel, Jeroen van den Brink, , and Dirk Bouwmeester. Creating and verifying a quantum superposition in a micro-optomechanical system. New J. Phys, 10:095020, 2008.

[21] P. E. Kloeden and E. Platen. Numerical solution of stochastic differential equations. Springer Verlag, Berlin, 1992.

[22] A.I. Lvovsky and J. Mlynek. Phys. Rev. Lett., 88:250401, 2002.

[23] Florian Marquardt, Joe P. Chen, A. A. Clerk, and S. M. Girvin. Quantum theory of cavity-assisted sideband cooling of mechanical motion. Phys. Rev. Lett., 99:093902, 2007.

[24] A. Nunnenkamp, K. Borkje, and S. M. Girvin. Single-photon optomechanics. Phys. Rev. Lett., 107:063602, 2011.

[25] A. D. OConnell, M. Hofheinz, M. Ansmann, Radoslaw C. Bialczak, M. Lenander, Erik Lucero, M. Neeley, D. Sank, H. Wang, M. Weides, J. Wenner, John M. Martinis, and A. N. Cleland. Quantum ground state and single-phonon control of a mechanical resonator. Nature, 464:697, 2010.

[26] R. Penrose. Quantum Concepts in Space and Time. Clarendon, Oxford, England, 1989.

[27] R. Penrose. The Emperors New Mind. Oxford University, Oxford, England, 1989.

[28] Ian Persival. Quantum state diffusion. Cambridge University Press, 1999.

[29] P. Rabl. Photon blockade effect in optomechanical systems. Phys. Rev. Lett., 107:063601, 2011.

[30] P. Rabl, D. DeMille, J. M. Doyle, M. D. Lukin, R. J. Schoelkopf, and P. Zoller. Hybrid quantum processors: Molecular ensembles as quantum memory for solid state circuits. Phys. Rev. Lett., 97:033003, Jul 2006.

[31] C. A. Regal and K. W. Lehnert. J. Phys.: Conf. Ser., 264:012025, 2011.

[32] A. H. Safavi-Naeini and O. Painter. Proposal for an optomechanical traveling wave phonon-photon translator. New Journal Of Physics, 13:013017, 2011.

[33] A. Sorensen and K. Molmer. Quantum computation with ions in thermal motion. Phys. Rev. Lett., 82:1971, 1999.

[34] K. Stannigel, P. Komar, S. J. M. Habraken, S. D. Bennett, M. D. Lukin, P. Zoller, and P. Rabl. Optomechanical quantum information processing with photons and phonons. Phys. Rev. Lett., 109:013603, Jul 2012.

[35] K. Stannigel, P. Rabl, A. S. Sørensen, P. Zoller, and M. D. Lukin. Optomechanical transducers for long-distance quantum communication. Phys. Rev. Lett., 105(22):220501, Nov 2010.

[36] S. Tanzilli, W. Tittel, M. Halder, O. Alibart, P. Baldi, N. Gisin, and H. Zbinden. A photonic quantum information interface. Nature, 437:116, 2005.

[37] J. M. Taylor, A. S. Sørensen, C. M. Marcus, and E. S. Polzik. Laser cooling and optical detection of excitations in a *lc* electrical circuit. Phys. Rev. Lett., 107:273601, Dec 2011.

[38] J. D. Teufel, T. Donner, Dale Li, J. H. Harlow, M. S. Allman, K. Cicak, A. J. Sirois, J. D. Whittaker, K. W. Lehnert, and R. W. Simmonds. Nature, 475:359, 2011.

[39] J. D. Teufel, Dale Li, M. S. Allman, K. Cicak, A. J. Sirois, J. D. Whittaker, and R. W. Simmonds. Circuit cavity electromechanics in the strong-coupling regime. Nature, 471:204, 2011.

[40] L. Tian and H. Wang. Phys. Rev. A, 82:053806, 2010.

[41] A. Uhlmann. Rep. Math. Phys., 9:273, 1976.

[42] E. Verhagen, S. Deleglise, S. Weis, A. Schliesser, and T. J. Kippenberg. Quantum-coherent coupling of a mechanical oscillator to an optical cavity mode. Nature, 482:63, 2012.

[43] A. Wallraff, D. I. Schuster, A. Blais, L. Frunzio, R. S. Huang, J. Majer, S. Kumar, S. M. Girvin, and R. J. Schoelkopf. Circuit quantum electrodynamics: Coherent coupling of a single photon to a cooper pair box. Nature, 431:162, 2004.

[44] D.F. Walls and G.J. Milburn. Quantum Optics. Springer-Verlag, 1994.

[45] Ying-Dan Wang and Aashish A. Clerk. Using dark modes for high-fidelity optomechanical quantum state transfer. arXiv:1205.5284v1, 2012.

[46] Ying-Dan Wang and Aashish A. Clerk. Using interference for high fidelity quantum state transfer in optomechanics. Phys. Rev. Lett., 108:153603, Apr 2012.

[47] H. M. Wiseman and G. J. Milburn. Phys. Rev. A, 47:642, 1993.

[48] H. M. Wiseman and G. J. Milburn. Interpretation of quantum jump and diffusion processes illustrated on the bloch sphere. Phys. Rev. A, 47:1652, 1993.

[49] Jing Zhang, Kunchi Peng, and Samuel L. Braunstein. Quantum-state transfer from light to macroscopic oscillators. Phys. Rev. A, 68:013808, Jul 2003.